THESIS

submitted to

THE FACULTY OF SCIENCE OF ROUEN UNIVERSITY

for the degree of Doctor of Philosophy

Discipline: Physics

Speciality: Energy

by

Minglin YANG

Computation of light scattering, radiation force, torque and stress of large non-spherical particles with Multilevel Fast Multipole Algorithm and Vectorial Complex Ray Model*

Defense on December 9, 2014

Supervisor

Professor Kuan Fang REN

Composition of Jury:

Reviewers:

Fabrice ONOFRI	Director of research at CNRS, UMR 7343 - IUSTI, Marseille
Ping YANG	Professor at Texas A&M University, Texas, USA

Examiners:

Bernard POULIGNY	Director of research at CNRS, CRPP, Bordeaux, France
Kuan Fang REN	Professor at Rouen University, CORIA-UMR 6614, Rouen
Claude ROZÉ	Professor at Rouen University CORIA-UMR 6614, Rouen
Xin Qing SHENG	Professor at Beijing institute of technology, Beijing, China

* The title of the thesis has been modified according to the suggestion of the defense committee. The original title was

Light Scattering by Large Non-spherical Particles
with Multilevel Fast Multipole Algorithm and Vectorial Complex Ray Model

THESE

présentée

A LA FACULTE DES SCIENCES DE L'UNIVERSITE DE ROUEN

en vue de l'obtention du Doctorat

Discipline : Physique

Spécialité: Energétique

par

Minglin YANG

Calculs de diagramme de diffusion, force, couple et tension de radiation pour des grosses particules Non Sphèriques par MLFMA et VCRM*

Soutenue le 9 Dècembre 2014

Directeur de thèse

Professeur Kuan Fang REN

Membres du jury:

Rapporteurs:	
Fabrice ONOFRI	Directeur de recherche au CNRS, UMR 7343 - IUSTI, Marseille
Ping YANG	Professeur à la Texas A&M University, Texas, USA
Examinateurs:	
Bernard POULIGNY	Directeur de recherche au CNRS, CRPP, Bordeaux
Kuan Fang REN	Professeur à l'Université de Rouen CORIA-UMR 6614, Rouen
Claude ROZÉ	Professeur à l'Université de Rouen , CORIA-UMR 6614, Rouen
Xin Qing SHENG	Professeur à la Pékin Institut de Technologie, Pékin, Chine

* Le titre de cette thèse a été modifié selon la suggestion du jury. The titre original était:

Diffusion de la Lumière par des Grosses Particules Non Sphèriques par MLFMA et VCRM

Acknowledgements

Foremost, I would like to express my heartfelt gratitude to my advisor Professor Kuan Fang REN for his continuous support through my Ph.D study, for his patience, encouragement, enthusiasm, and immense knowledge. His guidance helped me in all the time of research and writing of this thesis. Ever since, Professor REN has supported me not only by providing a research assistantship, but also academically and emotionally through the rough road to finish my thesis. Besides, during my stay in French, Professor REN has helped me a lot in my daily life.

Next, I would like to express my very sincere gratitude to Professor Xin Qing SHENG, my co-adviser in Beijing Institute of Technology, China. It is his encouragement and supports, which gave me confidence to study as a joint Ph.D abroad. In fact, Professor SHENG has guided me for more than seven years since I get my Bachelor's degree and became a Ph.D candidate in 2007. His creative idea and excellent insight into the computational electromagnetic brings me an open mind to do research work and his attitude of work triggers my love for science.

I want to thank CORIA[1]/UMR 6614[2], CNRS[3] - Université & INSA[4] de Rouen for providing me a comfortable working environment and all the supports during my stay here. I thank Drs. Keli JIANG, Hongjie WANG, Fan WANG, Yi WU, Xingling TANG, Liu Chu, Mincheng TANG and Zelong MA for the happy time we spent together during my stay in France, also for their care and love.

I am also thankful to my colleagues in Center for Electromagnetic Simulation (CEMS) in Beijing Institute of technology, Beijing, China. Drs. Hongwei GAO, Mingjiang GOU, Biyi WU, Xumin SUN and all the other colleagues for the help and support during my stay in French.

My grateful and special thanks are of course due to the members of the jury, Dr. Fabrice ONOFRI, Professor Ping YANG, Professor Bernard POULIGNY and

[1]CORIA: COmplexe de Recherche Interprofessionnel en Aérothermochimie
[2]UMR: Unité Mixte de Recherche
[3]CNRS: Centre national de la recherche scientifique
[4]INSA: Institut National des Sciences Appliquées

Professor Claude ROZÉ for examining this manuscript and evaluate this work. I would like to give thank of them for their patience in reading the manuscript as well as for their precious comments.

Finally, I take this opportunity to express the profound gratitude from my deep heart to my parents, my sisters, my fiancee Dr. Yueqian WU and my friends for their love and spiritual and material support.

My stay in France during the two first years of the thesis was supported by the China Scholarship Council. This work was also partially supported by substantial computation facilities from CRIHAN (Centre de Ressources Informatiques de Haute-Normandie) and the French National Research Agency under the grant ANR-13-BS09-0008-01 “AMO-COPS”.

Contents

List of Symbols and Abbreviations

Abbreviations

ABC	:	Absorbing Boundary Condition
ASP	:	Approximate Schur Preconditioner
CTF	:	Combined Tangential Formulation
CNF	:	Combined Normal Formulation
DDA	:	Discrete Dipole Approximation
DDM	:	Domain Decomposition Method
EBCM	:	Extended Boundary Condition Method
FDTD	:	Finite Difference Time Domain Method
FEM	:	Finite Element Method
GLMT	:	Generalized Lorenz-Mie Theory
GMRES	:	Generalized Minimal Residual Method
GO	:	Geometrical Optics
GTD	:	Geometrical Theory of Diffraction
LG	:	Laguerre-Gaussian
LMT	:	Lorenz-Mie Theory
LTASP	:	Lower Triangular Approximate Schur Preconditioner
MLFMA	:	Multilevel Fast Multipole Algorithm
MoM	:	Method of Moments
MPI	:	Message Passing Interface
N-EFIE	:	Normal Electric-Field Integral Equation (T-EFIE)
N-MFIE	:	Normal Magnetic-Field Integral Equation (T-EFIE)
OpenMP	:	Open Multi-Processing
PDE	:	Partial Differential Equation
PEC	:	Perfect Electric Conductor
PMCHW	:	Poggio-Miller-Chang-Harrington-Wu-Tsai

PML	:	Perfectly Matched Layer
PO	:	Physical Optics
PTD	:	Physical Theory of Diffraction
RPF	:	Radiation Pressure Force
RWG	:	Rao, Wilton and Glisson
SAI	:	Sparse Approximate Inverse
SIE	:	Surface Integral Equation
SVM	:	Separation of Variable Method
T-EFIE	:	Tangential Electric-Field Integral Equation (T-EFIE)
T-MFIE	:	Tangential Magnetic-Field Integral Equation (T-EFIE)
VCRM	:	Vectorial Complex Ray Model
VSWF	:	Vector Spherical Wave Functions

Roman Symbols

a	:	radius of particle
A	:	rotation matrix
$\boldsymbol{b}$	:	base vector perpendicular to the incident plane
C	:	curvature matrix of dioptric surface
$\mathcal{D}$	:	the divergence factor in VCRM
D	:	divergent factor in GO
$\boldsymbol{E}^i$	:	incident electric field
$\boldsymbol{E}^a$	:	internal electric field
$\boldsymbol{E}^e$	:	external electric field
$\boldsymbol{E}^s$	:	scattering electric field
E_0	:	amplitude of incident electric field
$\mathbf{J}$	:	equivalent electric currents
$\boldsymbol{H}^i$	:	incident magnetic field
$\boldsymbol{H}^a$	:	internal magnetic field
$\boldsymbol{H}^e$	:	external magnetic field
$\boldsymbol{H}^s$	:	scattered magnetic field
$h_n^{(2)}$	:	hankel function of the second kind
I	:	scattered intensity
$\overleftrightarrow{I}$	:	the 3×3 unit dyad
$\mathbf{g}$	:	vector basis function
G	:	Green's function
k	:	wave number
k_n	:	component of wave vector in normal direction
k_τ	:	component of wave vector in tangent direction
$\boldsymbol{k}$	:	incident wave vector
$\boldsymbol{k}'$	:	refracted wave vector
$\boldsymbol{k}^l$	:	reflection wave vector
L	:	number of multipole expansion terms

m	:	refractive index
m_i	:	imaginary part of the refractive index
$\mathbf{M}$	:	equivalent magnetic currents
p	:	order of ray
P_n	:	Legendre polynomial of degree n
Q	:	curvature matrix of incident wave
Q'	:	curvature matrix of refracted/refleccted wave
R_1	:	one of the curvature radii of a wavefront
R_2	:	one of the curvature radii of a wavefront
R'_{11}	:	one of the curvature radii of the refracted/reflected wavefront
R'_{12}	:	one curvature radius of refracted/reflected wavefront
R_u	:	the curvature of wave front in u direction
R_v	:	the curvature of wave front in v direction
S	:	scattered amplitude
S_G	:	complex amplitude of incident beam
S_d	:	complex amplitude of diffracted wave
$\boldsymbol{s}_1$	:	one of the principal directions of the dioptric surface
$\boldsymbol{s}_2$	:	one of the principal directions of the dioptric surface
$\boldsymbol{t}_1$	:	one of the principal directions of the wavefront
$\boldsymbol{t}_2$	:	one of the principal directions of the wavefront
$\hat{\mathbf{t}}$	:	surface unit tangential vector
$\overleftrightarrow{T}$	:	Maxwell's stress tensor
w_0	:	waist radius of a circular Gaussian beam
Z_l	:	wave impendence in material l

Greek Symbols

α	:	one of the three Euler angles
β	:	one of the three Euler angles
γ	:	one of the three Euler angles
ε	:	electrical permittivity
θ_i	:	incident angle
θ_r	:	refracted angle
θ'	:	deviation angle
θ	:	scattering angle
θ_{rg}	:	geometrical optics rainbow angle
Θ	:	projection matrix
κ_G	:	Gaussian curvature
κ_M	:	mean curvature
λ	:	wavelength
μ	:	permeability
ξ_a	:	absorbing factor or angle between the incident wave and x axis
x	:	size parameter
ρ_1	:	one of curvature radius of a dioptric surface
ρ_2	:	one of curvature radius of a dioptric surface
τ	:	angle between incident ray and dioptric surface
τ'	:	angle between refracted ray and dioptric surface
$\boldsymbol{\tau}$	:	unit vector tangent to the cylinder surface
ϕ_F	:	phase shift due to Fresnel coefficient
ϕ_T	:	phase shift due to total reflection
ϕ_{PH}	:	phase shift due to optical path
ϕ_{FL}	:	phase shift due to focal lines
ϕ_p	:	total phase shift
φ	:	phase function of the incident wave

Subscripts or superscripts

X	:	1 for perpendicular polarization state and 2 for parallel polarization state

Chapter 1

Introduction

Light, microwaves, x-rays, and TV or radio transmission waves are all kinds of electromagnetic (EM) waves with different wavelengths. When they encounter objects, they are scattered and absorbed, their propagations are deviated or attenuated. At the same time, the scattered waves contain some information on the object, permitting to measure or detect the properties of the object, such as the detection of objects with radar, imaging of complex spray, measurement of raindrops, and many optical techniques in the metrology of fluid mechanics and combustion, and in the environment detection. Furthermore, when an object is illuminated by an electromagnetic wave, it experiences a force and/or a torque, that maybe useful permits to manipulate the object without direct contact leading to the development of optical tweezers which play an important role in the life science. Therefore, the electromagnetic wave or light scattering is of great interest in many fields and a large number of theories and models have been developed, but new models are still necessary.

Research methods on electromagnetic wave interaction with particle can be divided into two catalogs: experimental research and theoretical research. The prime method of enquiry in science is the experiment. It may provide information of the "real world" and check the theoretical research, but it is often limited by real conditions, experimental costs, time-consuming costs and error-prone. The theoretical research permits, on the other hand, revealing better understanding of the phenomena, finding the law of nature and guiding the experimental research in the practical applications. With the development of computer technology, the computational ability has been improved dramatically in the last few decades and plays an increasing role in many applications such as engineering and designing. As a result, numerical methods are more and more omnipresent in the theoretical research. With the help of numerical

analysis, optimization of optical devices and improvements on optical technology and theory can be done.

When electromagnetic waves interact with objects, the behaviors may be very different according to the wavelength. The researches on the scattering of EM waves by objects are classified according to the wavelength. In the microwave domain (frequencies between 300 MHz and 300 GHz), after decades of efforts, a great progress has been recently achieved in solving the problems concerning complex objects (such as aircraft, antenna arrays, ...). The calculable size of scatters of perfect conductor can be of several hundreds of wavelengths. In the optical domain, the attention is more concentrated to the particles of simple shape. Because the wavelength of light is much shorter than the microwaves, the particles of some tens of micrometers are already too large to be treated with numerical methods, while the rigorous methods can only be applied to very simple shaped particles. The scientific and industrial communities do not have any mean to predict accurately the scattering and absorption properties of large complex shaped particles, whose size may reach up to a few tens of microns and whose shape deviate from the canonical spherical and cylindrical shapes. For example, in fluid mechanics, the characterization of a fuel injector of an automobile engine, the study of the instability and the breakup of the liquid jets are essential problems on the other way. A free jet is not circular cylindrical even in the most stable case. Single cells, subcellular components and biological molecules trapped in optical tweezers have irregular shapes too. The research on the interaction of light and complex non-spherical particles is thus a challenge in the development of optical metrology. Lack of means to deal with the scattering of large complex shaped particles severely limit possibility to understand, characterize and control many particle systems of interest. In this PhD thesis, we intend to make a step forward towards the computation of light scattering by large non-spherical particles.

The laboratory CORIA has developed in the recent year a novel ray model to predict the scattering of large irregular shape particle. It is very premising but needs to be validated by other methods. The Center for electromagnetic simulation (CEMS) in Beijing Institute of Technology has a rich experience in the electromagnetic computations. The multilevel fast multipole algorithm (MLFMA) they have developed is one of the most powerful algorithms in the field. The aim of this PhD thesis is therefore to join the competence of the two laboratories, on both approaches. The work of this thesis consists of the implementation of these algorithms for large non-spherical particles, the comparison of the results, and the application of the developed tools to the

prediction of force, torque and the stress exerted by a laser beam on such particles.

Theories and models of light scattering

Light is essentially a high frequency electromagnetic wave. Theoretically, all kinds of phenomena concerning the linear interaction between light and the electromagnetic waves can be solved by famous Maxwell's equations together with the associated boundary conditions. In practice, various theories and models have been developed according to the properties of the waves and the scatters. They can be categorized into three groups: rigorous theories, approximate methods and numerical methods.

Rigorous theories are based on the solution of Maxwell's equations usually by variable separation. The Lorenz-Mie theory (LMT) is one of the most famous theories. Originally, it was developed to describe the interaction between a homogeneous isotropic sphere and an electromagnetic plane wave [1, 2]. Then it has been extended to the scattering of a plane wave by other simple shaped particles (infinite long cylinder, spheroid, ellipsoid ...). However, these theories are limited to the plane wave incident problem. In the 1980s', the Lorenz-Mie theory was generalized to take into account the shape of the incident wave [3, 4, 5]. To do so, one of the most famous formalisms is the named Generalized Lorenz-Mie theory (GLMT), originally developed for the scattering of a Gaussian beam by a homogeneous spherical particle [5, 6, 7, 8, 9]. In GLMT, two sets of beam shape coefficients are employed to describe the incident beam. Various methods can be employed to evaluate beam shaped coefficients including quadratures, finite series, localized approximations, and the s-expansion method. Later, GLMT was extended to other simple shape particles: multilayered spheres [10], ellipsoids [11, 12], infinitely long cylinders with circular [13, 14] or elliptical cross-sections [15], sphere with one arbitrarily located spherical inclusion [16], and aggregates [17]. But the calculable size of particles is often limited to some tens of wavelengths except the sphere.

Approximate methods are not rigorous but flexible. Rayleigh theory applies to particle sizes much smaller than the wavelength and the Rayleigh-Gans theory for optically "soft" (i.e. with a refractive index close to 1) particles [18]. High frequency approximate methods, such as the geometrical optics (GO), the physical optics (PO), the geometrical theory of diffraction (GTD) and the physical theory of diffraction (PTD) can be used to deal with the scattering of very large (compared to the incident

wavelength) and complex shape particles. Besides their powerful computational capabilities for electrically large particles, another advantage of the latter methods is that they can give physical explanation and help us to understand clearly the mechanism of scattering. In the case of spherical particles or infinite circular cylinders, the GO is proved to be able to predict very accurately the scattering diagram in almost all directions. GO has been widely used for predicating light scattering by large particles. The research group of Yang has combined the GO with the electromagnetic wave method to predict the total scattering properties such as the scattering matrix [19, 20, 21]. But, GO is rarely applied to the scattering diagrams of a three dimensional (3D) irregular shaped particle because of the difficulties in the determination of reflection and refraction angles, in the calculation of local divergence/convergence and the phase shift due to focal lines [22].

Alternatively, the scattering problem of any shaped particle can be dealt with numerically by direct solution of Maxwell's equations and these methods are termed as numerical methods. These methods solve Maxwell's equations numerically, without any simplification. The T-matrix method (also called null field method or extended boundary condition method (EBCM)) can yield highly accurate numerical solution for the scattering of light by non-spherical particles, via regular vector spherical wave functions (VSWF) and a transformation matrix (so called T-matrix). Under the EBCM, the T-matrix for general particles is given by a set of integrals of vector cross products of vector spherical harmonics taken over the surface of the scatterer. It is viewed as a semi-analytical method. This is because, on one hand, it can be treated as an extension of the Lorenz-Mie theory, because it is also based on expansion of the incident, transmitted and the scattered fields into a series of VSWF. On the other hand, it can also, in some way, be considered as a surface discrete numerical method because it calculates numerically integrals over the surface enclosing the volume involving only the tangential components of the fields on the surface. The T-matrix method was developed by Waterman in a series of papers [23, 24]. It is popular in solving light scattering by non-spherical axially symmetric particles. A T-matrix code for computing scattering by non-spherical and aggregated particles is presented by Mishchenko *et al.* [25, 26]. The T-matrix technique usually relies on central expansions of the electromagnetic field in VSWF. When the particle is spherical, this integral can be evaluated analytically resulting in a diagonal matrix, whose elements are given by the Mie coefficients. For non-spherically symmetric particles, the integration must be numerically evaluated by quadrature [27]. To circumvent the the ill-condition problem in inverting the so-called Q-matrix, EBCM is combined with invariant imbedding

method makeing it applicable to a large class of scattering problems [28, 29].

Besides the T-matrix method, other numerical methods are generally divided into two groups by the form of Maxwell's equations they solve: differential-equation and integral-equation techniques. Differential equation methods compute the scattered field by solving the vector wave equation in the frequency or in the time domain, whereas integral equation methods are based on the integral counterparts of Maxwell's equations.

The finite-difference time-domain (FDTD) technique was introduced by Yee in 1966 [30]. It is a useful numerical method for modeling computational electromagnetics by finding approximate solutions to the associated system of differential form of Maxwell's equations. Since it is a time-domain method, FDTD solutions can cover a wide frequency range and treat nonlinear material properties in a natural way. In FDTD, the two curl equations in Maxwell's equations are converted into a set of finite difference equations by discretizing time into finite steps and solution region into rectangular grids. The FDTD method is a widely used and simple numerical method for computational electromagnetic [31, 32, 33]. It has several advantages and disadvantages. It is a versatile modeling technique that can manage any shaped particles. It also allows the user to specify the material proprieties at all points within the computational domain. Furthermore, in FDTD, there is no need to solve a large system of linear equations, and the memory storage requirement is proportional to the total number of grid points. On the other hand, since the FDTD is a volume discritized method, the number of unknowns increases quickly with increment of particle size parameter. The regular cubic mehs used by Yee is not flexible for models with long, thin or shape features because of the excessively large computational domain. Since FDTD can only be applied for finite computational domain, the total solution domain should be truncated with a virtual surface enclosing the particles with absorbing boundary conditions (ABCs) or a perfectly matched layer (PML) to minimize the effects of reflection. Usually, to promise the absorbing effect, the PML or ABC will be placed at a distance from the particle [34, 35]. That makes the total solution region larger than size of the particle. The finite spatial discretization and approximate boundary conditions will affect the accuracy of the FDTD and makes it poorly suitable for achieving high and controllable numerical accuracy.

The finite element method (FEM) is also a powerful full wave numerical method. It uses variational methods to minimize an error function to produce a stable solution. It is a volume discretized method, hence it can be used to deal with inhomogeneous,

anisotropic particles but it requires large computer resources for large particles. Similar to the FDTD, it use ABC or PML to truncate the solution region hence its accuracy highly depends on the boundary truncate accuracy. Its advantage is that it can use tetrahedral elements to model the solution domain, hence it can achieve good geometry modeling accuracy for particles with corners or edges. The FEM will form a sparse matrix equation system, which is usually hard to solve iteratively because of its bad conditioning number. This sparse matrix can be solved with fast sparse solver such as multifrontal approach more efficiently [36]. Moreover, the domain decomposition method can greatly enhance its capability especially for periodical structures such as antenna arrays [37, 38]. FEM has been widely used to solve thermal, electromagnetic, fluid, and structural problems.

Both FEM and FDTD are differential equation methods and an additional implementation of approximate boundary conditions is necessary because of the finite spatial discretization. On the contrary, the integral equation (IE) methods automatically satisfy the radiation boundary condition. They are efficient and provide good flexibility and accuracy for open region problems such as radiation and scattering. In the integral equation methods, the original boundary value problems for Maxwell's equations are reformulated as integral equations over the boundary interfaces or over the entire volume, hence they can be termed as volume integral equations (VIEs) or surface integral equations (SIEs). The integral equations can be converted from field theory to mathematical equations by using techniques such as the method of moments (MoM) [39] or other modifications of MoM such as the discrete dipole approximation (DDA) [40].

In optical domain, the DDA is more widely used than the MoM implementation of VIEs for scattering problems. In DDA, the particle is modeled as a lattice of dipolar point scatterers (dipoles). The scattered fields of the dipole interact with each other, and with the external field. The approximation of these interactions is based on the integral equation for the electric field. So the DDA is also referred to as the coupled dipole approximation. Initially the DDA was proposed by Purcell and Pennypacker replacing the scatterer by a set of point dipoles [40]. Later, developments and improvements on DDA have been done [41, 42, 43, 44]. Now, a C implementation of the DDA named ADDA [44] and a Fortran code developed by B. T. Draine *et al.* called DDScat [42] are available on website. Although the final equations are essentially the same, derivations based on the integral equations give more mathematical insight into the approximation, while the model of point dipoles is physically clearer. Since in

DDA, the whole volume of the particles is discretized into small cubical subvolumes, the optical properties (refractive index) of each dipole can be set independently, it has the ability to naturally simulate the scattering of any arbitrarily shaped and/or inhomogeneous scatterer. DDA can also be accelerated by using the fast fourier transform (FFT) for matrix-vector multiplication [45]. However, in DDA, the computation resources increase quickly and size of the particles is severely limited, especially for high refractive index particles [44]. Cubical subvolume meshes also make it not flexible and efficient for those complex shaped particles with sharp corners or wedges.

MoM implementation of surface integral equations (SIEs) is widely used for computing electromagnetic scattering by homogenous objects, such as design of dielectric components on satellite, cockpit cover of aircraft, and optical crystal devices [46, 47, 48]. By using the equivalence principle, four different integral equations, namely the tangential electric-field integral equation (T-EFIE), the normal electric-field integral equation (N-EFIE), the tangential magnetic-field integral equation (T-MFIE), and the normal magnetic-field integral equation (N-MFIE) can be derived for both inner and outer region by considering the boundary conditions for the electric and magnetic fields separately [49]. In the past few years, various formulations have been derived by using different combinations of the boundary conditions, testing schemes, and scaling operations [49, 46, 50, 51, 47]. These formulations are generally constructed from tangential (T) or normal (N) equations or a combination form of them. SIE formulations will result in a large-scale matrix equation system which can be solved with iterative solvers such as the generalized minimal residual method (GMRES). Because of the full MoM matrices, the size of the object is servery limited. Matrix-vector multiplications are performed with various acceleration methods [52, 53, 54]. Among these acceleration methods, the MLFMA has been well developed and can be used to solve challenging problems [55, 56, 57]. By employing MLFMA to speed up matrix-vector multiplication in the iterative solution of the final matrix equation system, both the time and the memory complexity can be reduced.

In the view of meshes used to model geometry of the particle, DDA, FEM and FDTD are volume discretized methods. Their number of unknowns is related to the volume of the particle($O(x^3)$ with $x = 2\pi a/\lambda$). Mesh density (size of dipolars for DDA, Yee cells for FDTD and average edge length of tetrahedral elements for FEM) in these volume discretized methods is usually about $1/(10|m|)$ to $1/(20|m|)$ with m being the refractive index of the scatterer. They are flexible and robust for inhomogeneous, anisotropic particles but the computation resource need increases rapidly with the

particle size, limiting this approach to the scattering of small particles. In the MoM implementation of SIEs, triangles patches are used, which limits the discretization of the unknowns to the surface of the particle and it can be termed as a surface discrete method. Compared with the volume discrete methods, such as the DDA, the FEM or the FDTD, SIE method is more flexible and efficient for large homogenous particles, especially for particles with large refractive index. Furthermore, discrete with triangles makes it easier to generate meshes for modeling irregular shape particles. Compared with T-matrix method, the SIE is also more general because it dose not need any expansion of the field into a series of VSWF. The SIE can be programmed in the manner independently of the geometry of the particle, hence it can be applied to arbitrary shaped particles, without any change, and can also be easily applied to other shaped beams.

As mentioned before, there are few means to deal with light scattering of large non-spherical particle, even if the particle itself is homogeneous. The goal of this thesis is consequently to try to make a step forward in computation of light scattering by large non-spherical homogeneous particles with the MLFMA enhanced combined tangential formulation (CTF) of the surface integral equations (SIEs). To further strength its capability for large particles, a hybrid message passing interface (MPI) and open multi-processing (OpenMP) parallelization of MLFMA on a memory distributed computer system is done. In practice, the MLFMA-tree is first partitioned among processes to construct MPI parallelization. Tasks on each process are further accelerated by OpenMP multi-threading parallelization [58]. The hybrid parallelization is of high efficiency and compatible with configuration of mainstream distributed memory high performance computer platforms and make this algorithm capable to deal with arbitrary shape particles of size parameter larger than 600.

On the other hand, approximate methods, thought not exact, can deal with the scattering of large non-spherical particle. Among them, the geometrical optics, or ray model is the only candidate to treat the total problem of the scattering, i.e. the scattering in all direction, calculation of the cross-sections, the radiation pressure force, torque and stress. Some authors have contributed to the application of the GO to the prediction of the radiation pressure force [59]. Yang *et al.* have extended the GO to the calculation of the scattering matrix of non-spherical particle by combination to the integral method [19]. The main difficulty to apply the ray model in the scattering of an irregular shape particle is the evaluation the divergence/convergence of the wave on the curved surface of the particle. To cross this barrier, Ren *et al.* [22] have

developed the Vectorial Complex Ray Model (VCRM). A new intrinsic property of the rays – the curvature of wave front is introduced in the model. With this new property and by using vectors for ray tracing, this method is more accurate and flexible than the classical GO. The accuracy of VCRM has been investigated by comparing results with LMT for spherical particles and circular infinite cylinders. It has been successfully applied to the calculation of scattering by ellipsoidal particles and infinite elliptical cylinders. Various new physical phenomenons in light scattering by non-spherical particles have been revealed. It is proved to be applicable for any form of incident wave, any shape of object with smooth surface, and to predict with sufficient precision all scattering properties of the object. However, because it is essentially based on the approximate method of ray tracing, its validity is to be validated and its precision is to be evaluated. Hence, one of the main tasks of the thesis is to compare the results obtained by new developed algorithm of MLFMA with VCRM.

Numerical simulations of radiation pressure force and torque

Interaction between the light and a particle let the particle experience the radiation pressure force (RPF), torque and stress. This mechanical effect may push or pull the particle, and in certain conditions make it rotate or be deformed. The radiation pressure force and the torque are the overall net force and torque on a particle. The surface stress is a local mechanical effect due to the nonuniformity of the electromagnetic wave radiation on the particle.

RPF can be used to manipulate small particles without contact with the targets, which is especially useful in many applications. The requirement of very high intensity (gradient) makes RPF usable only with laser light sources. Such activities was initiated by Ashkin in 1970 [60]. In this work, a loosely focused laser beam was used to guide particles. Then the acceleration of microscopic particles by the radiation force was observed, pulling transparent particles with an index of refraction higher than the surroundings towards the beam axis. Later, other stable optical traps were demonstrated, including the optical levitation trap. In 1986, a foundational work was done by Ashkin and co-workers in the field of optical micromanipulation [61]. In their work, a particle was confined by a single tightly focused laser beam through a high numerical aperture lens. In such way, one can establish gradient forces on a particle counteracting the scattering forces in propagation direction. This simple but elegant

implementation of an optical trap enables the stable, three-dimensional optical trapping of dielectric particles and makes this manner widely used in nowadays as named optical tweezers.

Since the introduction of optical tweezers in 1986, it has become an important tool for research in the fields of biology, physical chemistry and soft condensed matter physics and greatly accelerate researches in these domains. A dual beam trapping can form a optical stretcher which is capable of trapping and stretching soft dielectrics, such as living biological cells [62, 63]. A parametric survey of various geometric, loading and structural factors has been done to develop quantitative models for the mechanics of deformation with the help of optical tweezers to study mechanical deformation of living cells under different stress states and the progression of some diseases [64]. Optical traps have been applied in the study of molecular motors and the physical properties of DNA [65]. Optical tweezers can be used to the confinement and organization of dielectric particles and to form an optical sorter for microscopic particles [66]. Also, it is believed that extended manipulation techniques will find application in microfluidic devices such as actuators, pumps, and valves [67] as well as possible application in micromachining tools [68, 69]. Like optical force, the optical torque can make rotation of an element without mechanical contact, so the device can be rotated while in a sealed environment [69].

As one of the most effective methods for manipulating micron and sub-micron sized particles, optical tweezers has widely been studied by scientists through both theoretical and experimental research. In the past few decades, work on numerical simulations also achieves good harvest and provides supports for experimental work.

The generalized Lorenz-Mie Theory (GLMT) is developed in 1980's by Gouesbet *et al.* [5] for the scattering of a a Gaussian beam by a homogeneous sphere. Ren *et al.* [70, 71] has applied it to the prediction of RPF exerted on a sphere. RPF exerted on arbitrarily located particles in Gaussian beam as well as associated resonance effects is studied [70]. Later, an improved standard beam description is presented by Polaert *et al.* [72]. They have calculated the RPF on a multilayered spherical particle by a focused Gaussian beam [73]. Lock studies on-axis and off-axis RPFs exerted by a tightly focused laser beam [8, 9]. However, trapping and manipulation of non-spherical particles is both very different and much less mastered than that of spheres. The case of a cylinder of circular cross section is reported [74]. Theoretical prediction of RPF exerted on a spheroid by an arbitrarily shaped beam is discussed by Xu *et al.* [12]. Recently, Xu *et al.* [75] provide an analytical solution to the radiation torque

exerted by an arbitrarily shaped beam on a spheroid. Nonetheless, much less work on the RPF and torque prediction for irregular particles has been reported. This is because the rigorous solutions of Maxwell equations exist only for the particles whose shape corresponds to a type of coordinates system. On the other hand, even for the regular shaped particle as spheroid or ellipsoid, the numerical evaluation of the special function is still another obstacle.

Approximate methods, such as ray optics, although not accurate enough, can provide acceptable approximation in the analysis of experimentally measured values [76, 77, 78]. Chang *et al.* [77] calculate the optical force on a ellipsoidal particle subjected to a loosely focused laser beam with the dynamic ray tracing method and find the ellipsoids levitated along the direction of the laser beam propagation will move horizontally with rotation. In [78], a 2-dimensional ray optics model is used to give explanations of the observed tumbling motion.

The T-matrix method is also used in the computation of RPF and torque. In this method, one needs first to calculate T-matrix, and then find VSWF representation of beam at the desired position within the trap for the desired orientation. Then the scattered fields are expressed in terms of VSWFs and the RPF and torque are finally computed by integrating the field around the particle. The most notable work in this domain has been presented by Nieminen *et al.* [79, 80, 81]. In [79], they calculated the axial force acting on particles of different shapes (spheroid and cylinder) and of volume equal to a sphere of radius $0.75\mu m$. The beam shape coefficients were calculated by the localized approximation. Later the work of Simpson *et al.* concerns T-matrix method for more complicated interactions associated with holographic assembly and present a general and flexible method, based on T-matrix method [82, 83, 84]. In [82], they investigated the optical interactions between pairs of particles in a single trap and in two separate traps, and proved that the T-matrix method is very versatile and it is expected to be valuable in studies of holographic nanoassembly. Simpson *et al.* have performed numerical studies on spheroids [83]. They found an interesting phenomenon: in a laser beam the prolate spheroids generally align with the symmetry axis parallel to the beam while the oblate spheroids always assume a perpendicular orientation. The long axis of the particle will align with the polarization direction. The rotation of absorbing spheres in Laguerre-Gaussian beams is also studied by using a large-sphere approximation for particle size parameter until 40 [84]. The T-matrix method is further extended to binary clusters composed of two identical, mutually contacting spheres of latex [85] (less than1 μm). In principle, the T-matrix method

can be used easily to predict the RPF of arbitrary shaped particles with any size parameters. However, so far as we know, there are few or none reports on particles of size more than ten microns or, in other words, of size parameter larger than 100. Moreover, this technique usually relies on central expansions of the electromagnetic field in VSWF. Arbitrary shaped particles of low rotational symmetry will increase time required to evaluate the T-matrix.

Because of its strong flexibility, DDA has also been used in computing RPF and torque. Draine calculated the radiation pressure force on a particle by a plane wave with DDA in 1988 [86]. In this paper, the radiation pressure cross section is computed for fluffy aggregates by computing the asymmetry parameter and the cross sections for extinction and scattering. Later, Draine and Weingartner present a series of work on radiation torque [87, 88, 89]. They are interested in radiation torque on irregular dust grains while at the same time, Kimura and Mann have also done notable work on computing RPF with DDA [90]. In all these researches, the total radiation force is numerically evaluated by an integral over the total space angle. Hoekstra *et al.* calculate the radiation forces on each dipole in the DDA model and then obtain the total radiation pressure on the particle by summation of the individual forces [91]. All of the above DDA based work for RPF and torque is for plane wave incidence and the particles are relatively small (less than ten micrometers).

In the last decade, work on the prediction of the RPF and torque by DDA on larger arbitrary shaped particles with shaped beams has been reported [92, 93, 94, 95, 96]. Bonessi *et al.* use DDA to obtain internal fields, and finally integrate the force densities given in equation over the volume of the particle [92]. The axial trapping forces are calculated for spheres and cubes and results have been then compared with the benchmarks. Chaumet *et al.* [93] have shown that the radiative reaction term must be taken into account to express the optical torque on a dipolar subunit. In their paper, they also compute optical torque on a micro-propeller illuminated by a right-handed circularly polarized wave. Simpson *et al.* present results of DDA calculations of the optical forces and torques experienced by a dielectric cylinder trapped horizontally in more than two Gaussian beams [94]. The rod emerged in water ($m = 1.33$) was $5\mu m$ in length, with a radius of $0.2\mu m$ and a refractive index of $m = 1.4663$. They have also evaluated the stiffness and strength of RPF as a function of the refractive index and radii of a dielectric cylinders held horizontally between pairs of Gaussian beams [95]. They pointed out that, these characteristic parameters are influenced in a similar way as spheres by optical resonances and by the relative dimensions of the

trapped particle and incident beam. Their results show that a rod can be trapped when the electric field is polarized perpendicular, but not parallel to their axes. Their latest work concern the optical forces and torques calculated by DDA and T-matrix method for lower symmetry particles and demonstrate excellent agreement [96]. These particles include dielectric spheres, geometrically and optically anisotropic particles, and also inhomogeneous core-shell particles.

Compared with scattering problems, much less work has been reported on the numerical computation of RPF and torque by using FDTD. When FDTD is used for computing RPF or torque by a shaped beam, Lorentz law of force or time average of the Poynting vector for the object under analysis instead of Maxwell's stress tensor is used [97, 98, 99, 100, 101]. Mansuripur *et al.* [99] analyzed the radiation pressure on a dielectric prism. They found that when the surrounding medium is a transparent liquid, the force of radiation on the body of the liquid should be included to achieve consistency with momentum based calculations. Gauthier computes the radiation pressure force on various dielectric objects including a dielectric thick walled shell by using the 2-D FDTD computation technique [100]. The RPF is obtained by computing the energy flow at the boundary of the FDTD grid domain with and without the trap object present. Liu *et al.* demonstrated a single tapered fiber optical tweezers system, and they calculated also both the axial and transverse trapping forces by using FDTD method [101]. Similarly to FDTD, although the FEM is powerful and has great capability for computing radiation or scattering, still much less work has been reported in computing RPF and torque. The only work we find is that by White [102].

We can conclude that in the literature the prediction of the RPF and torque is focused on two kinds of particles: spheres and particles of very small size. Because of the limitation of computational capability, less knowledge is known about possibilities to effectively trap larger particles with irregular shapes, neither experimentally nor theoretically. However, irregular shape particles such as nanotubes and nanorods are widely applied in biophysics, microfluidics, microelectronics and photonics [69, 103, 104]. Trapping of non-spherical particles is both very different and much less mastered than that of spheres [105]. Experimental researches on non-spherical particles find interesting phenomena greatly different from spherical particles. Cheng *et al.* find that disks stably trapped in bulk water will oscillate [106]. Neves *et al.* have shown that nano-fibres will switch to a strongly oblique orientation when it is brought in contact to the cover slip of the sample chamber [103]. Mihiretie *et al.* observed ellipsoids of

aspect ratio $k < 3$ trapped similarly to simple spheres, but for elongated particles with $k > 3$ it will not keep immobile but tumble [78]. Little formal interpretation is provided to explain these phenomenons. Theoretically study with the help of exact numerical simulation for 3D particles is perhaps a good way to help us achieving better understanding on radiation pressure force. Hence besides the study on light scattering by the MLFMA, the radiation pressure and torque on large non-spherical particles as well as the surface stress will be numerical analyzed in this thesis.

Structure of the dissertation

The remainder of the dissertation is organized as follows. Chapter 2 is devoted to the numerical computation and comparison of the scattering properties of large elliptical particles by using both the MLFMA and the VCRM. After a brief description of the two methods, the procedure on the hybrid MPI and OpenMP parallelized MLFMA is given. The numerical results for ellipsoidal particle of different aspect ratios obtained by VCRM and MLFMA are then compared. A series of numerical experiments are performed on Chebychev particles to show the performance of our algorithm. In Chapter 3, the SIE with MLFMA is applied to compute RPF and torque exerted by a shaped beam on homogenous particles of different shape. In MLFMA, the RPF is computed by vector flux of the Maxwell's stress tensor and the radiation torque is computed with the vector flux of the pseudotensor over a spherical surface tightly enclosing the particle separately. Thus, the analytical expressions for electromagnetic fields of incident beam in near region are used. Chapter 4 presents the study of the surface stress on soft homogeneous non-particles. Stress profiles on spheroids with different aspect ratios are computed. Physical analysis on mechanism of optical stress is given with help of VCRM. Computational study of stress on surface of a biconcave cell-like particle, which is a typical application in life science, is also undertaken. The last Chapter is dedicated to the conclusions and perspectives of the dissertation.

Chapter 2

Scattering diagrams calculated by VCRM and MLFMA

In various research fields, we need to simulate the scattering of light by particles with complex shapes, such as in multiphase flow, atmospheric radiative transfer, bio-optics and climate study. In fact, particles encountered in nature, in industry and in laboratories (spray of atomization, ice crystals, dust aerosols, raindrops and cells in biophysical systems) are often irregularly shaped and having a wide range of sizes. As already discussed in Chapter 1, existing rigorous methods such as the LMT and GLMT are able to predict the scattering properties for particles of simple shapes. However, when the shape of the particles is more complex, numerical methods must be used. If the size parameter of irregular shape particles is much larger than the incident wavelength, approximate methods such as GO can be applied.

In principle, the geometrical optics can be applied to deal with the interaction between light and objects of any shapes. But in reality, it is rarely used in quantitative study of particle scattering by non-spherical, non-circular cylindrical particles. Many researchers have contributed to the improvement of geometrical optics in different angles, some take into account special effects, others combine it with the electromagnetic wave method to predict the total scattering properties such as the scattering matrix [107, 108, 109, 110, 111]. But, few researchers have examined the scattering diagrams for non-spherical particles. However, the scattering diagrams are important in both theoretical and practical points of view since they reveal the physical mechanism of scattering and the typical information in certain angles (rainbow and critical angles for example) are of particular interest in applications such as the optical metrology in multiphase flow. For instance Hovenac *et al.* have examined the scattering diagrams

of a sphere around rainbow angles by GO, Airy theory, Debye series and have discussed also the contribution of the surface waves [107]. By comparison with the Lorenz-Mie theory, Xu *et al.* have shown that by takeing into account the interference and diffraction effect in forward direction, GO can correctly predict the scattering diagram of a sphere in all direction [112, 113].

But the approach used by Hovenac *et al.* [107] and Xu *et al.* [112] can only be applied to a homogeneous sphere and an infinite circular cylinder. Lock has studied the scattering of a spheroid by ray model [114, 115]. He has shown that it is possible to obtain analytical equations to describe the ray properties but the numerical calculation is limited only to the reflection and the first refraction rays ($p = 1$) because of the difficulty in the solution of the equations. Later, Yuan attempted to solve this problem numerically but did not succeeded even in the simplest case: scattering in the symmetrical plane of an elliptical particle illuminated by a plane wave [116].

The key problem is the divergence/convergence of a wave on the surface of the particle. To overcome these difficulties, Ren *et al.* have introduced a new wave property – wave front curvature and developed a new model: the VCRM [22, 117]. The wave front curvature considers the wavelike behaving of light, the convergence or divergence of the wave. Thus, a ray is described not only by its amplitude, phase, polarization, propagation direction, but also by the curvatures of the local wave front of the wave that the ray presents. All these features evolve at each interaction of ray with the particle surface. Particularly, the curvature matrix of the emergent wave after each interaction of the ray with the particle surface is calculated according to the curvature matrix of the incident wave and the local curvature of the particle surface by using the wave front equation. The significant benefits of this approach are: the wave properties are integrated in the ray model; the divergence/convergence of the wave is deduced by the wave front curvature; the phase shift due to the focal lines is determined directly by the curvature of the wave front. Hence it can be used to obtain a quite accurate scattering diagram in all directions and the scattering properties of an object of any shape with smooth surface illuminated by an arbitrarily shaped beam. This model has already been applied successfully for computing scattering of large ellipsoids and infinite long elliptical cylinders with the plane wave or shaped beam incidences [22, 117, 118]. However, the results of VCRM are to be validated because neither theoretical nor numerical methods exist to predict with precision the scattering properties of so large non-spherical particles.

Full wave numerical methods, although time consuming and needing large amounts

of CPU memory, are very flexible in term of the particle shape. With the development of super computer technology, the CPU memory capacity becomes larger and larger, the computation speed becomes faster and faster. So the calculable size of the particle can be solved with full wave numerical method increase, from about one wavelength to tens of wavelengths. With the help of parallelization technique, this size limit can be further increased to hundreds of wavelengths. Among various numerical methods, SIE method is especially suitable for large homogeneous particles. By using the MLFMA to speed up matrix-vector multiplication in the iterative solution of the final SIE matrix equation system, CPU time and memory resources need can be greatly reduced. The code MLFMA I develped with hybrid MPI and OpenMP parallelization can be applied to very large particles with size parameter bigger than 600.

In this chapter, after the description of the general principle of VCRM and MLFMA for light scattering problems, the comparison between the diagrams calculated by MLFMA and VCRM for elliptical particles is given and discussed. At the end, some scattering diagrams computed for large Chebychev particles are provided to demonstrate the capability and flexibility of our algorithm.

2.1 Vectorial Complex Ray Model

In the Vectorial Complex Ray Model (VCRM), all waves are described by bundles of vectorial complex rays having five properties. Besides the direction, the amplitude, the polarization and the phase, the wavefront curvature of the wave is introduced. Furthermore, the wave vector $\boldsymbol{k}$ is used to describe the direction of a vectorial complex ray which simplifies considerably the calculation.

According to the continuity of the tangent component of the wave vector on the interface of the particle, Snell's law can be written as

$$k'_\tau = k_\tau \tag{2.1}$$

where k'_τ and k_τ are respectively the tangent components of the wave vectors $\boldsymbol{k}$ and $\boldsymbol{k}'$ of the rays before and after interaction (reflection or refraction). Then the normal component of the emergent ray is given by

$$k'_n = \sqrt{k'^2 - k_\tau^2} \tag{2.2}$$

We assume the curvature of the particle surface in the vicinity of the incident point of a ray to be described by matrix C; the curvatures of the incident and refracted/reflected

wave fronts are expressed, respectively, by the matrices Q and Q'(see Fig. 2.1). The

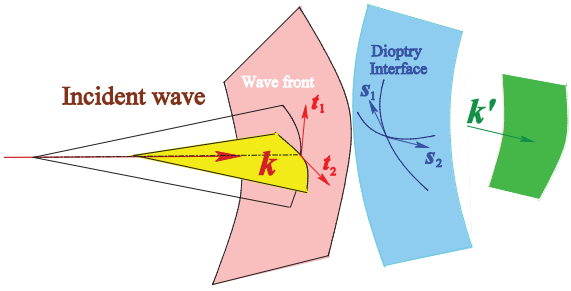

Figure 2.1: Schematic of the interaction of the wavefront and surface.

projection matrix between the base unitary vectors $(\boldsymbol{t}_1, \boldsymbol{t}_2)$ of the coordinates systems on the planes tangent to the wavefront and to the dioptric surface$(\boldsymbol{s}_1, \boldsymbol{s}_2)$ is Θ:

$$\Theta = \begin{pmatrix} \boldsymbol{s}_1 \cdot \boldsymbol{t}_1 & \boldsymbol{s}_1 \cdot \boldsymbol{t}_2 \\ \boldsymbol{s}_2 \cdot \boldsymbol{t}_1 & \boldsymbol{s}_2 \cdot \boldsymbol{t}_2 \end{pmatrix} \tag{2.3}$$

Then the relation between these three curvature matrices is given by the following wavefront matrix equation [22]

$$(\boldsymbol{k}' - \boldsymbol{k}) \cdot \boldsymbol{n} C = k' \Theta'^T Q' \Theta' - k \Theta^T \, Q \Theta \tag{2.4}$$

where $\boldsymbol{n}$ is the normal of the dioptric surface (i.e., the particle surface), the superscript T represents the transposition operator, the letters with or without the prime represent respectively the values after or before interaction of the ray with the surface. If we are interested in 2D problems, in which the scattering in the plane defined by the symmetric axis of the particle and the direction of the incident plane wave, the curvature matrices described in the two main directions are diagonal:

$$C = \begin{pmatrix} \frac{1}{\rho_1} & 0 \\ 0 & \frac{1}{\rho_2} \end{pmatrix} \tag{2.5}$$

$$Q = \begin{pmatrix} \frac{1}{R_1} & 0 \\ 0 & \frac{1}{R_2} \end{pmatrix} \tag{2.6}$$

$$Q' = \begin{pmatrix} \frac{1}{R'_1} & 0 \\ 0 & \frac{1}{R'_2} \end{pmatrix} \tag{2.7}$$

where ρ_1 and ρ_2 are the two principal curvature radii of the particle surface at the incident point. R_1 and R_2 the principal curvature radii of the wavefront before interaction, and R'_1, R'_2 those of the wavefront after interaction. They satisfy the two

simplified scalar wave front equations:

$$\frac{k' \cos^2 \theta_r}{R'_1} = \frac{k \cos^2 \theta_i}{R_1} + \frac{k' \cos \theta_r - k \cos \theta_i}{\rho_1} \tag{2.8}$$

$$\frac{k'}{R'_2} = \frac{k}{R_2} + \frac{k' \cos \theta_r - k \cos \theta_i}{\rho_2} \tag{2.9}$$

where θ_i and θ_r are respectively the incident and refraction angles. In VCRM the divergence factor D is introduced to describe the divergence/convergence of the wave and it is determined directly by the curvature radii of wavefronts as follows

$$\mathcal{D} = \frac{R'_{11} R'_{21}}{R_{12} R_{22}} \cdot \frac{R'_{12} R'_{22}}{R_{13} R_{23}} \cdots \frac{R'_{1p} R'_{2p}}{(r + R'_{1p})(r + R'_{2p})} \tag{2.10}$$

where r is the distance between the origin of the coordinate system and the observation point. The index p is the order of the ray. R_{1j} and R_{2j} $(j = 1, 2, \cdots, p)$ represent the two curvature radii of the wavefront of incident ray at j^{th} interaction with the surface. R'_{1j} and R'_{2j} are the corresponding curvature radii of the refracted ray.

To take into account the effect of interference, generally, the phase of each ray must be computed which is composed of four parts:

$$\Phi = \Phi_{inc} + \Phi_{pth} + \Phi_{Frs} + \Phi_{fcl} \tag{2.11}$$

1. The phase Φ_{inc} of the incident wave is calculated directly according to the wave front of the incident wave expression.

2. The phase Φ_{pth} due to the optical path is calculated according to the optical path in and out the particle relative to the reference ray passing by the center of the particle.

3. The phase due to the reflection or refraction Φ_{Frs} is included in the Fresnel coefficients which are calculated with the normal components of the wave vectors of the incident wave k_n and the refracted wave k'_n ($k'_n = -k_n$ for reflected wave).

$$r_1 = \frac{k_n - k'_n}{k_n + k'_n} \tag{2.12}$$

$$r_2 = \frac{m^2 k_n - k'_n}{m^2 k_n + k'_n} \tag{2.13}$$

$$t_1 = \frac{2k_n}{k_n + k'_n} \tag{2.14}$$

$$t_2 = \frac{2mk_n}{m^2 k_n + k'_n} \tag{2.15}$$

where r_X and t_X stand for the reflection and refraction ratios, and $X = 1, 2$ for perpendicular and parallel polarizations.

4. The phase shift due to the focal lines Φ_{fcl}. Each time a ray passes a focal line, the phase advances $\pi/2$. To do so, it is only necessary to count the number of sign change of the curvature radii between two successive interactions.

The complex amplitude of a ray is calculated by the product of three terms, the Fresnel coefficients, the divergence factor and the absorption factor, with

$$S_{X,p} = \sqrt{\mathcal{D}_p}\ \ |S_G|\, \varepsilon_{X,p} A_p e^{i\Phi} \tag{2.16}$$

where S_G the amplitude of the incident wave, A_p is the absorption factor, which can be evaluated by the attenuation factor as function of the distance of the ray in the particle [119] according to

$$A_p = \exp\left(-m_i \sum_{q=1}^{p} k'_{n,q} d_q\right) \tag{2.17}$$

where m_i is the imaginary part of the refractive index. d_q denotes the distance that the ray crosses in the particle. $k'_{n,q}$ is the component of the wave vector normal to the particle surface. The total amplitude of the scattering field at a given angle is just the summation of all rays.

In this chapter we are interested in a relative simple case: scattering of a plane wave by a homogeneous ellipsoidal particle. The incident direction is in a symmetrical plane of the particle so that all the rays remain in the same plane.

An ellipsoidal particle is described by

$$\frac{x^2}{a^2} + \frac{y^2}{b^2} + \frac{z^2}{c^2} = 1 \tag{2.18}$$

where a, b and c are respectively the semi-axes of ellipsoid in x, y and z directions (Fig. 2.2. The scattering diagrams are observed in the plane $y = 0$. The two curvature radii in the two principal directions are given by

$$\rho_1 = \frac{c^2}{a}\left[1 + \left(a^2/c^2 - 1\right) z^2/c^2\right]^{3/2} \tag{2.19}$$

$$\rho_2 = \frac{b^2}{a}\left[1 + \left(a^2/c^2 - 1\right) z^2/c^2\right]^{1/2} \tag{2.20}$$

according to the coordinate z of the impact point of the ray.

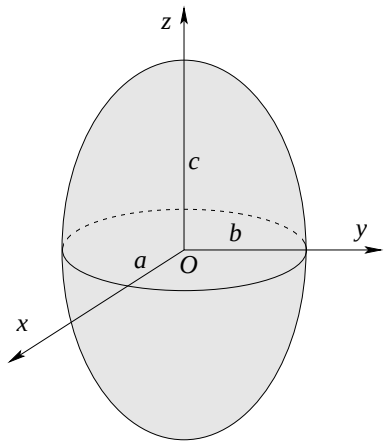

Figure 2.2: Geometry of a triaxial ellipsoid.

In summary, Eqs. (2.1), (2.2) and (2.18) permit to determine the interaction points of rays and their directions. The divergence/convergence of the wave is calculated according to Eqs. (2.4), (2.19), (2.20), (2.8), (2.9) and (2.10), and the amplitude of the rays are deduced from Eqs. (2.12)-(2.15), (2.16) and (2.17). Then the final amplitude in a given direction is calculated by summing all the complex rays arriving in that direction.

2.2 Combined tangential formulation with MLFMA

The surface integral equation (SIE) approach is often preferred for homogeneous objects because it limits the discretization of the unknowns to the surface of the object and the discontinuous interfaces between different materials [49]. In this section, we give a brief description of the SIE method for homogeneous dielectric objects. For a dielectric object, using either the equivalence principle or the vector Green's theorem, we can formulate a set of integral equations to calculate the electric and magnetic fields $(\mathbf{E}, \mathbf{H})$ in terms of equivalent electric and magnetic currents $(\mathbf{J}, \mathbf{M})$. The boundary S of the dielectric object is taken as the equivalent surface, as shown in Fig. 1, with the incident beam denoted as $(\mathbf{E}^i, \mathbf{H}^i)$ and the equivalent sources as $(\mathbf{J}, \mathbf{M})$. Four basic integral equations are expressed in the homogeneous medium: the electric field integral equation outside the dielectric body (EFIE-O), the magnetic field integral equation outside the dielectric body (MFIE-O), the electric field integral equation inside the dielectric body (EFIE-I), and the magnetic field integral equation

inside the dielectric body (MFIE-I) [49]:

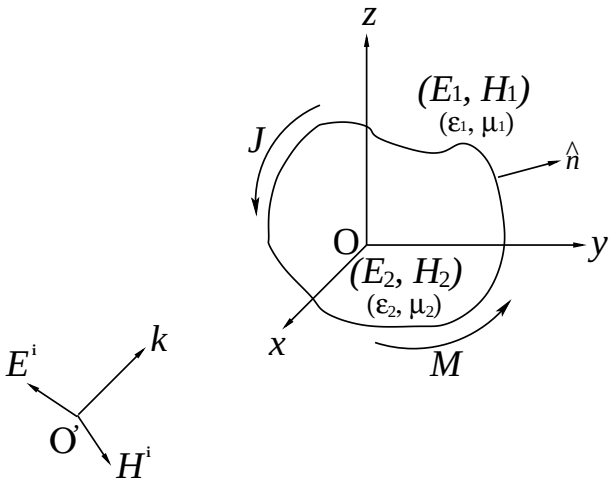

Figure 2.3: Sketch of three dimensional homogeneous dielectric object.

$$\text{EFIE-O:} \qquad \mathbf{E}_1 - Z_1\mathbf{L}_1(\mathbf{J}) + \mathbf{K}_1(\mathbf{M}) = \mathbf{E}^i \tag{2.21}$$

$$\text{MFIE-O:} \qquad \mathbf{H}_1 - Z_1^{-1}\mathbf{L}_1(\mathbf{M}) - \mathbf{K}_1(\mathbf{J}) = \mathbf{H}^i \tag{2.22}$$

$$\text{EFIE-I:} \qquad \mathbf{E}_2 - Z_2\mathbf{L}_2(\mathbf{J}) + \mathbf{K}_2(\mathbf{M}) = 0 \tag{2.23}$$

$$\text{MFIE-I:} \qquad \mathbf{H}_2 - Z_2^{-1}\mathbf{L}_2(\mathbf{M}) - \mathbf{K}_2(\mathbf{J}) = 0 \tag{2.24}$$

where $Z_l = (\mu_l/\varepsilon_l)^{1/2}$ denotes the wave impedances in medium l with $l = 1, 2$ respectively for medium outside and inside object. The operators $\mathbf{L}_l$ and $\mathbf{K}_l$ are defined as:

$$\mathbf{L}_l\{\mathbf{X}\}(\mathbf{r}) = jk_l \int_S [\mathbf{X}(\mathbf{r}') + \frac{1}{k_l^2}\nabla(\nabla' \cdot \mathbf{X}(\mathbf{r}'))]G_l(\mathbf{r}, \mathbf{r}')d\mathbf{r}' \tag{2.25}$$

$$\mathbf{K}_l\{\mathbf{X}\}(\mathbf{r}) = \int_S \mathbf{X}(\mathbf{r}')\times\nabla' G_l(\mathbf{r}, \mathbf{r}')d\mathbf{r}' \tag{2.26}$$

where $j = \sqrt{-1}$, $k_l = \omega(\mu_l/\epsilon_l)^{1/2}$, $\mathbf{X}$ is either the equivalent electric current $\mathbf{J}$ or the equivalent magnetic current $\mathbf{M}$ on the surface of the object, and

$$G(\mathbf{r}, \mathbf{r}') = \frac{\exp(-jk_l|\mathbf{r} - \mathbf{r}'|)}{4\pi|\mathbf{r} - \mathbf{r}'|} \tag{2.27}$$

In order to overcome the resonance problem, the combined field integral equation is used. We can combine the electric field integral equation with the magnetic field integral equation, or the internal integral equation with the external integral equation. Various forms of combined field integral equations can be constructed, such as the

Poggio-Miller-Chang-Harrington-Wu-Tsai(PMCHW) equations [120], the Combined tangential formulation(CTF), the combined normal formulation(CNF) and the electric and magnetic current combined-field integral equations(JMCFIE) [121]. Among those forms of combined equations, the nature of CTF equations is close to a first-kind integral equation and its accuracy is the best, especially when dealing with objects with sharp edges, corners or high dielectric constant. The equation form of CTF can be expressed as follow:

$$\begin{cases} Z_1^{-1}\hat{\mathbf{t}} \cdot (\text{EFIE-O}) + Z_2^{-1}\hat{\mathbf{t}} \cdot (\text{EFIE-I}) \\ Z_1\hat{\mathbf{t}} \cdot (\text{MFIE-O}) + Z_2\hat{\mathbf{t}} \cdot (\text{MFIE-I}) \end{cases} \tag{2.28}$$

where $\hat{\mathbf{t}}$ is the tangential vector at a point on the surface. Eq. (2.28) can be discretized by first expanding $(\mathbf{J}, \mathbf{M})$ as:

$$\mathbf{J} = \sum_{i=1}^{N_s} \mathbf{g}_i J_i \qquad \mathbf{M} = \sum_{i=1}^{N_s} \mathbf{g}_i M_i \tag{2.29}$$

where N_s denotes the total number of edges on S and $\mathbf{g}_i$ denotes the Rao, Wilton and Glisson(RWG) vector basis functions [51]. In implementation, the surface of the particle is modeled by using small triangular patches, such work can be done with the help of commercial software. The RWG basis functions are associated with the edges of the triangular patches. By substituting Eq. (2.29) into Eq. (2.28) and applying $\mathbf{g}_i$ as the trial functions for the tangential field equations, a complete matrix equation system can be obtained. This numerical solution process is well known as the method of moment (MoM). By solving this matrix equation with iterative solvers, such as the generalized minimal residual method (GMRES), the equivalent sources $(\mathbf{J}, \mathbf{M})$ on the surface S can be known. Such procedure is well known as the method of moments (MoM).

$$\begin{bmatrix} \mathbf{Z}_{11} & \mathbf{Z}_{12} \\ \mathbf{Z}_{21} & \mathbf{Z}_{22} \end{bmatrix} \begin{bmatrix} \mathbf{J} \\ \mathbf{M} \end{bmatrix} = \begin{bmatrix} \mathbf{f}_1 \\ \mathbf{f}_2 \end{bmatrix} \tag{2.30}$$

with

$$\mathbf{Z}_{11}[m,n] = \mathbf{Z}_{22}[m,n] = \int_S \mathbf{g}_m \cdot \mathbf{L}_1(\mathbf{g}_n)\, d\mathbf{r} + \int_S \mathbf{g}_m \cdot \mathbf{L}_2(\mathbf{g}_n)\, d\mathbf{r} \tag{2.31}$$

$$\mathbf{Z}_{12}[m,n] = -(1/Z_1)\int_S \mathbf{g}_m \cdot \mathbf{K}_1(\mathbf{g}_n)\, d\mathbf{r} - (1/Z_2)\int_S \mathbf{g}_m \cdot \mathbf{K}_2(\mathbf{g}_n)\, d\mathbf{r} \tag{2.32}$$

$$\mathbf{Z}_{21}[m,n] = Z_1 \int_S \mathbf{g}_m \cdot \mathbf{K}_1(\mathbf{g}_n)\, d\mathbf{r} + Z_2 \int_S \mathbf{g}_m \cdot \mathbf{K}_2(\mathbf{g}_n)\, d\mathbf{r} \tag{2.33}$$

$$\mathbf{f}_1[m] = -(1/Z_1) \int_S \mathbf{g}_m \cdot \mathbf{E}^i(\mathbf{r})\, d\mathbf{r} \tag{2.34}$$

$$\mathbf{f}_2[m] = -(1/Z_1) \int_S \mathbf{g}_m \cdot \mathbf{H}^i(\mathbf{r})\, d\mathbf{r} \tag{2.35}$$

When the surface integral equations are used to analyze a dielectric object, the triangle meshes used to discrete the surface S must be dense if the dielectric constant of the medium is big. Moreover, the number of unknowns is double compared to the metal since both the equivalent electric and magnetic currents exist on the surface. Therefore MoM is conventionally limited to dealing with electrically small dielectric objects due to the computational and storage complexity of $O(N^2)$, with N the number of unknowns. To circumvent this problem, matrix-vector multiplications are performed with various acceleration methods, such as FFT, AIM and MLFMA [52, 122, 53]. Among these acceleration methods, the MLFMA has been well developed and can be used to solve challenging problems. Hence, the multilevel fast multipole algorithm (MLFMA) is employed here to speed up matrix-vector multiplication and reduce the memory requirements. By using the MLFMA, both the time and memory complexity can be reduced to $O(NlogN)$ [123, 49, 52]. We describe briefly in the following how to use MLFMA in CTF formulation. More details can be found in [49, 52].

In MLFMA, interactions between the basis and testing elements can be divided into two types: near interactions and far interactions. For near interactions, they are computed directly in the same way as those in MoM and stored as a sparse matrix. However, for far interactions, we first construct a tree structure of levels by placing the scatterer in a cubic box and recursively dividing the computational domain into sub-boxes. Then MLFMA calculates the interactions between the basis and testing elements, which are far from each other, in a group-by-group manner consisting of three stages called aggregation, translation, and disaggregation [49]. It can be known from Eq. (2.28), because both the operators $\mathbf{L}$ and $\mathbf{K}$ are involved in the matrix equation of CTF, we need to solve only two types of multiplication which can be

expressed in terms of the multipole expansion as follows [49]:

$$\langle \mathbf{g}_i, \mathbf{L}_l(\mathbf{g}_j)\rangle = k_l^2(4\pi)^{-2}\oint \mathbf{V}_{1l}T_l(\hat{\mathbf{k}}\cdot\hat{\mathbf{r}}_{mm'})\mathbf{V}_l' d^2\hat{\mathbf{k}} \tag{2.36}$$

$$\langle \mathbf{g}_i, \mathbf{K}_l(\mathbf{g}_j)\rangle = k_l^2(4\pi)^{-2}\oint \mathbf{V}_{2l}T_l(\hat{\mathbf{k}}\cdot\hat{\mathbf{r}}_{mm'})\mathbf{V}_l' d^2\hat{\mathbf{k}} \tag{2.37}$$

where the aggregation terms $\mathbf{V}_{1l}$ and $\mathbf{V}_{2l}$, the disaggregation term $\mathbf{V}_l'$, and the translation term T_l are explicitly expressed as:

$$\begin{aligned}
&\mathbf{V}_{1l} = \textstyle\int_S e^{-j\mathbf{k}_l\cdot\mathbf{r}_{im}}(\overleftrightarrow{I} - \hat{\mathbf{k}}\hat{\mathbf{k}})\cdot\mathbf{g}_i dS\\
&\mathbf{V}_{2l} = \textstyle\int_S e^{-j\mathbf{k}_l\cdot\mathbf{r}_{im}}(\hat{\mathbf{k}}\times\mathbf{g}_i) dS\\
&\mathbf{V}_l' = \textstyle\int_{S'} e^{-j\mathbf{k}_l\cdot\mathbf{r}_{jm'}}\mathbf{g}_j dS'\\
&T_l = \sum_{n_l=0}^{L}(-j)^{n_l}(2n_l+1)h_{n_l}^{(2)}(k_l r_{mm'})P_{n_l}(\hat{\mathbf{k}}\cdot\hat{\mathbf{r}}_{mm'})
\end{aligned} \tag{2.38}$$

where $\overleftrightarrow{I}$ denotes the 3×3 unit dyad and the integral is evaluated on the unit sphere, $\mathbf{k}_l = k_l\hat{\mathbf{k}}$. $\mathbf{g}_i$ and $\mathbf{g}_j$ are the basis functions at i^{th} and j^{th} edges which reside in the groups m or m' centered at $\mathbf{r}_m$ and $\mathbf{r}_{m'}$ respectively, and we note $\mathbf{r}_{im} = \mathbf{r}_i - \mathbf{r}_m$, $\mathbf{r}_{jm'} = \mathbf{r}_j - \mathbf{r}_{m'}$ and $\mathbf{r}_{mm'} = \mathbf{r}_m - \mathbf{r}_{m'}$. $h_{n_l}^{(2)}$ denotes the spherical Hankel function of the second kind, P_{n_l} the Legendre polynomial of degree n_l, and L the number of multipole expansion terms. Then, MLFMA can be used to accelerate matrix-vector multiplication in the iterative solving process of the resultant equation matrix.

Compared with the MLFMA for PEC targets, another set of tree structure for inner medium is needed. In each matrix-vector multiplication, four-fold and eight-fold of CPU time is needed respectively for near and far interactions. For large targets discretized into millions of unknowns, memory requirement for storing those matrices for far interaction groups increases significantly. For lossless homogenous space, its wave number k is a real constant. By using symmetry of the aggregation matrix, disaggregation matrix, and shifting matrix [55], the total memory requirement can be halved for the aggregation and disaggregation matrices while the memory requirement for the shifting matrix is reduced by a factor of four in our program by partly using symmetry to keep high efficiency [57]. However, for lossy homogenous space, k is a complex constant and has a imagine part. In such condition, MLFMA will lose most of its symmetry. However, we can still use symmetry of the center shifting matrix as usual with a small change as:

$$e^{-jk_l\hat{d}\cdot\hat{k}} = \frac{1}{e^{jk_l\hat{d}\cdot\hat{k}}} \tag{2.39}$$

Problems involving more complicated objects may require effective preconditioners. Tahir Malas and Levent Gurel proposed several kinds of preconditioners constructed from the near interaction matrix of the MLFMA [124], among which the approximate Schur preconditioner (ASP) is proved to have the best convergence and most efficient. However, ASP is a complex and time-consuming preconditioning approach, and it also requires more memory because two approximate matrix inverses need to be computed with the sparse approximate inverse (SAI) method [124]. For electrical large problems involving more than tens of millions unknowns, such extra computation costs are usually not preferable. Therefore, here we employ the lower triangular approximate Schur preconditioner (LTASP) to reduce the complexity of constructing preconditioning matrix.

$$\mathbf{M}^{-1} = \begin{bmatrix} \left(\bar{\mathbf{Z}}_{11}\right)^{-1} & 0 \\ 0 & \left(\bar{\mathbf{Z}}_{11}\right)^{-1} \end{bmatrix} \begin{bmatrix} I & 0 \\ -\mathbf{Z}_{21}\left(\bar{\mathbf{Z}}_{11}\right)^{-1} & I \end{bmatrix} \tag{2.40}$$

For electrically large problems with more than tens of millions unknowns to be solved, a sequential implementation of MLFMA is not sufficient. In order to solve such extremely large problems, MLFMA can be parallelized on distributed-memory architectures with different strategies increasing the problem size from tens of millions to hundreds of millions in the last decade mostly for perfect electric conductor (PEC) targets [55, 56, 57]. Recently, MPI based parallel implementations of the MLFMA for solutions of problems involving homogeneous objects with diverse material properties are presented [125, 126]. However, the simple MPI parallel schemes always perform inefficiently because of extensive communications among processes, poor load-balance, and unavoidable duplications of data. A flexible and efficient hybrid MPI-OpenMP paralleled MLFMA (MPI-OpenMP-MLFMA) is used here. MLFMA is parallelized using the hybrid partitioning strategy. The MLFMA-tree is partitioned among processes to conduct MPI parallelization. Tasks on each process are further accelerated by OpenMP multi-threading parallelization [58]. Such hybrid MPI-OpenMP paralleled MLFMA is proved to have the great capability for solving PEC problems modeled with as many as one billion unknowns. In the MPI-OpenMP-MLFMA, similar to the hybrid partitioning strategy, a transition level is adopted. And then, a user-specified number of OpenMP threads are forked in each MPI process. Hence the number of processes is cut down a lot while the total number of computing units remains constant. The transition level can be moved down to a finer level in the MLFMA tree structure compared with the conventional hybrid MLFMA while compared with the

hierarchical strategy of MLFMA, the MPI-OpenMP-MLFMA generally has a better scalability because the additional overhead to modify data partition is completely avoided. Here we do not give a detail description of this MPI-OpenMP-MLFMA, readers can refer to [58] for technical details.

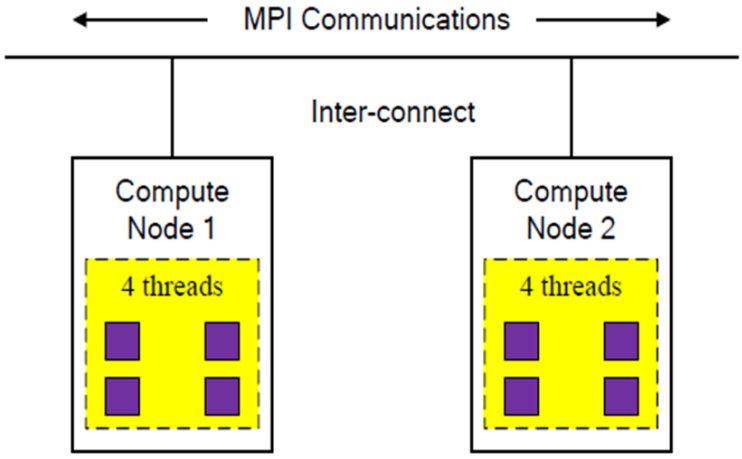

Figure 2.4: Schematic of hybrid MPI and OpenMP on mainstream high performance computer platform.

In MLFMA, total CPU time is the main cost by the following parts: CPU time for constructing matrices, including these for near field interaction and for multipole expansion, with complexity of $O(NlogN)$, we call it matrix filling time; CPU time for iterative solution of the final matrix equation system with complexity of $O(NlogN)$, we call it solution time; CPU time for computing scattering properties, with $O(N_pN)$ complexity of and (N_p) the number of required observing angles. Also there is CPU time used for constructing a preconditioner with complexity of $O(NlogN)$ if the SAI technique is employed. For a given particle and a given incident wavelength, matrix filling and precondition constructing process need to be done for only once; iterative solution and computing of scattering properties need to be performed for different incident waves. Generally speaking, compared with these other three steps, CPU time for computing scattering properties after obtaining the equivalent electromagnetic currents $(\mathbf{J}, \mathbf{M})$ can be nearly ignored. An example is given in Table 2.1 for an ellipsoid of aspect ratios $k_1 = 3.5$, $k_2 = 2.0$ and size parameter equals to 220. The CPU time for the calculation of the scattering diagrams is only 0.6% of the total CPU time for 1801 observe angles.

Table 2.1: CPU time in seconds for different scattering angle numbers

Number of scattering angles	181	1801
CPU time for solving SIE ($\times 10^3$)	27.795	27.795
CPU time for scattering calculation($\times 10^3$)	0.017	0.168

2.3 Numerical results

For the computations performed in this section, the incident plane wave propagates always along z axis and the orientation of the particle is described by the conventional Euler angles α, β and γ denoting respectively the angles of rotations about z axis, the temporary y' axis and z'' axis. We define a triaxial ellipsoid of the semi-axes a, b, c along the x, y and z directions respectively as shown in (Fig. 2.2). The shape of the particle is characterized by a couple of aspect ratios, defined as $k_1 = b/a, k_2 = c/a$. Hence we have $k_1 = k_2 = 1$ for a sphere, $k_1 = k_2$ for a spheroid and $k_1 \neq k_2$ for a triaxial ellipsoid. The size parameter is defined in terms of a volume-equivalent sphere for all the cases.

Before the study of the effects of the size parameter and the aspect ratios on the scattering properties for large spheroids, we validate our code by comparison with the results of an independent code, i.e. the open source software ADDA [127]. We have intended to compare their results with ADDA for large particles directly, but the ADDA we have used failed to converge when the size of the particle is large. Perhaps there is no precondition employed in ADDA to make sure convergence of the iterative sovler it employed. Hence we compare only our MLFMA results with those from ADDA for a relatively small particle. Fig. 2.5 shows the scattering matrix elements S_{11}, $-S_{12}/S_{11}$, $-S_{21}/S_{11}$, S_{22}/S_{11} calculated by MLFMA and DDA. The size parameter of the ellipsoid is fixed to 4.4 and its aspect ratios are $k_1 = 1.4$ and $k_2 = 2.0$. The Euler angles are set to $\alpha = 30°$, $\beta = 15°$ and $\gamma = 0°$. The scattering angle step in the calculation is taken to be 0.1°. It is found that the agreement between the two methods is excellent for these scattering matrix elements.

After validating our MLFMA code by comparing results with DDA, we will perform a series of numerical experiments. We divide this section into two parts, the first one for the comparison of VCRM and MLFMA for plane wave scattering by a large ellipsoidal particles. We want to validate the VCRM with the full wave numerical method MLFMA, which is flexible in shape of the particle. The computed particles include prolate spheroids and oblate spheroids with different aspect ratios, as well as

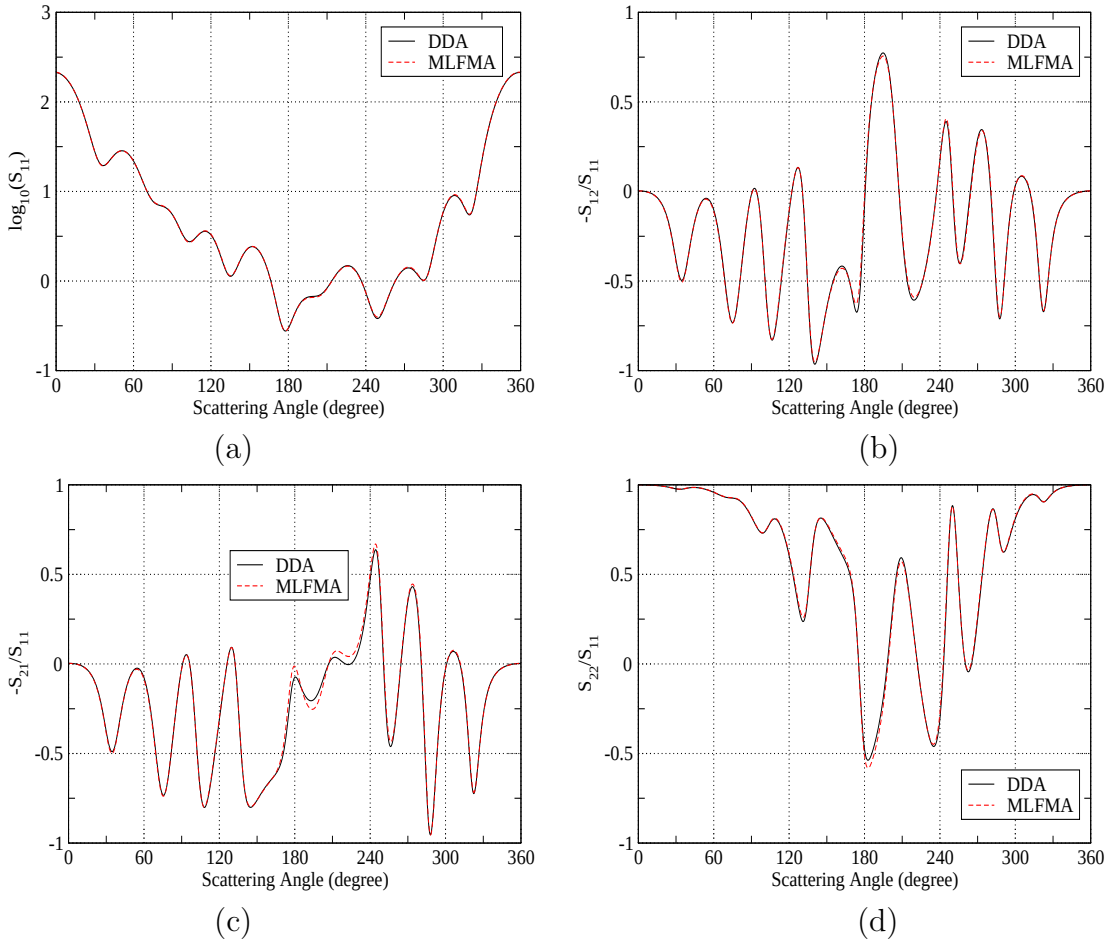

Figure 2.5: Comparison of scattering matrix elements computed by MLFMA and DDA for a triaxial ellipsoid ($x = 4.4$, $k_1 = 1.4$, $k_2 = 2.0$ and $m = 1.555 + 0.004i$) illuminated by the plane wave of wavelength 0.633 μm. The ellipsoid is rotated with Euler angles $\alpha = 30°$, $\beta = 15°$ and $\gamma = 0°$ and the observation is in yz plane.

an ellipsoid. The second part is devoted to numerical study of the scattering matrix elements of large ellipsoidal particles with different size parameters and aspect ratios, as well as a Chebshev particle with different size parameters.

2.3.1 Comparisons of VCRM and MLFMA for scattering by large spheroidal particles

In this subsection, we focus on the validation of VCRM by comparing the scattering diagrams of large ellipsoidal particles calculated with the results of MLFMA code we developed. Since the accuracy of MLFMA has been validated by another numerical method DDA, and in theory these two numerical methods are flexible in shape of the particle, here we choose results computed by our MLFMA as the reference. The wavelength of the incident plane wave is fixed to 0.785 μm and the refractive index of the particle is set to $m = 1.33$. In all the results computed by VCRM, the maximum order of rays is set to 12 with total 4000 number of rays and 10000 scattered rays. The diffraction effect, which is very important in the forward direction, is also taken into consideration by using the simple model given in [22][22].

In principle, the ray model is only valid for particles of size much larger than the incident wavelength. The first example we give here is for the comparison of VCRM and MLFMA with LMT for a large sphere. A water droplet with radius 50 μm is computed. The results obtained by LMT, VCRM and MLFMA are plotted in Fig. 2.6. It can be seen from this figure that both VCRM and MLFMA are in agreement with LMT especially in the forward and backward direction. But there are slight differences between VCRM and LMT around 90° and the Alexander's dark region while MLFMA agrees perfectly with LMT. This is because in VCRM the surface wave effect has not yet been taken into consideration. The scattering diagrams computed by VCRM and MLFMA for the incident plane wave polarized in y axis (perpendicular polarization) are shown in Fig. 2.7. It is obvious in this figure, better agreement is achieved than that polarized in x axis (parallel polarization). Similar phenomenon has been observed for scattering by infinite long cylinders [128, 118].

Then we examine the effect of particle size on the precision of ray model by comparing the scattering diagrams calculated by VCRM to those obtained by LMT and MLFMA for a particle smaller than in Figs. 2.6 and 2.7. We show in Fig. 2.8 the scattered intensities of a sphere with radius of 30 μm illuminated by the perpendicularly polarized plane wave. We can see from this figure that, the general

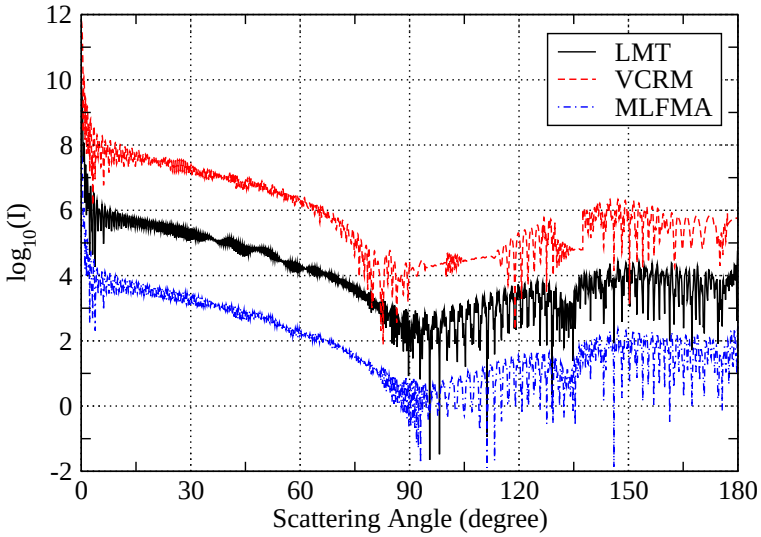

Figure 2.6: Comparison of scattering diagrams computed by LMT, VCRM and MLFMA for a sphere with radius of 50 μm illuminated by the plane wave of wavelength 0.785 μm. The refractive index is 1.33. the incident plane wave propagates along z axis polarized in x axis. The observation is in xz plane. The results of VCRM and MLFMA are shifted by 10^2 and 10^{-2} respectively for clarity.

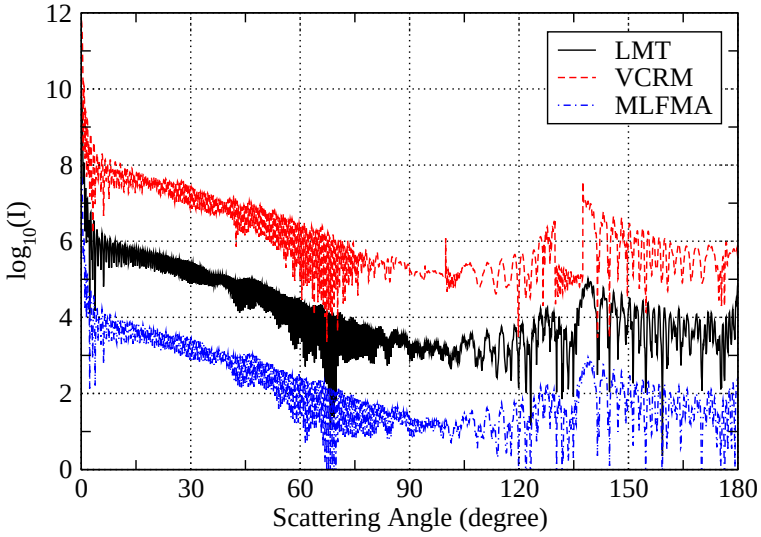

Figure 2.7: Comparison of scattering diagrams computed by LMT, VCRM and MLFMA for a sphere with radius of 50 μm illuminated by the plane wave of wavelength 0.785 μm. The refractive index is 1.33. the incident plane wave propagates along z axis polarized in y axis. The observation is in xz plane. The results of VCRM and MLFMA are shifted by 10^2 and 10^{-2} respectively for clarity.

agreement between LMT and VCRM is still very good but not as good as for the particle with radius of 50 μm. The discrepancy near rainbow angles and around 90° is clearly visible. The MLFMA, of course, still in very good agreement with the LMT results.

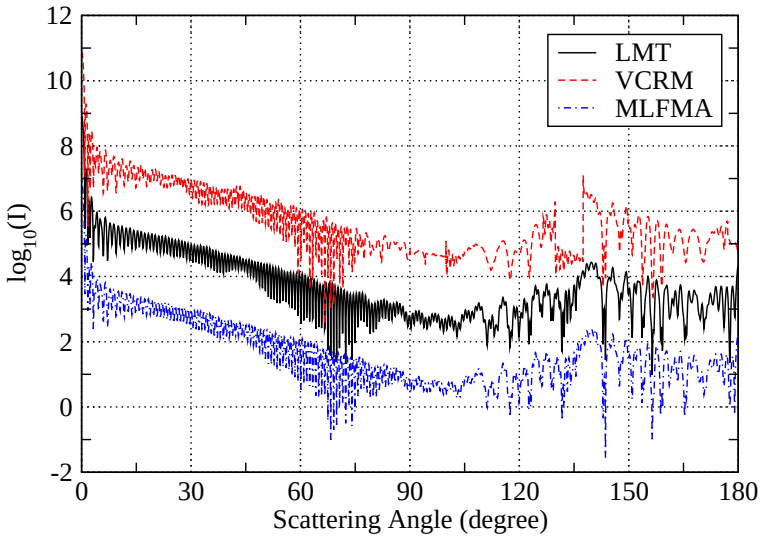

Figure 2.8: Same parameters as in Fig. 2.7 but the particle radius is 30 μm.

If we further reduce radius of the spherical particle to 10 μm, the difference between VCRM and LMT becomes more important, especially for the scattering angle larger than 60° where the profiles of the two curves are still similar but the details are different. The difference in the backward direction becomes also perceivable. But the overall accuracy of VCRM is acceptable even in such condition.

Now we study the influence of aspect ratios for prolate and oblate spheroids separately. We suppose that all the spheroidal particles have the same volume equal to that of a sphere with radius of 30μm. We first set the aspect ratios of a prolate spheroid to $k_1 = 1.0$, $k_2 = 1.1$. In such condition, we have $a = b$ =29.06188 μm, c =31.96807 μm. We have no LMT results for such large spheroid, so we just compute the scattering diagrams of VCRM with MLFMA. The computed results for parallel and perpendicular polarization as a function of scattering angles are plotted in Fig. 2.10 and Fig. 2.11 respectively. Again we can observed that better agreement is achieved for perpendicular polarization than that for parallel polarization. Compared with the spherical case, there are greater discrepancies between these two curves in the Alexander's dark region and near the caustics. The band of the Alexander's dark region between primary and secondary rainbows is also wider than for the sphere. We

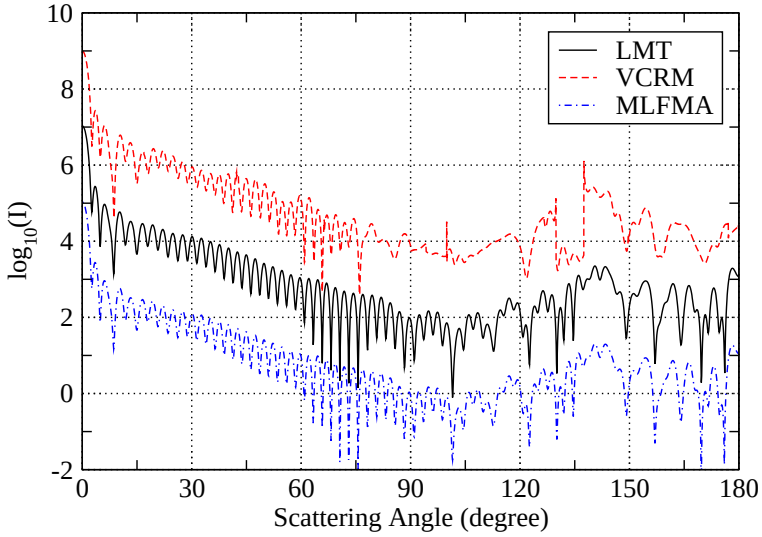

Figure 2.9: Same parameters as in Fig. 2.7 but the particle radius is 10 μm.

can also observe slight differences between the results of VCRM and MLFMA in the strong oscillation region caused by the interference of the diffracted and the reflected waves near the forward direction.

To quantify the discrepancy between the two methods, we can use the global root mean square (RMS) error defined as:

$$\mathrm{RMS} = \sqrt{\frac{1}{N_o}\sum_{i=1}^{N_o} e^2\left(\theta_i\right)}, \qquad \text{with} \qquad e\left(\theta\right) = \frac{\left|I_{cal}\left(\theta\right) - I_{ref}\left(\theta\right)\right|}{\max\left|I_{ref}\left(\theta\right)\right|} \tag{2.41}$$

with N_o the number of scattering angles. I_{cal} and I_{ref} are respectively the intensity calculated by the VCRM and the intensity of reference (here the results of MLFMA). the RMS in Figs. 2.11 and 2.10 are respectively 0.24% and 0.2%, so can conclude the global agreement between VCRM and MLFMA is very good.

However, the global RMS is not suitable to evaluate the difference of the two methods in the range of scattering angles where they have visible discrepancy since the mean scattering intensity will be four to six orders smaller than that in the forward direction. For example, it is clear that discrepancy around 80° in Fig. 2.10 is more important than that in Fig. 2.11. Here we define an average mean relative error to give quantitatively evaluation of the precision of VCRM as:

$$\bar{e}\left(\theta\right) = \frac{\left|\bar{I}_{cal}\left(\theta\right) - \bar{I}_{ref}\left(\theta\right)\right|}{\max\left|\bar{I}_{ref}\left(\theta\right)\right|}, \quad \theta = 0^\circ, 1^\circ, 2^\circ \cdots \tag{2.42}$$

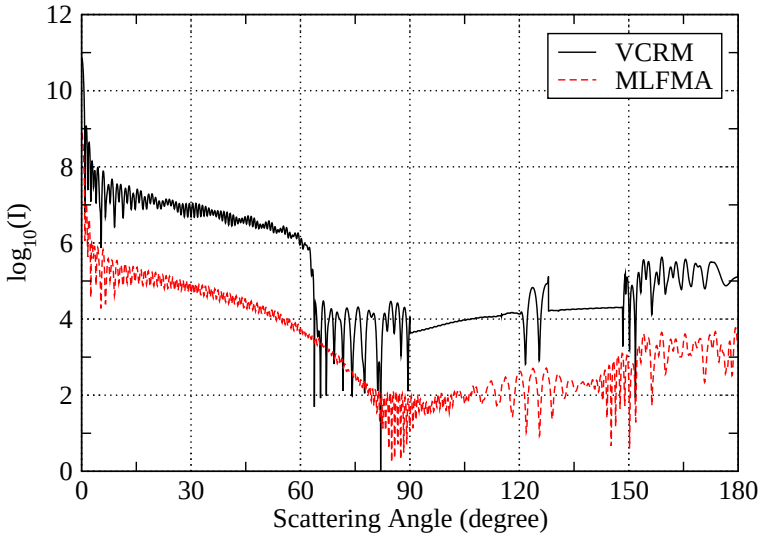

Figure 2.10: Comparison of scattering diagrams computed by VCRM and MLFMA for a prolate spheroid ($k_1 = 1$, $k_2 = 1.1$ and $m = 1.33$) with volume equal to that of a sphere with radius of 30 μm. The plane wave of wavelength 0.785 μm propagates along z axis polarized in x axis. The observe plane is fixed in xz plane. The results of VCRM are shifted by 10^2 for clarity.

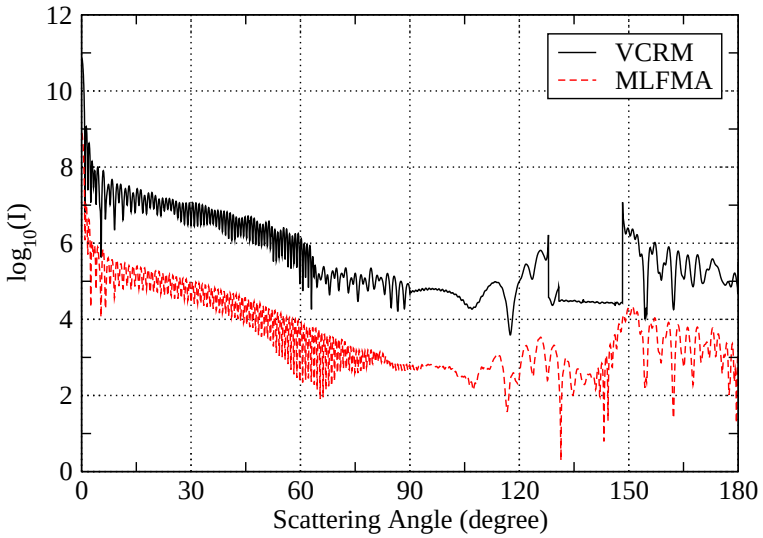

Figure 2.11: Comparison of scattering diagrams computed by VCRM and MLFMA for a prolate spheroid ($k_1 = 1$, $k_2 = 1.1$ and $m = 1.33$) with volume equal to that of a sphere with radius of 30 μm. The plane wave of wavelength 0.785 μm propagates along z axis polarized in y axis. The observe plane is fixed in xz plane. The results of VCRM are shifted by 10^2 for clarity.

where $\bar{I}_{cal}$ and $\bar{I}_{ref}$ are the average value of the scattering intensities in dB calculated for each degree by VCRM and MLFMA respectively. This choice is to avoid the high oscillations in the scattering diagrams. They are calculated by:

$$\bar{I}(\theta) = \frac{1}{11}\sum_{i=1}^{11} \log_{10}\left[I\left(\theta + (i-1)\times 0.1^{\circ}\right)\right] \tag{2.43}$$

The calculated relative error as a function of scattering angles for Fig. 2.10 and Fig. 2.11 are plotted in Fig. 2.12. We find that VCRM and MLFMA are in better agreement for the perpendicular polarization than the parallel polarization around 80°.

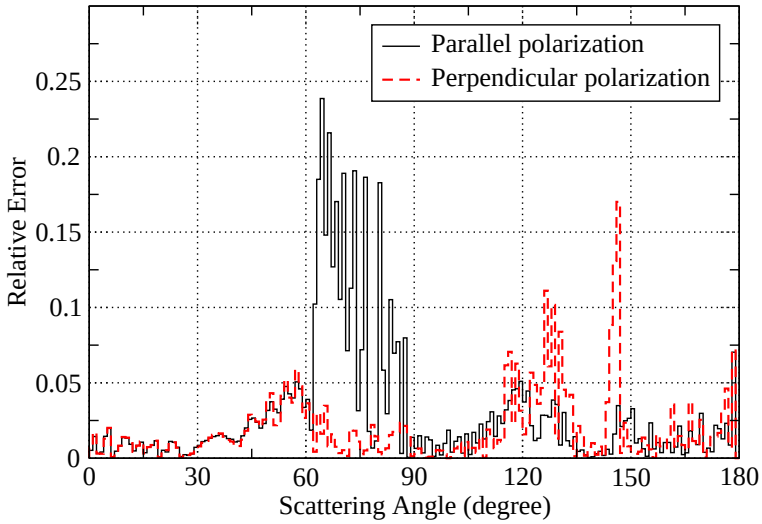

Figure 2.12: Relative error between VCRM and MLFMA in Fig. 2.10 and Fig. 2.11.

We further change the aspect ratios to $k_1 = 1.0$, $k_2 = 1.2$ ($a = b$ =28.23108 μm, c =33.87730 μm) and the scattering diagrams are shown in Fig. 2.13. We can observe similar phenomenon as in Fig. 2.11, the band of the Alexander's dark region becomes even wider, slight differences between results from VCRM and MLFMA in the strong oscillation region near the forward direction.

Then in Fig. 2.14 we show the scattering diagrams to the same particle but with the incident wave is inclined to 30°. The scattering diagrams are no longer symmetric as they should be, so they are given in all directions (−180° to 180°). There are two Alexander dark regions in the two sides of the scattering diagram (0° to 180° and −180° to 0°) not symmetric, as shown in Fig. 2.15: one very narrow ranges from −97.5° to −93.9° not very visible; the other ranges from 161.8° to 186.2° (−173.8°) which is clearly visible. Also, the two curves by VCRM and MLFMA are again in

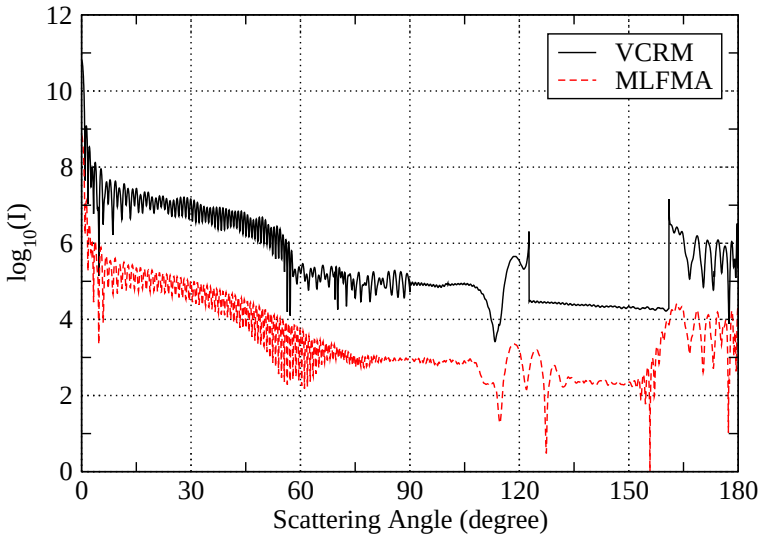

Figure 2.13: Same parameters as in Fig. 2.11 except the aspect ratio is set to $k_1 = 1.0$, $k_2 = 1.2$.

very good agreement except these in Alexander dark regions and near $-150°$. These effects can be clearly seen from the ray tracing graph given in Fig. 2.16. The rainbow of the first order (blue) around $-100°$ is much important that in $-170°$. The peaks around 140°-150° are due to the rays corresponding to the rainbow of second order $p = 3$. But the structures are very different from that of a sphere.

If we further increase the incident angle to 60°, as shown in Fig. 2.17. There is only one Alexander dark region in one side of the scattering diagram ($-180°$ to $0°$). It ranges from $-178.3°$ to $-160.6°$ and is clearly visible. The other dark Alexander region disappears because both the rays of order $p = 2$ and $p = 3$ cover the region from $-77.4°$ to $-55.9°$, as shown in Fig. 2.18. Again we can see that the two curves of VCRM and MLFMA are in very good agreement except those in Alexander dark regions and in the region around $-60°$ where both the rays of $p = 2$ and $p = 3$ exist. When the incident angle is set to 90° (Fig. 2.19), the results of VCRM and MLFMA are in better agreement than in Fig. 2.17. This is because there is no dark Alexander region in such condition.

If we change aspect ratio to $k_1 = 1.0$, $k_2 = 1.5$ ($a = b$ =26.20741 μm, c =39.31112 μm), the Alexander's dark region is not visible. Ray tracing in Fig. 2.20 shows that, unlike these for sphere or prolate spheroids with small aspect ratios, when the aspect ratio is set to $k_2 = 1.5$, rays of order $p = 2$ and $p = 3$, which can form the primary and secondary rainbows will be almost all in the backward and forward direction

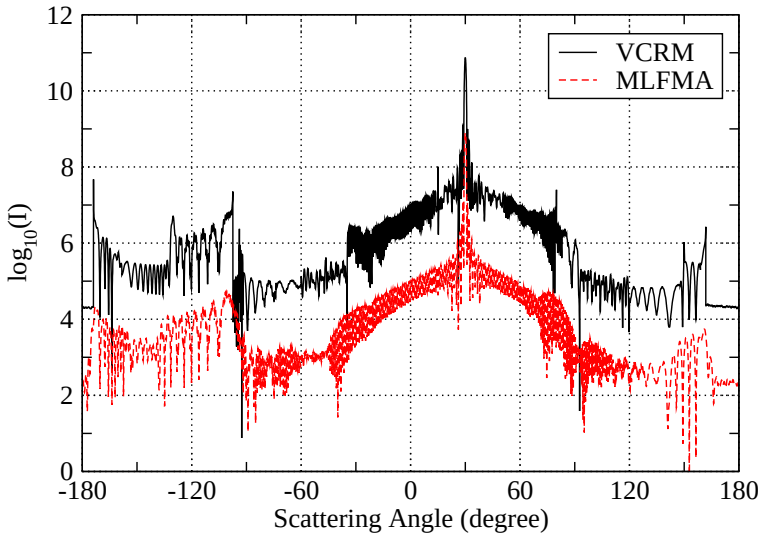

Figure 2.14: Comparison of scattering diagrams computed by VCRM and MLFMA for a prolate spheroid ($k_1 = 1$, $k_2 = 1.2$ and $m = 1.33$) with the incident angle set to 30°. Other parameters are the same as in Fig. 2.13.

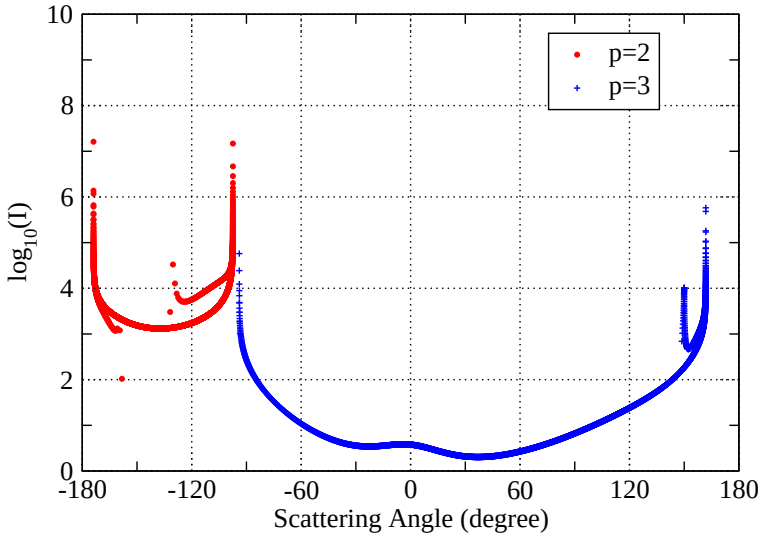

Figure 2.15: Scattered intensities of rays order $p = 2$ and $p = 3$ for the prolate spheroid in Fig. 2.14.

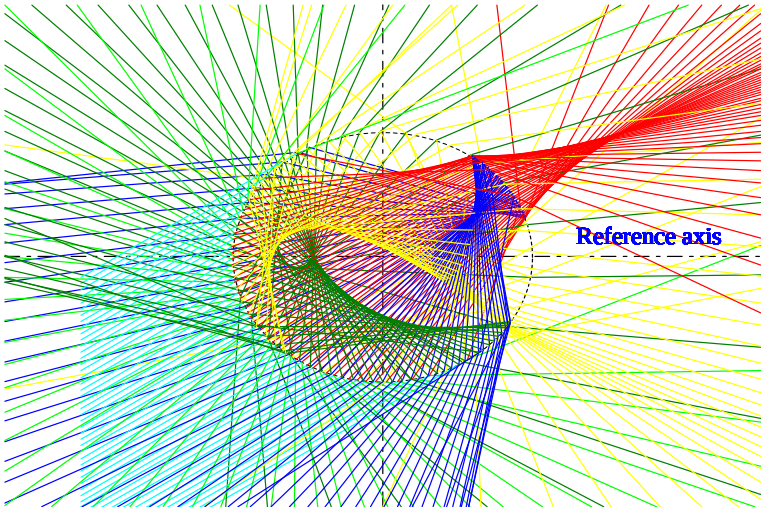

Figure 2.16: Ray tracing for the prolate spheroid in Fig. 2.14. Incident rays: cyan, $p = 0$: red, $p = 2$: blue, $p = 3$: green, $p = 4$: yellow.

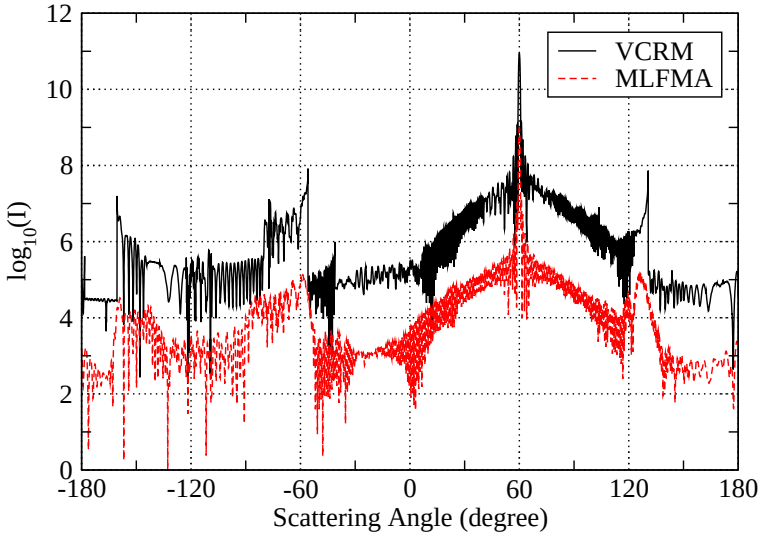

Figure 2.17: Comparison of scattering diagrams computed by VCRM and MLFMA for a prolate spheroid ($k_1 = 1$, $k_2 = 1.2$ and $m = 1.33$) with the incident angle set to 60°. Other parameters are the same as in Fig. 2.13.

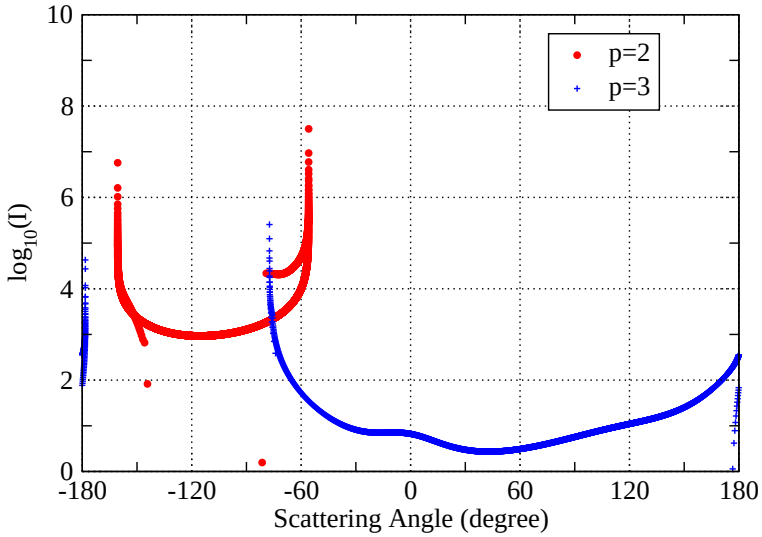

Figure 2.18: Scattered intensities of rays order $p = 2$ and $p = 3$ for the prolate spheroid in Fig. 2.17.

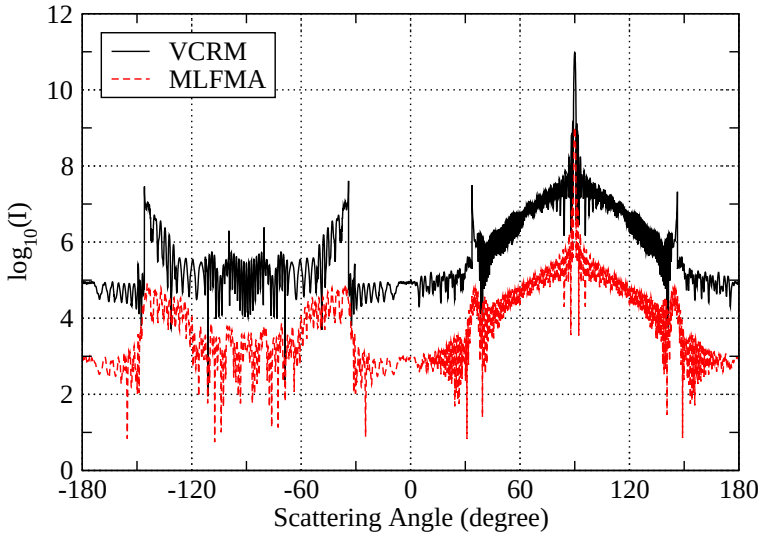

Figure 2.19: Comparison of scattering diagrams computed by VCRM and MLFMA for a prolate spheroid ($k_1 = 1.0$, $k_2 = 1.2$ and $m = 1.33$) with the incident angle set to 90°. Other parameters are the same as in Fig. 2.13.

respectively. Then the agreement between these two results are very good for the observation angles range 90° to 180° .

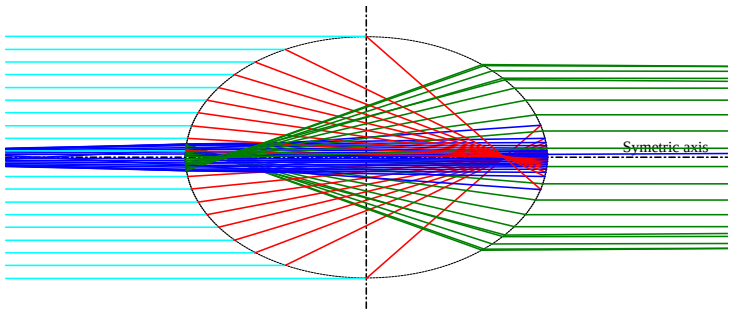

Figure 2.20: Ray tracing for rays of order $p = 2$ and $p = 3$ for a prolate spheroid with equivalent radius 30 μm with aspect ratio $k_1 = 1.0$, $k_2 = 1.5$.

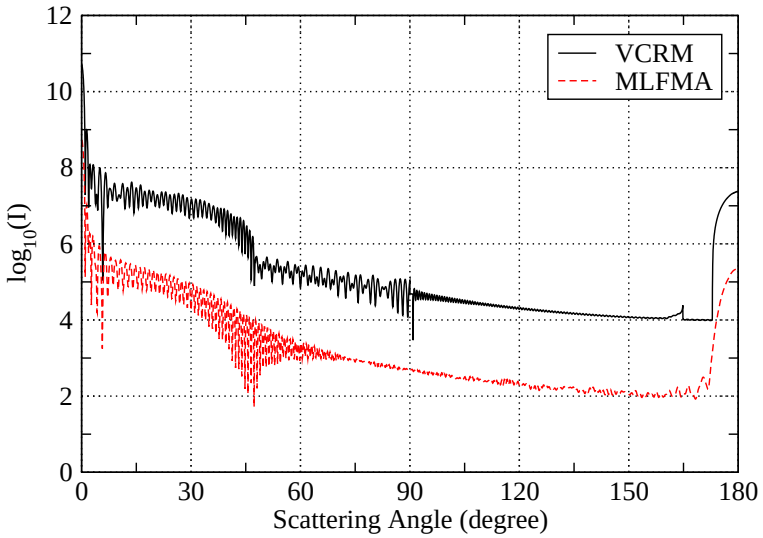

Figure 2.21: Same parameters as in Fig. 2.11 except the aspect ratio is set to $k_1 = 1.0$, $k_2 = 1.5$.

Now we examine the scattering diagram of oblate spheroids calculated by the two methods. We set $k_1 = 0.9$, $k_2 = 1.0$ always for a particle of volume equivalent to a sphere of radius 30 μm such that the three axes are $a = c$ =31.07232 μm, b =27.96509 μm. The scattering diagrams calculated by VCRM and MLFMA are shown in Fig. 2.22. Compared with that for a sphere in Fig. 2.8, the discrepancy between the two methods for observation angles from 70° to about 120° is more visible. There is also a peak for the curve of VCRM at about 42° which differs greatly from the curve of MLFMA. Around this angles are the rainbow of third and fourth orders ($p = 4$ and $p = 5$) where the intensity tends to be very large and a singularity appears in VCRM.

For the case $k_1 = 1.0$, $k_2 = 0.9$, equivalent to set the observation plane in yz plane in the case above. As shown in Fig. 2.23, the agreements between the two methods is better than that in Fig. 2.22.

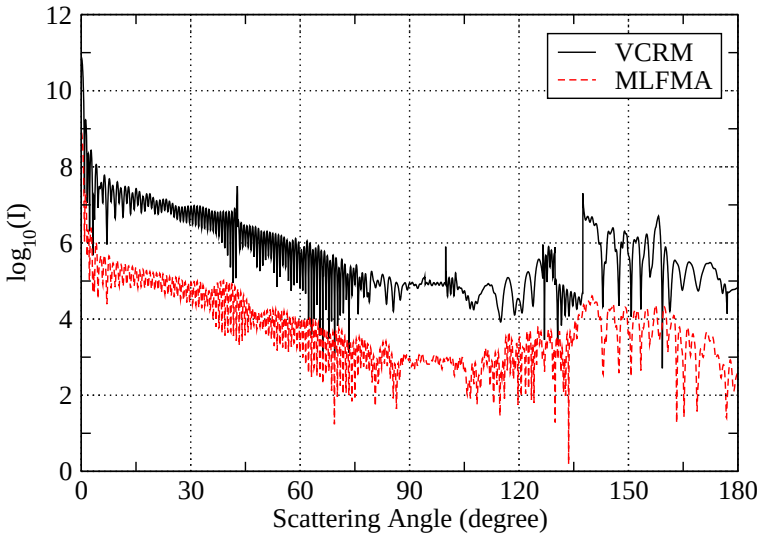

Figure 2.22: Comparison of scattering diagrams computed by VCRM and MLFMA for an oblate spheroid ($k_1 = 0.9$, $k_2 = 1.0$). Other parameters are the same as in Fig. 2.11.

Our VCRM code can also calculate the scattering diagrams of large ellipsoids when the incident plane wave remains in a plane defined by any two axis of the ellipsoid. Fig. 2.24 and Fig. 2.25 show respectively the scattering diagrams of an ellipsoid with $k_1 = 1.1$, $k_2 = 1.2$ (a =27.34827 μm, b =30.08310 μm, c =32.81793 μm) and $k_1 = 1.2$, $k_2 = 1.1$ (a =27.34827 μm, b =32.81793 μm, c =30.08310 μm). The incident plane wave is perpendicularly polarized. Similarly, good agreement can be observed.

To study the influence of size parameter, we show in the next example the scattering diagram of a prolate spheroid with its volume equal to a sphere of radius 50μm ($x = 400$). The aspect ratios are $k_1 = 1.0$, $k_2 = 1.2$, which correspond to $a = b = 47.05180$ μm, $c = 56.46216$ μm. The scattering diagrams computed by VCRM and MLFMA are shown in Fig. 2.26. Compared to the results in Fig. 2.13 for the smaller prolate spheroid of 30 μm, better agreements are observed in the scattering angles near 120°, as the mean relative error given in the Fig. 2.27. This is because the bigger the scatter is, the better the result of the ray model. The Alexander's dark region is still clearly visible.

Then we show in Fig. 2.28 the scattering diagram of an ellipsoid. The two aspect ratios are $k_1 = 1.1$, $k_2 = 1.2$ (a =45.58046 μm, b =50.13850 μm, c =54.69655 μm).

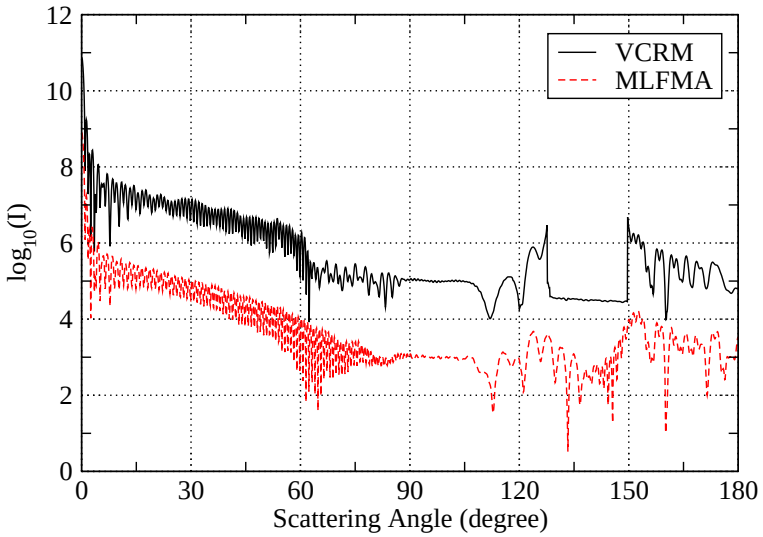

Figure 2.23: Comparison of scattering diagrams computed by VCRM and MLFMA for an oblate spheroid ($k_1 = 1.0$, $k_2 = 0.9$). Other parameters are the same as in Fig. 2.22.

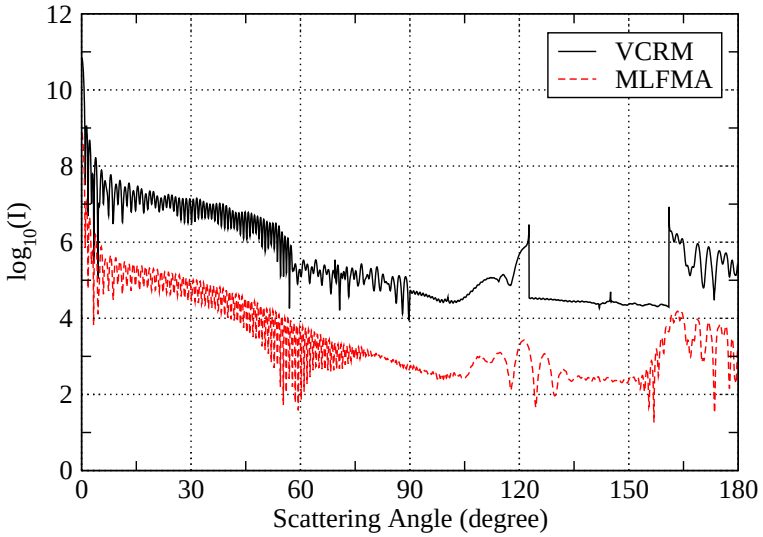

Figure 2.24: Comparison of scattering diagrams computed by VCRM and MLFMA for an ellipsoid ($k_1 = 1.1$, $k_2 = 1.2$) illuminated by a perpendicular polarized plane wave. Other parameters are the same as those in Fig. 2.11.

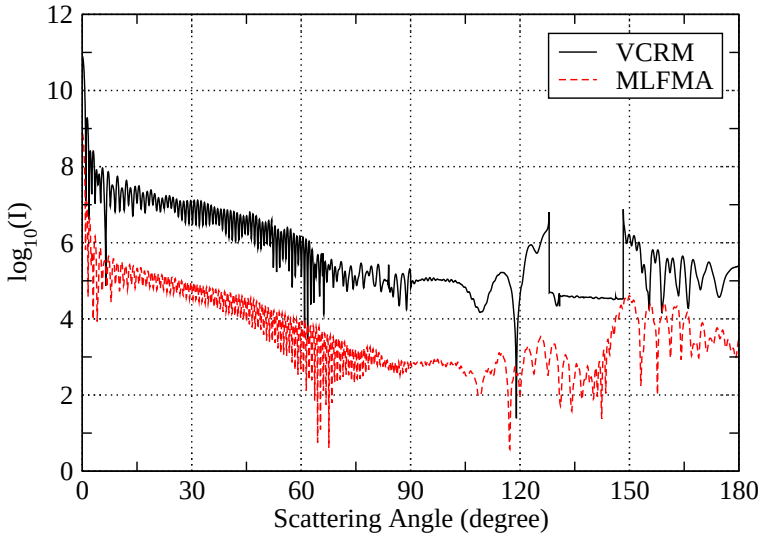

Figure 2.25: Comparison of scattering diagrams computed by VCRM and MLFMA for an ellipsoid ($k_1 = 1.2$, $k_2 = 1.1$). Other parameters are the same as those in Fig. 2.24.

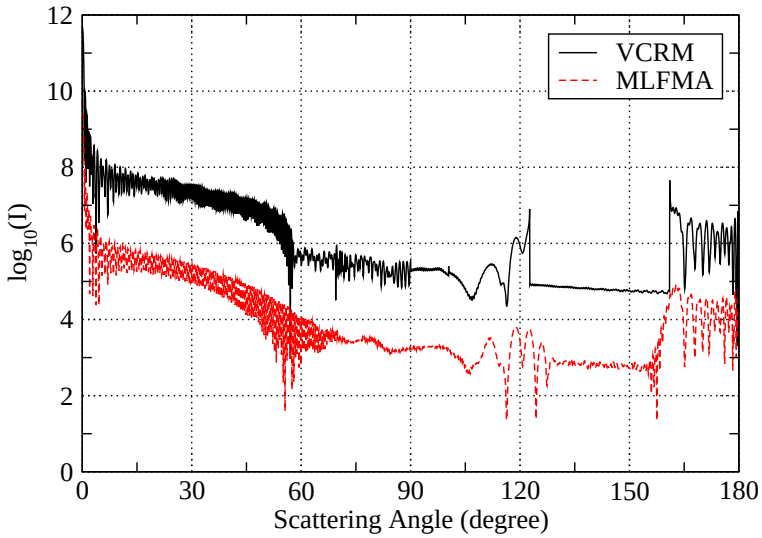

Figure 2.26: Comparison of scattering diagrams computed by VCRM and MLFMA for a prolate spheroid ($k_1 = 1.0$, $k_2 = 1.2$ and $m = 1.33$) with its volume equals to a sphere with radius of 50 μm illuminated by the plane wave of wavelength 0.785 μm. The incident plane wave propagates along z axis polarized in y axis. The observe plane is fixed in xz plane. The results of VCRM are shifted by 10^2 for clarity.

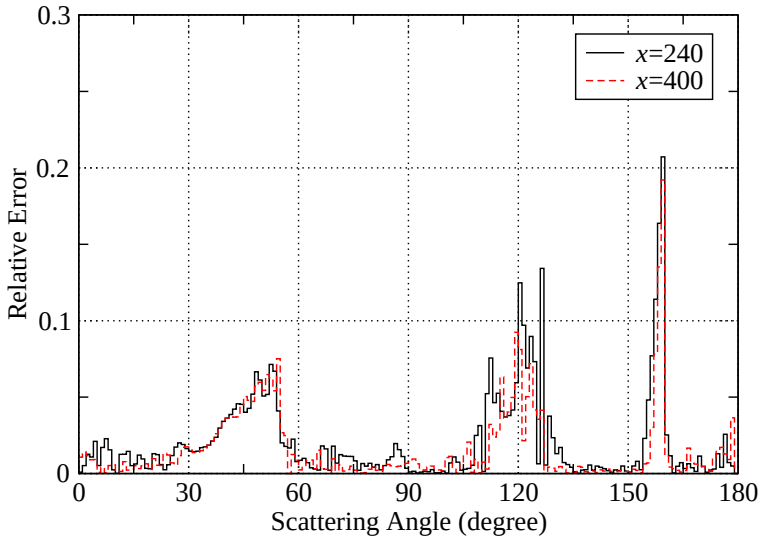

Figure 2.27: Relative error between scattering diagrams for a prolate spheroid ($k_1 = 1.0$, $k_2 = 1.2$) with different size parameters by VCRM and MLFMA.

Again better agreements can be observed between VCRM and MLFMA compared to the results in Fig. 2.24, especially for scattering angles range from 90° to 120°.

In the last example, we show in Fig. 2.29 the scattering diagram of an ellipsoid ($k_1 = 1.1$, $k_2 = 1.2$, a =45.58046 μm, b =50.13850 μm, c =54.69655 μm) with an incident angle of 30°. Still good agreements can be observed between the two methods. From all the numerical experiments shown in Fig. 2.6-2.29 we can conclude that VCRM can predict with precision the scattering diagrams of a sphere, prolate or oblate spheroids, ellipsoids of size as small as some tens of wavelengths. The larger the size of the particle, the better the precision. However, in ray model, there are singularities near rainbow angles for particles of refractive index greater than that of the surrounding medium and near critical angles where the derivative of intensity is not continuous. These problems are under study by taking into account wave effect.

For a non-spherical particle such as the ellipsoid, we can observe another kind of singularity: transverse convergence [117]. For example, when a plane wave is incident on a an ellipsoidal particle in xz plane and the particle has a circular section in this (xz) plane. By changing the semi-axis in x direction, we can obtain a transverse convergence of the wave in the direction perpendicular to xz plane. A numerical result is shown in Fig. 2.30 for the aspect ratios $k_1 = 0.5$, $k_2 = 1$ ($a = c$ =62.99605 μm, b =31.498031 μm). We found a peak near 8°. This phenomenon is due to the transversal convergence of the wave in the direction perpendicular to the scattering

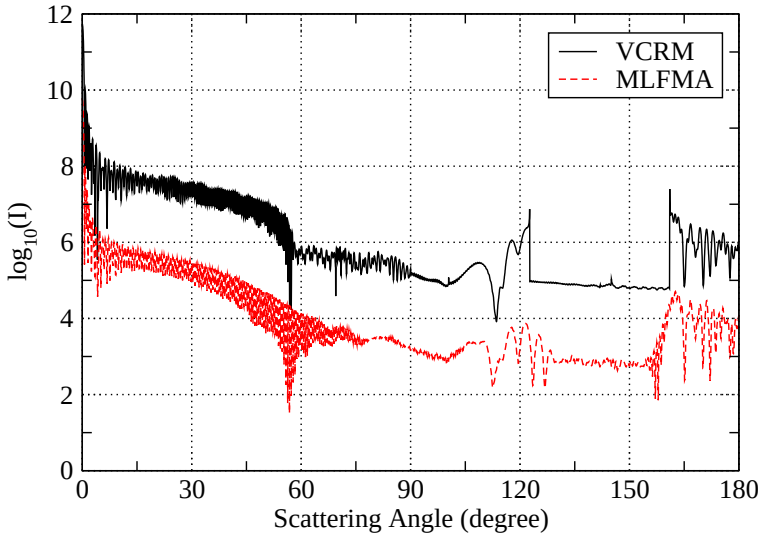

Figure 2.28: Comparison of scattering diagrams computed by VCRM and MLFMA for an ellipsoid ($k_1 = 1.1$, $k_2 = 1.2$ and $m = 1.33$) with its volume equals to a sphere with radius of 50 μm illuminated by the plane wave of wavelength 0.785 μm. The incident plane wave propagates along z axis polarized in y axis. The observe plane is fixed in xz plane. The results of VCRM are shifted by 10^2 for clarity.

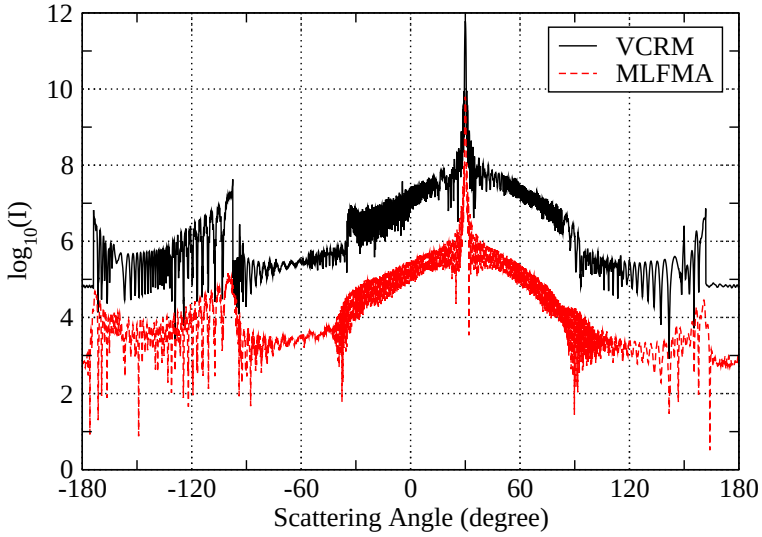

Figure 2.29: Comparison of scattering diagrams computed by VCRM and MLFMA for an ellipsoid ($k_1 = 1.1$, $k_2 = 1.2$ and $m = 1.33$) with its volume equals to a sphere with radius of 50 μm illuminated by the plane wave of wavelength 0.785 μm. The incident plane wave with the incident angle 30° propagates along z axis polarized in y axis. The observe plane is fixed in xz plane. The results of VCRM are shifted by 10^2 for clarity.

Table 2.2: List of computation resources for the large ellipsoid particles: N_u-Number of unknowns, N_i-Number of iterations.

Figures	N_u	Memory (GB)	N_i	CPU (hour)
Fig. 2.26	34.5×10^6	200.5	75	13.8
Fig. 2.29	34.5×10^6	200.8	103	18.9

plane [117]. Scattering intensity in the forward direction is determined by rays of order $p = 0$ and the two peaks are determined by rays of order $p = 1$. But MLFMA does not predict any peak in this region.

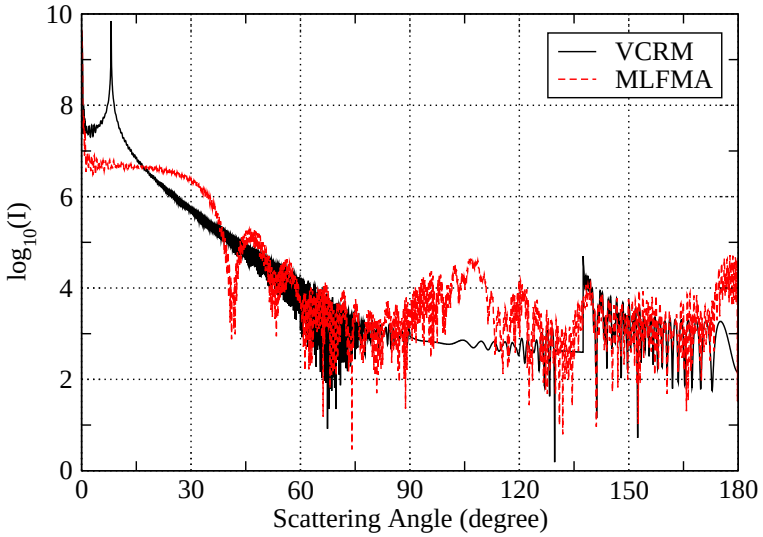

Figure 2.30: Comparison of scattering diagrams computed by VCRM and MLFMA for a oblate spheroid ($k_1 = 0.5$, $k_2 = 1$) with the same volume of a sphere with radius 50 μm. Other parameters are the same as those in Fig. 2.7.

Another important advantages of VCRM is its rapidity. For all the calculations presented in the papers, the computation time is less than one seconde on a personal computer. MLFMA is however needs much more computer resources and CPU times. For the calculation in Fig. 2.29, there are 34.5×10^6 unknowns and The calculation has taken 200.8 GB memory and 18.9 hours CPU time with 36 MPI processes and 2 threads for each process. For smaller particle the CPU time and the number of iterations are both reduced. To give a idea about the the computation resource need, we compile in Table 2.2 the parameters used in the calculations for a large prolate spheroid and an large ellipsoid. These two calculations are performed with 25 MPI processes and 2 threads for each process.

2.3.2 Scattering matrix elements for arbitrary shaped particles with MLFMA

In this last subsection, we aim on the light scattering diagrams of two kinds of large non-spherical particles: ellipsoidal and Chebychev particles. We pay our attention to the scattering matrix for particles with different sizes and shapes. The scattering matrix contains all polarizing properties of the particles and plays an important role in radiative transfer studies. Detailed definitions of the scattering elements are given in [129].

First, we apply MLFMA to large ellipsoid particles for the study of the influence of the size parameter on the scattering elements. We fix aspect ratios to ($k_1 = 1.4, k_2 = 2.0$) for three ellipsoids with different size parameters (x = 126, 220 and 314). Fig. 2.31 (a) illustrates the comparison of the scattering-matrix element $S_{11}(\theta)$ of ellipsoid particles with different size parameters. We fix $\alpha = 0°$, $\beta = 0°$, $\gamma = 0°$, and observe plane in yz plane. It is evident and logical that the value of $S_{11}(\theta)$ increases with the size parameter. S_{11} has a strong oscillation behavior in the forward direction but much smoother in the backward direction. This is not observed for a small particle (Fig. 2.5) and can be explained by the effect of absorption. In the view point of GO, the high order rays are absorbed by particle and the strong oscillations in the forward direction may be understood as the interference of the diffracted and the reflected waves. With the increment of the particle size, the curve of $S_{11}(\theta)$ becomes smoother. We also plot the scattering element $-S_{12}/S_{11}$ for ellipsoids with different size parameters in Fig. 2.31 (b) and the similar phenomena caused by the effect of absorption is observed.

Then we examine the scattering properties as function of the particle shape, or in other words, influence of the aspect ratio for ellipsoids. Consider three ellipsoids of equal volume with the same size parameter $x = 220$ and the same aspect ratio $k_2 = 2.0$, but different aspect ratio k_1: 1.4, 2.3 and 3.5. The results are shown in Fig. 2.32, noticeable differences can be observed for these three curves. With the increment of k_1 (i.e. the semi-axis in y direction b), $S_{11}(\theta)$ between about 50° to 120° decreases while that for the angle larger than 100° increases. We observe also a significant variation of the amplitude in forward direction. These are due to the shape of the particle. The scattering element $-S_{12}/S_{11}$ for ellipsoids with different aspect ratios are shown in Fig. 2.32 (b). It is noted that $-S_{12}/S_{11}$ is more sensible to the aspect ratio in the forward direction than in the backward direction. We can

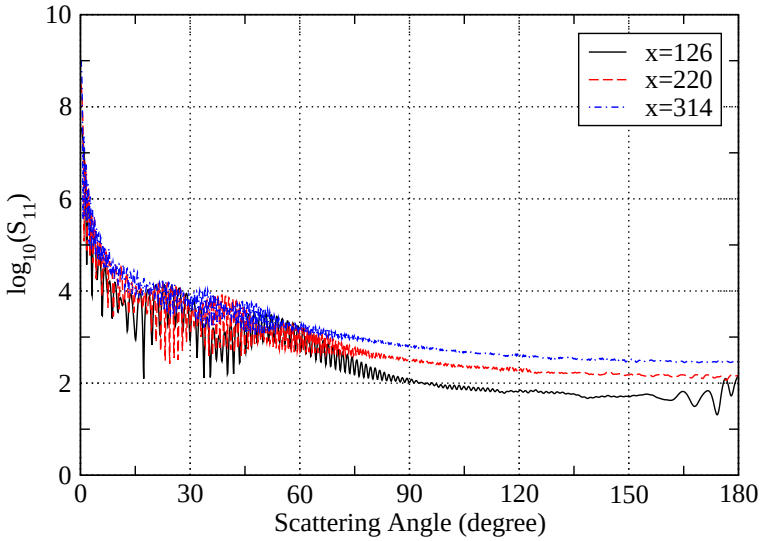

(a)

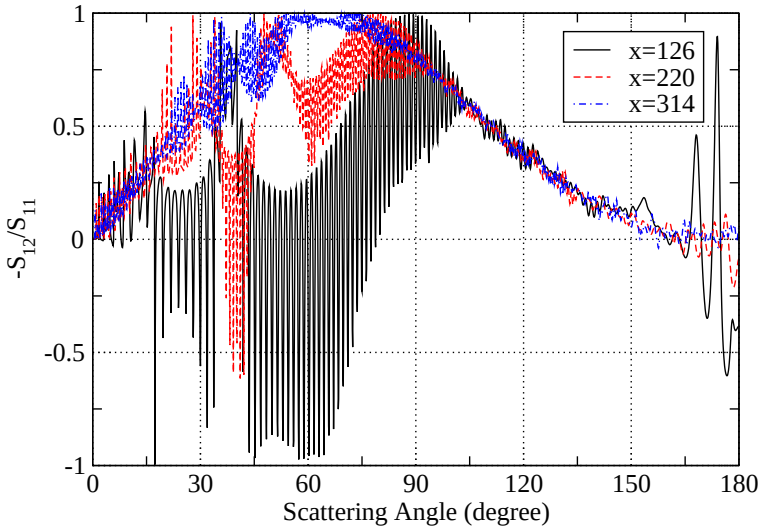

(b)

Figure 2.31: Comparison of S_{11} and $-S_{12}/S_{11}$ for ellipsoids of refractive index $m = 1.555 + 0.004i$ illuminated by a plane wave of wavelength 0.633 μm with different size parameters. We set $\alpha = 0°$, $\beta = 0°$ and $\gamma = 0°$, and observe in yz plane.

conclude from Figs. 2.31 and 2.32 that the scattering-matrix elements are sensitive to the size parameter and the aspect ratio for large ellipsoidal particles.

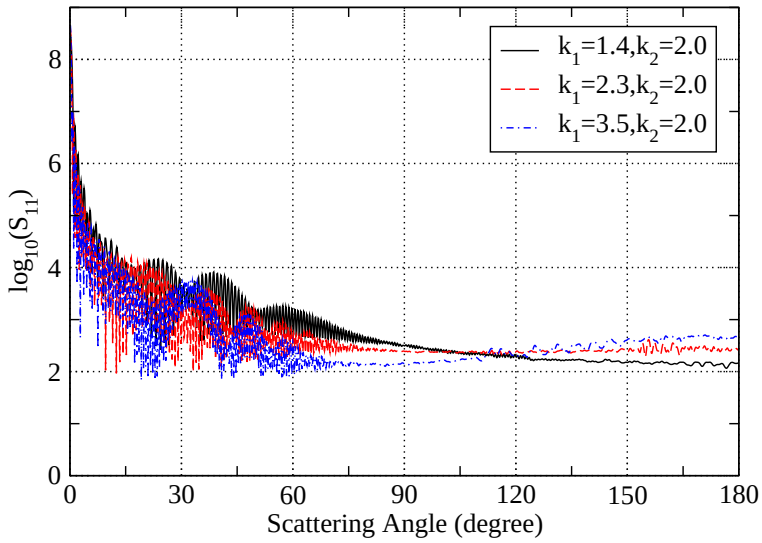

(a)

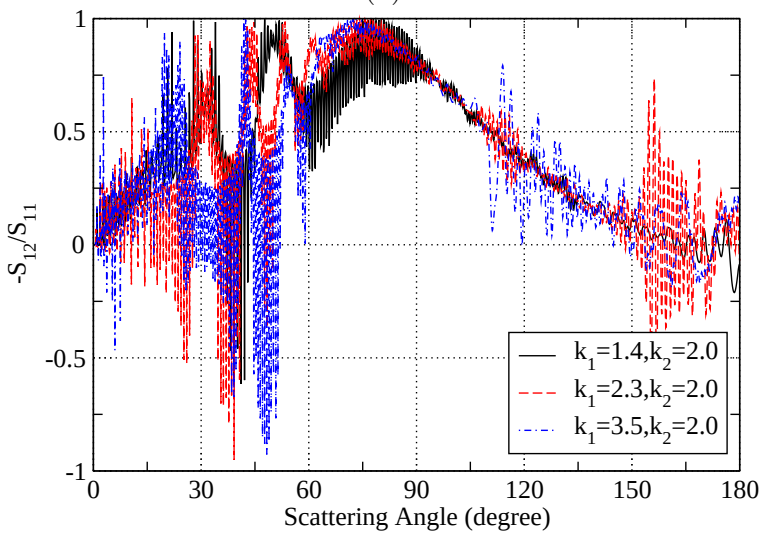

(b)

Figure 2.32: Comparison of S_{11} and $-S_{12}/S_{11}$ for ellipsoids of refractive index $m = 1.555 + 0.004i$ illuminated by a plane wave of wavelength 0.633 μm with different aspect ratios.

The SIE with MLFMA is flexible in term of particle shape and can be easily applied for irregular shaped particles. To show its ability in the study of the scattering properties of large particles with more complex shape, we consider Chebyshev

particles, which shapes are defined by:

$$r = r_0(1 + \sum_{n=0}^{\infty} c_n \cos n\theta) \tag{2.44}$$

where r_0 is the radius of a volume-equivalent sphere, c_n are the deformation coefficients, more information for this model can be found in [130].

The geometry of Chebyshev particles under study is sketched in Fig. 2.33. In our simulation, the deformation coefficients c_n are $c_0 = -9763 \times 10^{-5}$, $c_1 = 0$, $c_2 = -28966 \times 10^{-5}$, $c_3 = -10143 \times 10^{-5}$, $c_4 = -1677 \times 10^{-5}$, $c_5 = 346 \times 10^{-5}$, $c_6 = 173 \times 10^{-5}$, $c_7 = 21 \times 10^{-5}$, $c_8 = -76 \times 10^{-5}$, $c_9 = -29 \times 10^{-5}$. The axis ratio of such particle is $b/a = 0.583$. The size parameter of the Chebyshev particle is taken to be 377. In these conditions, the surface of the particle is discretized into 12×10^6 triangle patches with 35.6×10^6 unknowns.

The scattering matrix elements S_{11} and $-S_{12}/S_{11}$ calculated by MLFMA are shown in Figs. 2.34, 2.35 and 2.36 respectively for the incident angle $\beta = 0°$, $90°$ and $180°$ with $\alpha = 90°$ and $\gamma = 0°$. Such condition corresponds to a rotation of the particle respect to $+x$ axis. When $\beta = 0°$ and $180°$, the scattering diagrams are symmetric about z axis, so the curves are plotted only for θ between $0°$ and $180°$ in Figs. 2.34 and 2.36. But when $\beta = 90°$ the scattering diagrams in all directions must be plotted because of the asymmetry of the problem (Fig. 2.35). We remark that when the particle is illuminated along the symmetric axis, from the bottom or the top, the curves of S_{11} are similar in forward direction (Fig. 2.34 (a) and Fig. 2.36 (a)). But there is a strong oscillation in the backward direction when the particle is illuminated from the bottom ($\beta = 0°$). This can be explained by the interference of the waves reflected from the hollow part of the particle. The profiles of the curves $-S_{12}/S_{11}$ are also similar with a little shift of the peak to a larger angle for the top illumination.

The scattering matrix elements are very different when the Chebyschev particle is illuminated from the side ($\beta = 90°$ Fig. 2.35). Both the curves of S_{11} and $-S_{12}/S_{11}$ are not symmetric about z axis, i.e. they are different in the angle ranges $0°$ - $180°$ and $180°$ - $360°$), as it should be. Also, because of its irregular shape, there is no strong oscillation or significant variation of the amplitude in forward direction.

At last, to demonstrate the capacity of our algorithm, we consider an extremely large Chebyshev dust particle of size parameter equal to 628. The symmetry axis of the particle makes $45°$ with respect of the incident wave, i.e. the three Euler angles

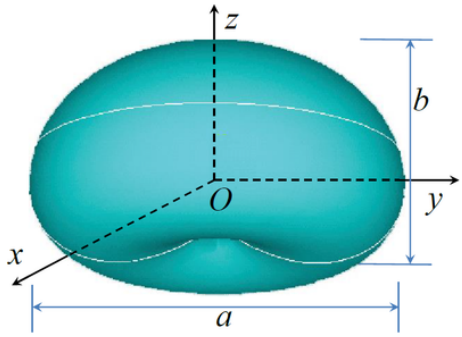

Figure 2.33: Illustration of a Chebyshev shaped dust particle.

are respectively $\alpha = 90°, \beta = 45°, \gamma = 0°$. The step of the scattering angle is now 0.1°, a total of 32.73×10^6 triangular patches are used to model the surface of the particle and this results in 98.19×10^6 unknowns. This calculation took 728 GB memory and 25 hours CPU time with 70 MPI processes and 2 threads for each process. The computed results are shown in Fig. 2.37. We found a peak at 90° with a strong oscillation around. This is due to the reflection of the incident wave from the concave bottom of the particle. For these observe angles range around 270°, where the convex top of the particle faces, the curve of the computed scattering elements is very smooth.

2.4 Conclusions

The classical geometrical optics model is approximated and, in principle, it can be used to predict light scattering of very large and irregular shaped particles. In practice, it is not apt to deal with the scattering of complex shaped particle. In this Chapter, the Vectorial Complex Ray Model (VCRM) is used for computing scattering by large ellipsoids. On the other hand, full wave numerical method SIE is applied to deal with arbitrary shaped particles. However, because it requires large amount of computation resources, the calculable size is severely limited. MLFMA permits to reduce computational complexity of the SIE from $O(N^2)$ to $O(NlogN)$, so the scattering problem of large non-spherical particle can be solved. To further enlarge size parameter of the particle, an efficient Hybrid MPI and OpenMP parallelization is employed. In this chapter, the codes of VCRM and MLFMA are first validated by comparing the scattering diagrams of a spherical particle. Then scattering diagrams calculated by VCRM for large ellipsoidal particles are compared to the results of MLFMA to evaluate the precision of VCRM. Good agreements are observed between

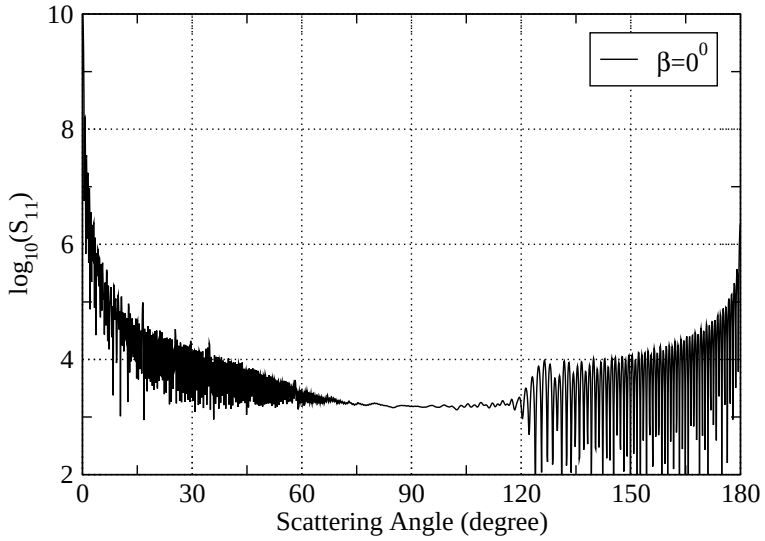

(a)

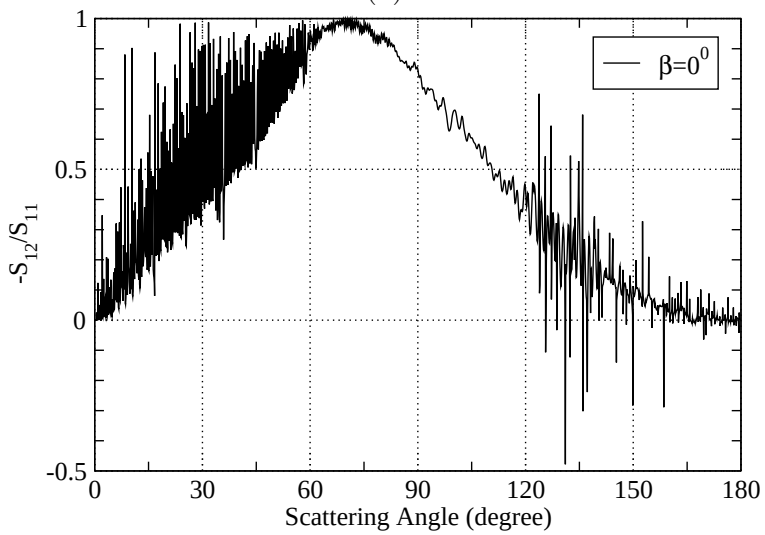

(b)

Figure 2.34: MLFMA results of S_{11} and $-S_{12}/S_{11}$ for a Chebyshev shaped particle $(x = 377, m = 1.555 + 0.004i)$ with Euler angle $(90°, 0°, 0°)$.

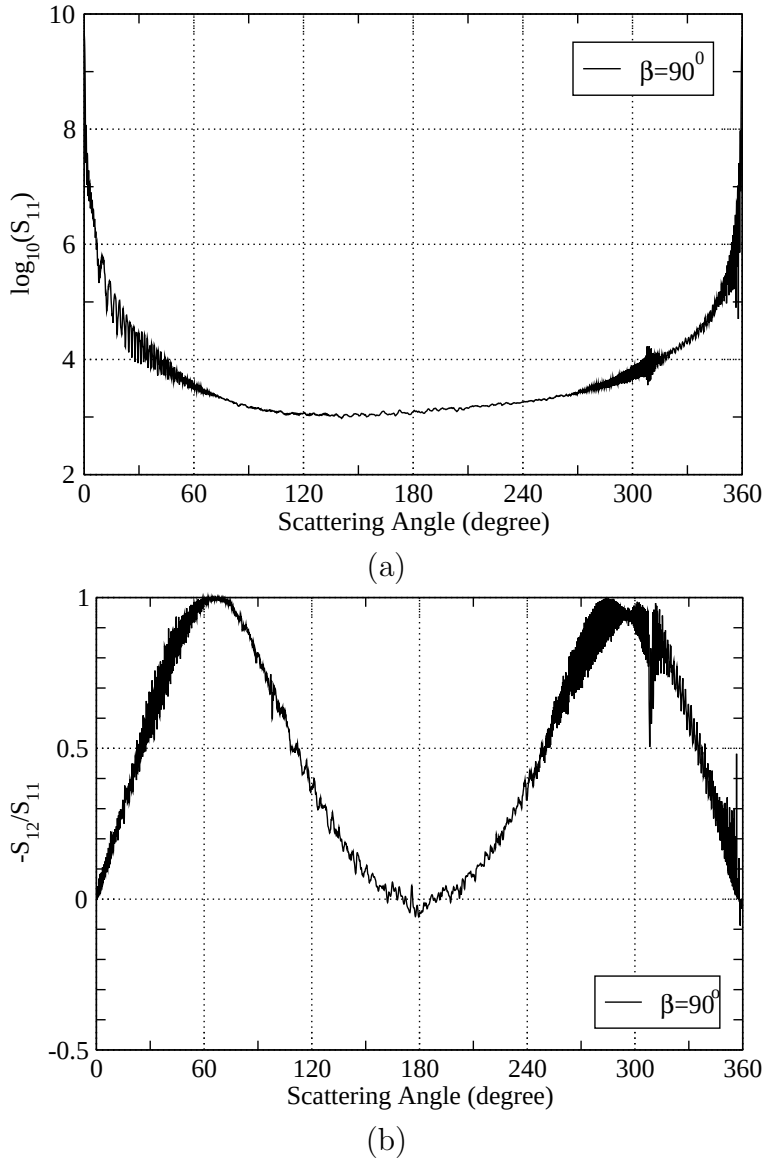

Figure 2.35: MLFMA results of -S_{12}/S_{11} for a Chebyshev shaped particle ($x = 377, m = 1.555 + 0.004i$) with Euler angle $(90°, 90°, 0°)$.

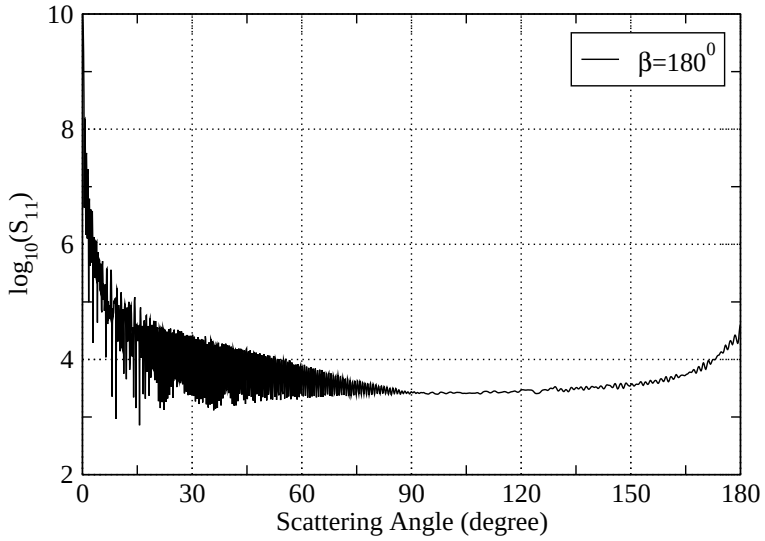

(a)

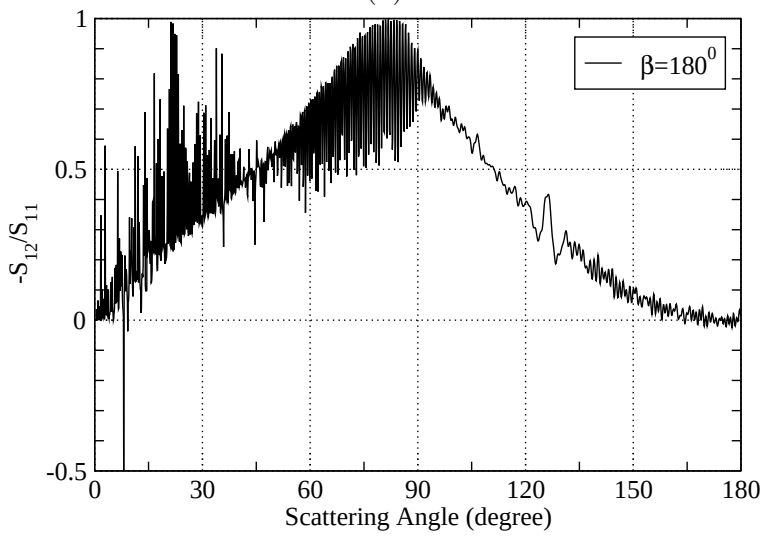

(b)

Figure 2.36: MLFMA results of -S_{12}/S_{11} for a Chebyshev shaped particle ($x = 377, m = 1.555 + 0.004i$) with Euler angle $(90°, 180°, 0°)$.

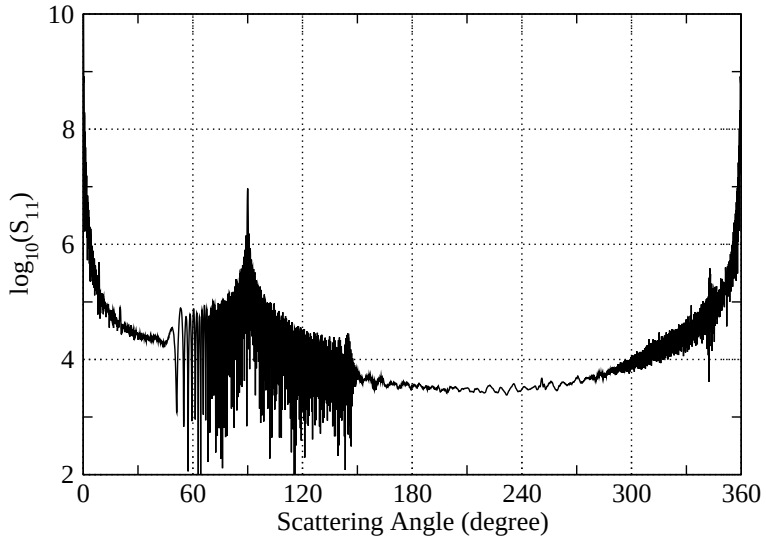

(a)

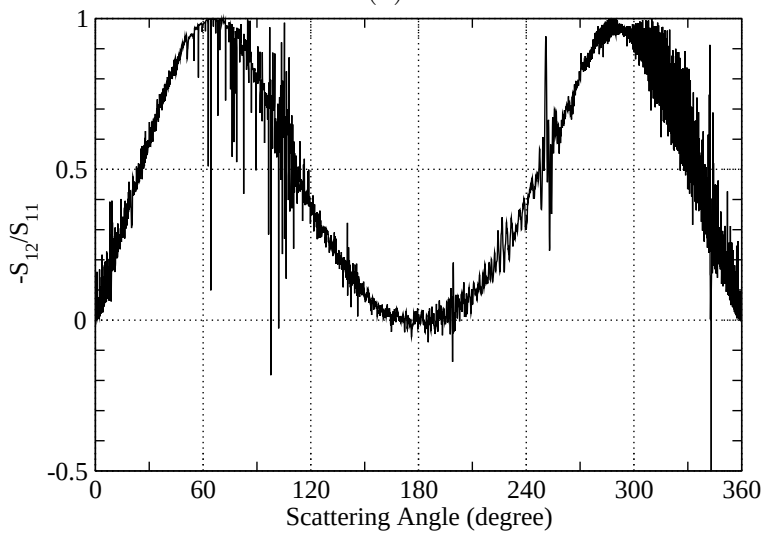

(a)

Figure 2.37: MLFMA results of -S_{12}/S_{11} for a Chebyshev shaped model ($x = 628, m = 1.555 + 0.004i$) with Euler angle $(90°, 45°, 0°)$.

MLFMA and VCRM. Numerical results proved that VCRM can predict with precision the light scattering of a sphere, prolate or oblate spheroids and ellipsoids of size as small as some tens of wavelengths. The code MLFMA developed in this thesis has also been applied to the computation of the scattering matrix of a large ellipsoidal particles and Chebyshev particles of a size parameter as large as 630.

Chapter 3

CTF with MLFMA for optical force and torque

When a particle is illuminated by a beam of light, it experiences a force called radiation pressure force (RPF) and/or torque. Under the action of the RPF generated by tightly focused laser beams, small particles can be trapped and moved to a desired location [60, 61, 131], while the orientation of particles can be controlled through the torque exerted by the beam [132, 78]. The computation of RPF and torque is of growing interest due to its importance in practical applications, such as biological cell trapping [133], design of micromotors [134], and laser based measurement techniques [135].

Theories for RPF and torque computations have already been developed by using different approaches. When the particle is much smaller than the wavelength, the Rayleigh regime is concerned and RPF can be calculated by using the Rayleigh-Debye theory [136]. In order to enlarge object size range, rigorous theory must be developed. To do so, Gouesbet *et al.* developed the GLMT [5] for studies of RPF or torque exerted on a particle of simple shape such as homogeneous sphere [70, 71, 72], multilayered sphere [73], spheroid [12, 75] and a infinite long cylinder of circular cross section [74]. However, the rigorous solutions of Maxwell's equations exist only for a particle whose shape coincides with a specific coordinates system. Furthermore, even for large regular shaped particles such as spheroid or ellipsoid, the numerical computation of the special function is still another obstacle.

Numerical techniques are possible ways to overcome these limitations. Researches on the prediction of the RPF and torque exerted on non-spherical particles by using the DDA [87, 88, 90, 91, 89, 92, 93, 94, 95, 96], the T-matrix method [79, 80, 81, 82, 83, 84]

and the FDTD [97, 98, 99, 100, 101] are reported. The T-matrix method is very efficient and applicable for large particles. But it usually relies on central expansions of the electromagnetic field in VSWF and suitable for rotational symmetry particles. Both DDA and FDTD are volume discretized methods. They are flexible and robust for inhomogeneous, anisotropic particles. But the computational demands for FDTD and DDA increases quickly and calculable size of the particle is severely limited, especially for high refractive index particles. Approximate methods, such as ray optics, can provide approximate results for large particles but is usually not accurate enough [76, 77, 78].

However, trapping and manipulation of large non-spherical particles is much less mastered both in experimental and theoretical researches. In biophysics, microfluidics, microelectronics and photonics, non-spherical particles such as nanotubes and nanorods have their important applications [69, 103, 104]. Morever, experimental researches on non-spherical particles found interesting phenomena greatly different from spherical particles [106, 103, 78, 137]. Compared to the theoretical efforts in the calculation of RPF or torque on spherical particles, less work on the RPF or torque prediction for large non-spherical shape particles has been reported. In this chapter, we present an approach for the computation of the RPF and torque exerted on large arbitrary shape and homogenous particles illuminated by an arbitrary shaped beam. This approach, is based on the MLFMA enhanced SIE method is presented in Chapter 2. Since MLFMA is a surface discritized method with triangles patches, it can be used for arbitrarily shaped large homogenous particles.

For a shaped beam, it is hard or even impossible to get the mathematical description of the electromagnetic field components, which accurately satisfies Maxwell's equations in far-field region [70]. In our computational approach, the RPF/torque is computed by integrating the dot product of the outwardly directed normal unit vector and the Maxwell stress tensor/pseudotensor over a spherical surface tightly enclosing the particle under consideration. In this way, we can use the accurately computed near region electromagnetic fields instead of the widely used far-field approximation [138]. The same mathematical description of the incident beam is used for computing both the equivalent sources in SIE and the Maxwell stress tensor because the enclosed surface of integration can be chosen tightly to the particle surface. Since only the near fields are needed, the calculation of far field components of the incident beams is avoided and it is not necessary to develop the incident beam with the beam shape coefficient as done in GLMT.

In this chapter, we first describe in detail how to compute RPF and torque with MLFMA enhanced SIE. Then, as an example, we calculate the RPF and torque exerted on different kinds of non-spherical particles illuminated by a Gaussian beam. By following the same process, readers can easily use this method to deal with other shaped beams.

3.1 Computation of radiation pressure force and torque

When an arbitrarily shaped particle is illuminated by a shaped beam, the radiation force and the torque exerted on the particle can be determined by integrating the dot product of the surface normal $\hat{\mathbf{n}}$ and the Maxwell stress tensor $\overleftrightarrow{T}$ over a surface enclosing the particle [138, 139]

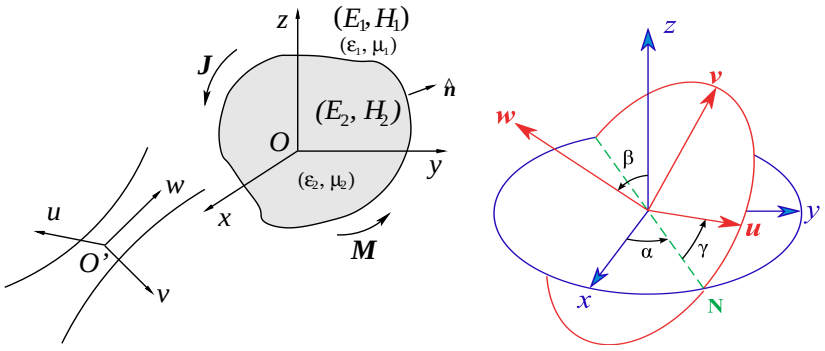

Figure 3.1: Schematic of arbitrary shaped homogeneous particle illuminated by a shaped beam and definition of Euler angles.

$$\mathbf{F} = \int_{S_v} \overleftrightarrow{T}(\mathbf{r}) \cdot \hat{\mathbf{n}} ds \tag{3.1}$$

$$\mathbf{M} = -\int_{s} (\overleftrightarrow{T}(\mathbf{r}) \times \mathbf{r}) \cdot \hat{\mathbf{n}} ds \tag{3.2}$$

where

$$\begin{aligned} \overleftrightarrow{T}(\mathbf{r}) &= \frac{1}{2}\mathrm{Re}[\varepsilon_1 \mathbf{E}(\mathbf{r})\mathbf{E}^*(\mathbf{r}) + \mu_1 \mathbf{H}(\mathbf{r})\mathbf{H}^*(\mathbf{r}) \\ &- \frac{1}{2}(\varepsilon_1 |\mathbf{E}(\mathbf{r})|^2 + \mu_1 |\mathbf{H}(\mathbf{r})|^2)\ \overleftrightarrow{I}] \end{aligned} \tag{3.3}$$

is the time average Maxwell stress tensor, the asterisk * indicates for conjugate, and $\mathbf{E}(\mathbf{r})$ and $\mathbf{H}(\mathbf{r})$ are total electromagnetic fields:

$$\mathbf{E}(\mathbf{r}) = \mathbf{E}^s(\mathbf{r}) + \mathbf{E}^i(\mathbf{r}) \tag{3.4}$$

$$\mathbf{H}(\mathbf{r}) = \mathbf{H}^s(\mathbf{r}) + \mathbf{H}^i(\mathbf{r}) \tag{3.5}$$

If we choose a virtual sphere of radius r_s tightly enclosing the particle with its center located in the scattering object, Eqs. (3.1) and (3.2) can be written as [138]

$$\begin{aligned}
\mathbf{F} &= \frac{1}{4}\int_0^{2\pi}\int_0^{\pi} \mathrm{Re}[\varepsilon_1(|\mathrm{E_r}|^2 - |\mathrm{E}_\theta|^2 - |\mathrm{E}_\phi|^2) \\
&+ \mu_1(|H_r|^2 - |H_\theta|^2 - |H_\phi|^2)\mathbf{e}_r \\
&+ 2(\varepsilon_1 E_r E_\theta^* + \mu_1 H_r H_\theta^*)\mathbf{e}_\theta \\
&+ 2(\varepsilon_1 E_r E_\phi^* + \mu_1 H_r H_\phi^*)\mathbf{e}_\phi] r_s^2 \sin\theta d\theta d\phi \qquad (3.6) \\
\mathbf{M} &= \frac{1}{2}\int_0^{2\pi}\int_0^{\pi} \mathrm{Re}[(\varepsilon_1 E_r E_\theta^* + \mu_1 H_r H_\theta^*)\mathbf{e}_\phi \\
&- (\varepsilon_1 E_r E_\phi^* + \mu_1 H_r H_\phi^*)\mathbf{e}_\theta] r_s^3 \sin\theta d\theta d\phi \qquad (3.7)
\end{aligned}$$

where the electric and magnetic field components are evaluated on the surface of the virtual sphere. To be convenient, the radius r_s is usually chosen to be infinite so that the asymptotic forms can be used for the special functions [138, 75]. For time-harmonic plane wave, such work is straightforward since the wave field expressions rigorously satisfy the Maxwell's equations in all space [140]. But, for a shaped beam, such as Gaussian beam, it is hard or even impossible to get the mathematical description of the electromagnetic fields which satisfy rigorously Maxwell's equations in all space. Hence, to avoid inaccuracy caused by description of the incident electromagnetic fields, the analytical electromagnetic field expression will be used.

Once the equivalent electric and magnetic currents $\mathbf{J}$ and $\mathbf{M}$ are solved, the scattered fields $\mathbf{E}^s$ and $\mathbf{H}^s$ at any point can be obtained by:

$$\mathbf{E}^s = Z_1\mathbf{L_1}(\mathbf{J}) - \mathbf{K_1}(\mathbf{M}) \tag{3.8}$$

$$\mathbf{H}^s = 1/Z_1\mathbf{L_1}(\mathbf{M}) - \mathbf{K_1}(\mathbf{J}) \tag{3.9}$$

Since only the near fields are needed for radiation force and torque, the calculation of the incident electromagnetic fields in far region is avoided. Theoretically, the virtual sphere can be chosen arbitrarily. However, to avoid special treatment for dealing with the singularity of Green's function, we choose a spherical surface tightly close to the outer surface of the particle (minimum 0.1λ away from the particle surface S). The

same analytical expressions of the incident wave are used for computing both the equivalent sources in SIE and the Maxwell stress tensor.

Then, we need to deal with the spherical integral in Eqs. (3.6) and (3.7). Among different kinds of numerical integral methods, the Gaussian surface integral is simple with high accuracy. We choose an integral number N_L to divide the interval $[0, \pi]$, such that $\cos\theta$ satisfies the Gauss Legendre quadrature rule, and $2N_L$ points averagely in $[0, 2\pi]$ for ϕ. Usually, N_L is determined by

$$N_L = k_1 r_s + 3\ln(k_1 r_s + \pi) \tag{3.10}$$

To show the precision and the capability of our method for the computation of RPF and torque, we use a focused Gaussian beam as an example. Other types of beams can be done in a similar way. When the beam waist radius is much greater than the wavelength, the Davis first-order Gaussian beam description [141] has been found good enough. However, for tightly focused beams, one should consider the use of higher-order approximate expressions. In this thesis, we adopt the Davis-Barton fifth-order approximation [142]. The electric and magnetic fields in the beam coordinate system $(Ouvw)$ are given by

$$\begin{aligned}
E_u^i &= E_0\{1 + s^2(-\rho^2Q^2 + i\rho^4Q^3 - 2\xi^2Q^2) \\
&\quad + s^4[2\rho^4Q^4 - 3i\rho^6Q^5 - 0.5\rho^8Q^6 \\
&\quad + (8\rho^2Q^4 - 2i\rho^4Q^5)\xi^2]\}\psi_0\exp(-ikw) \\
E_v^i &= E_0\{s^2(-2\xi\eta Q^2) \\
&\quad + s^4[(8\rho^2Q^4 - 2i\rho^4Q^5)\xi\eta]\}\psi_0\exp(-ikw) \\
E_w^i &= E_0\{s(-2Q\xi) + s^3[(6\rho^2Q^3 - 2i\rho^4Q^4)\xi] \\
&\quad + s^5[(-20\rho^4Q^5 + 10i\rho^6Q^6 + \rho^8Q^7)\xi]\}\psi_0\exp(-ikw) \\
H_u^i &= H_0\{s^2(-2\xi\eta Q^2) \\
&\quad + s^4[(8\rho^2Q^4 - 2i\rho^4Q^5)\xi\eta]\}\psi_0\exp(-ikw) \\
H_v^i &= H_0\{1 + s^2(-\rho^2Q^2 + i\rho^4Q^3 - 2\eta^2Q^2) \\
&\quad + s^4[2\rho^4Q^4 - 3i\rho^6Q^5 - 0.5\rho^8Q^6 \\
&\quad + (8\rho^2Q^4 - 2i\rho^4Q^5)\eta^2]\}\psi_0\exp(-ikw) \\
H_w^i &= H_0\{s(-2Q\eta) + s^3[t(6\rho^2Q^3 - 2i\rho^4Q^4)\eta] \\
&\quad + s^5[(-20\rho^4Q^5 + 10i\rho^6Q^6 + \rho^8Q^7)\eta]\}\psi_0\exp(-ikw)
\end{aligned} \tag{3.11}$$

with

$$s = \frac{1}{kw_0}, \quad l = kw_0^2 \tag{3.12}$$

$$\rho^2 = \xi^2 + \eta^2, \quad \xi = \frac{u}{w_0}, \quad \eta = \frac{v}{w_0} \tag{3.13}$$

$$Q = \frac{1}{i + 2z/l}, \quad \psi_0 = iQ \exp(-iQ\frac{u^2 + v^2}{w_0^2}) \tag{3.14}$$

where E_0 and H_0 are the amplitudes of the electromagnetic field at the center of the beam, w_0 the beam waist radius and $k = 2\pi/\lambda$ the wave number.

However, to calculate the equivalent source of the incident wave and the total electromagnetic field on the virtual sphere we need the incident beam expressed in the particle coordinate system ($Oxyz$). The relation between the two systems can be obtained by a translation and three rotations according to Euler angles [143, 144]. It is worth to point out that, the Euler angles describe the rotations of the beam coordinate system ($Ouvw$), but not the particle system ($Oxyz$). Shown in Fig. 3.1 are (x_0, y_0, z_0) the coordinate of the beam center in the particle system and α, β, γ the three rotation Euler angles. The coordinates of a point in the particle system x, y, z can be expressed as function of the coordinates in the beam system u, v, w:

$$\begin{bmatrix} x - x_0 \\ y - y_0 \\ z - z_0 \end{bmatrix} = \mathbf{A} \begin{bmatrix} u \\ v \\ w \end{bmatrix} \tag{3.15}$$

where $\mathbf{A}$ is the transformation matrix:

$$\mathbf{A} = \begin{bmatrix} a_{11} & a_{12} & a_{13} \\ a_{21} & a_{22} & a_{23} \\ a_{31} & a_{32} & a_{33} \end{bmatrix} \tag{3.16}$$

and its elements are defined by

$$\begin{aligned}
a_{11} =& \cos\alpha\cos\beta\cos\gamma - \sin\alpha\sin\gamma \\
a_{21} =& -\cos\alpha\cos\beta\sin\gamma - \sin\alpha\cos\gamma \\
a_{31} =& \cos\alpha\sin\beta \\
a_{21} =& \sin\alpha\cos\beta\cos\gamma + \cos\alpha\sin\gamma \\
a_{22} =& -\sin\alpha\cos\beta\sin\gamma + \cos\alpha\cos\gamma \\
a_{23} =& \sin\alpha\sin\beta \\
a_{31} =& -\sin\beta\cos\gamma \\
a_{32} =& -\sin\beta\sin\gamma \\
a_{33} =& \cos\beta
\end{aligned} \tag{3.17}$$

Similarly, the electric and magnetic field components of the incident beam in the two coordinate systems are related by:

$$\begin{bmatrix} E_x^i \\ E_y^i \\ E_z^i \end{bmatrix} = \mathbf{A} \begin{bmatrix} E_u^i \\ E_v^i \\ E_w^i \end{bmatrix}, \quad \begin{bmatrix} H_x^i \\ H_y^i \\ H_z^i \end{bmatrix} = \mathbf{A} \begin{bmatrix} H_u^i \\ H_v^i \\ H_w^i \end{bmatrix} \tag{3.18}$$

We would point out that the Eqs. (3.15) - (3.18) are valid for any shaped beam. In the following section, we will apply the method presented above to the evaluation of the RPF and the torque exerted by a Gaussian beam on different shaped particles.

3.2 Numerical results

Based on the algorithm described above, a code for computing RPF and torque has been realized in Fortran 95. Moreover, parts of the code are parallelized with shared memory multiprocessing programming-OpenMP. All the computations are performed on Compute node-dx360 M2 of calculator *ANTARES* in "Centre de Ressources Informatiques de HAute-Normandie"(CRIHAN), France. Each node has bi-Quad-Core Intel Nehalem EP@2.8 GHz and maximum 96 GB DDR3 memory. Mesh density in the numerical realization is set to about $0.08 - 0.1\ \lambda$. The GMRES iteration solver is employed for solving the final matrix equation system.

The RPF and the torque on the particle are proportional to the power of the incident beam. The results presented in this section are normalized according to the power of the Gaussian beam given by [142]:

$$P = \frac{1}{2}\pi w_0^2 I_0 (1 + s^2 + 1.5s^4) \tag{3.19}$$

and the intensity I_0 is related to the amplitude of the electric field by $I_0 = E_0^2/(2Z_1)$ with $Z_1 = (\mu_1/\varepsilon_1)^{1/2}$.

3.2.1 Radiation pressure force

We first examine the accuracy and capability of the presented method for computing RPF on a homogenous particle. For comparison, the radiation pressure crossections (RPCS) computed by Ren [70] with GLMT developed is chosen and the RPF is related to the RPCS by

$$C_{pr} = cF \tag{3.20}$$

where c denotes the light speed in vacuum.

We check first the validity of our method and our code by comparing the radiation pressure cross section (RPCS) calculated with GLMT by Xu *et al.* [12]. Consider a spheroidal particle of slightly volatile silicone oil ($m = 1.5$) illuminated by a Gaussian beam. RPCS as a function of the beam center position along z-axis computed by MLFMA is presented in Fig. 3.2. A comparison of the results for $a/b = 1.05$ and 1.1 with those of Xu *et al.* (Fig. 9 in [12]) shows that the agreement is very good. We have also calculated RPCS on a sphere with GLMT in order to evaluate the precision of MLFMA. We find that the results of GLMT and of MLFMA (solid curve and dot symbols in Fig. 3.2) are in good agreement with about 2% discrepancy. One reason for this is the different computation algorithms employed in these two methods. Another possible reason is due to the precision of the description of the beam since we use directly analytical electromagnetic field expression [142] while in GLMT the beam is expressed in beam shape coefficients calculated by localized approximation [7]. Differences caused by the latter known to be relatively small or even vanish when the beam waist is large enough. To prove this, we compute RPF on a spherical particle with different w_0 when the beam center coincide with the particle center. We define the relative error as:

$$\frac{|F_{GLMT} - F_{MLFMA}|}{|F_{GLMT}|} \times 100\% \tag{3.21}$$

The relative errors between the RPF computed by the MLFMA and the GLMT as a function of w_0 are shown in Fig. 3.3. As expected, the relative error decrease with the increment of w_0 and finally approximate to almost a constant. This constant difference is caused by different computation algorithms employed and depends on electrical size of the particle as well as its relative refractive. When the beam radius is set to $w_0 = 2\mu\text{m} = 2\lambda$, the relative error in Fig. 3.3 is about 11%. Despite of the difference between two numerical methods (about 4%), it is still larger than that in Fig. 3.2 (about 2%). This is because, for a larger particle, a more important difference between the Davis-Barton analytical electromagnetic field expression and the localized approximation beam description will happen.

Next, we will enlarge radius of the spherical particle to 16 μm and discuss the case of off-axis (move along x-axis) incidence of the beam. Since the beam center is located along the x-axis, we have $y_0 = 0$, $z_0 = 0$. In this calculation, the whole surface of the

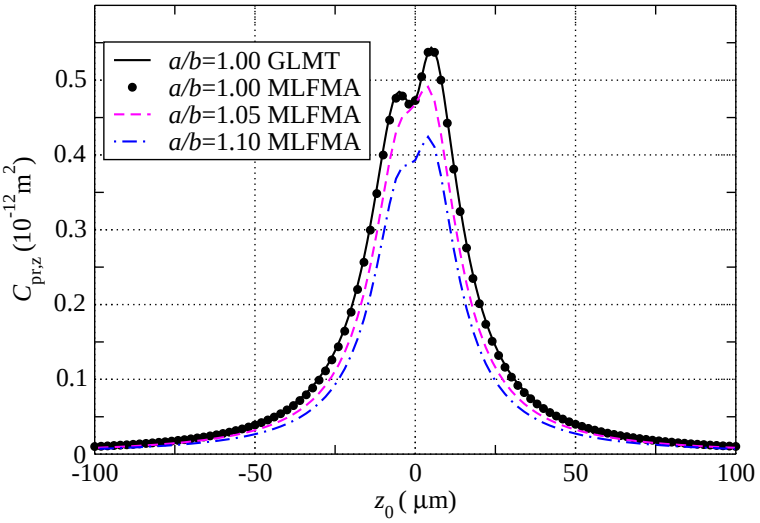

Figure 3.2: Comparison of the longitudinal RPF on a prolate silicone oil particle ($m = 1.5$) computed by our approach and by GLMT [12]. The wavelength and the beam waist radius of the Gaussian beam are respectively $\lambda = 0.5145$ μm and $w_0 = 2\lambda$. The center of the particle moves along z axis. The transversal radius of the particle is $b = 1$ μm while the radius a along z axis varies with three aspect ratio values $a/b = 1.0$, 1.05 and 1.10.

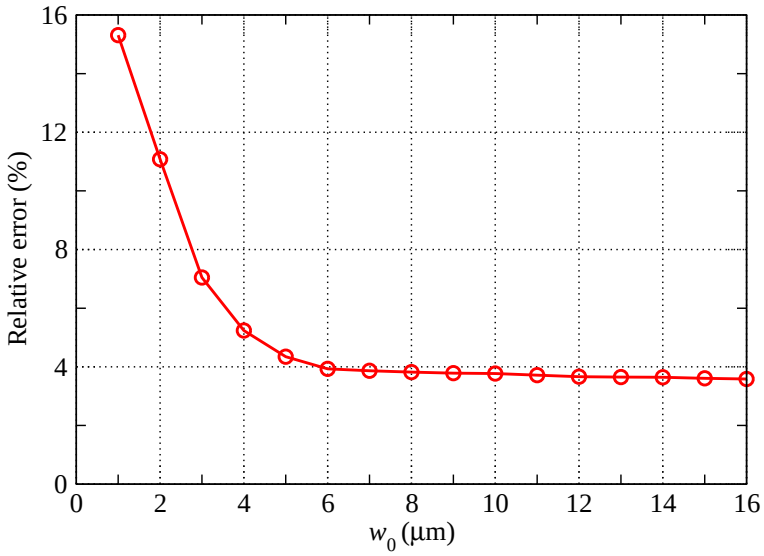

Figure 3.3: Relative error of longitudinal RPF on a sphere water droplet $m = 1.33$ with $a = b = c = 8$ μm versus different waists of incident beams.

particle S is discretized into 1.08×10^6 edges with total of 2.16×10^6 unknowns. We set the beam waist $w_0 = 3\mu$m. The longitudinal and the transverse RPFs obtained from the MLFMA are presented in Fig. 3.4(a) and Fig. 3.4(b) together with those from the GLMT. As shown in these figures, again good agreements can be observed. This computation by MLFMA costs 50GB memory and 2140 seconds wall time with 10 threads for computing each RPF point.

Next, we study effects on RPF of the incidence angles for spheroidal particles. We fix ($x_0 = y_0 = z_0 = 0$) and let the Gaussian beam incident on a spheroid polystyrene particle ($m = 1.59$) located in water ($m = 1.33$) at different incidence angles β and set $\alpha = \gamma = 0°$. In such condition, the direction of the incident beam varied in the $x - z$ plane. We compute the RPF by this Gaussian beam under two different conditions. In the first condition, we fix the center of the beam to be coincident with the center of the particle $x_0 = 0$, $y_0 = 0$, $z_0 = 0$ and the beam incident direction rotate around its center, as shown in Fig. 3.5(a). Second, the beam incident direction is rotated but the beam center keep a distance equal to the radius c along z axis from the bottom extremity of the particle, as schetched in Fig. 3.5(b). The three components of RPF are depicted in Fig. 3.6 and Fig. 3.7. The main difference between this two figures is that, there exist a positive x component force in Fig. 3.7 at about 15° to 55°. Explanation for this is that, when a beam is incident on a particle, there is not only a force pushing the particle in its incident direction, but also a force pulling transparent particles with an index of refraction higher than the surrounding towards the beam axis. When the center of the beam coincide with center of the particle, this force is very small, and when $\beta = 90°$ this force vanishes. However, when the particle center keeps a distance from the beam center, this force exist and sometimes may be even very large. Hence the total force in x direction will change to the opposite direction (pulling the particle towards the beam axis). That is also the reason when $\beta = 90°$ the z component of RPF is non zero in Fig. 3.7. The whole outer surface of the spheroid was discredited into triangles leading to 1.41×10^6 unknowns. The total required memory is 28 GB. The real computation time with 10 threads for one point including solving the resultant matrix equation system is 1800 seconds.

The above numerical experiments show the great capability of the presented MLFMA for computing RPF on spheroid particles. Our approach can be applied to compute RPF of any shaped particle. As an example, we perform numerical experiments on a symmetric biconcave shaped red blood cell-like particle ($m = 1.4$) in water ($m = 1.33$) versus beam incident direction for two wavelengths. To describe the

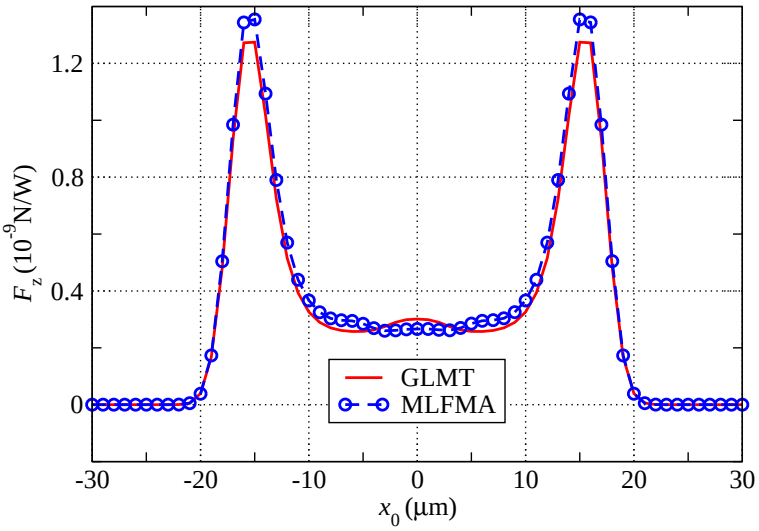

(a) Longitudinal

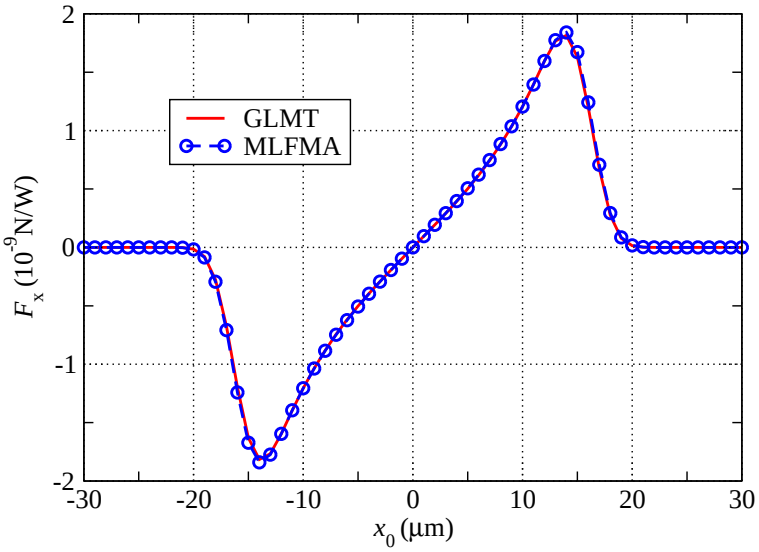

(b) Transverse

Figure 3.4: RPFs versus particle location along the x axis. The beam waist radius of the incident Gaussian beam is set to $w_0 = 3\mu$m, the size of the particle is assumed to be $a = b = c = 16$ μm.

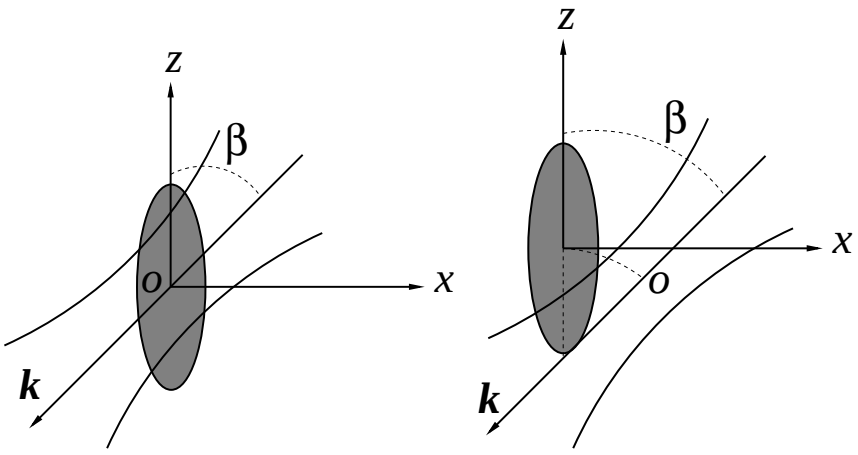

(a) Around the center of particle

(b) Around the bottom extremity of particle

Figure 3.5: Sketch of the beam incident rotation direction.

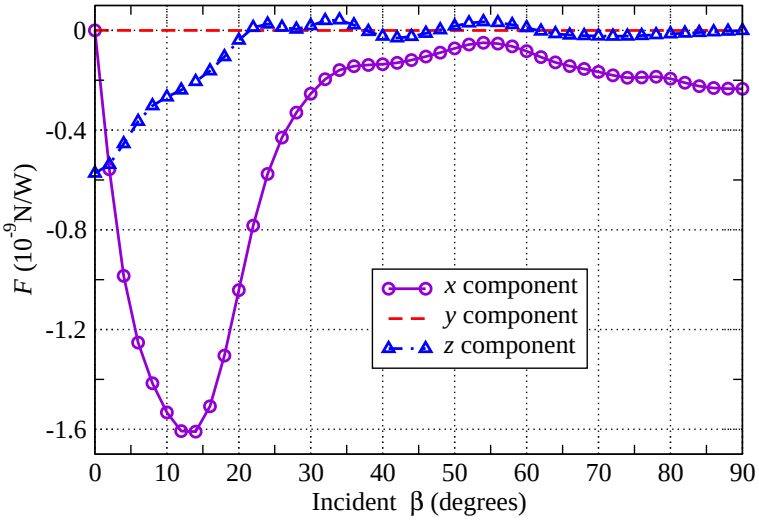

Figure 3.6: RPF on an ellipsoid ($a = 3$ μm, $b = 3$ μm, $c = 12$ μm) polystyrene particle ($m = 1.59$) in water ($m = 1.33$) illuminated by a Gaussian beam ($\lambda = 0.5145$ μm, $w_0 = 1.3$ μm). The incident beam rotates around the center of the particle.

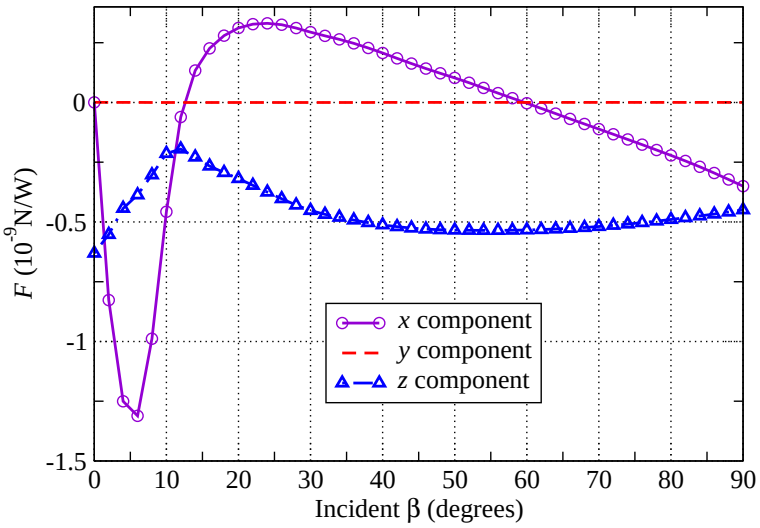

Figure 3.7: Like in Fig. 3.6, but the incident beam rotates around the bottom extremity of the particle.

biconcave disc shape of the cell, we employ a simple surface function as:

$$r(\theta_A, \phi_A) = asin^q\theta_A + b \tag{3.22}$$

We set $a = 3.8$, $b = 0.41$, $q = 9$ and it is of the same size as the one with $q = 9$ in [145]. The triangle patches generated on the surface of the cell is shown in Fig. 3.8. Fig. 3.9(a)-3.9(b) show the longitude and traverse RPF versus different beam incident directions. When a beam incident on a transparent particle, usually, it will push the particle move along the incident direction. However, in Fig. 3.9(a), because of the shape of the cell-like particle, when the incident wavelength $\lambda = 0.5145$ μm and beam center not far from the point $x_0 = 0$, $y_0 = 0$, $z_0 = 0$, the longitude RPF on this particle is relatively small and opposite to the propagation direction of the beam. For the same reason, in Fig. 3.9(b), there exists a large range of incident β that the x direction component of the RPF opposite to each other for these two incident wavelengths.

3.2.2 Radiation torque

In this section, we discuss the numerical computation of the radiation torque with MLFMA. We first check the validity of our method and our code by comparing the radiation torque calculated with GLMT by Xu *et al.* [75]. Consider a spheroidal particle ($m = 1.573 + 6.0 \times 10^{-4}i$) illuminated by an Gaussian beam. The radiation

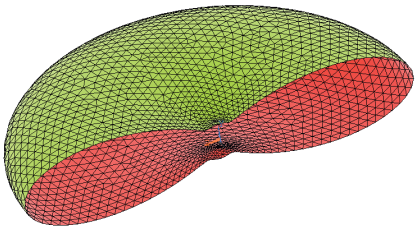

Figure 3.8: Meshes for the biconcave shaped red blood cell-like particle.

torque as a function of the incident angle β computed by MLFMA is presented Fig. 3.10. A comparison of the results for $a/b = 1.05$ and 1.1 with those of Xu *et al.* (Fig. 3 in [75]) shows that the agreement is very good.

Next, we fix ($x_0 = y_0 = z_0 = 0$) and let the Gaussian beam ($\lambda = 0.5145$ μm, $w_0 = 1.3$ μm) incident on a spheroid polystyrene particle ($m = 1.59$) located in water ($m = 1.33$) at different incidence angles β and set $\alpha = \gamma = 0°$. In such condition, the direction of the incident beam varied in the (x, z) plane. We compute the radiation torque by this Gaussian beam under two different conditions. First, the beam coincide with the center of the particle $x_0 = 0$, $y_0 = 0$, $z_0 = 0$ and the incident beam rotates around its center as shown in Fig. 3.5(a). Second, the incident beam rotates around the bottom extremity of particle but the beam center keeps a distance equal to the radius c along the z axis, as shown in Fig. 3.5(b). The computed torques are shown in Fig. 3.11. Since there are no torque components about the x and z axes, only y component of the torque is plotted. Here we define the positive (negative) torque causing counterclockwise (clockwise) rotation of the spheroid particle about the y axis. When the direction of the incident beam rotation around the center of the particle ($x_0 = y_0 = z_0 = 0$), the radiation torque always makes the spheroid particle rotation counterclockwise. Such phenomenon can be easily understood, because in both numerical and experimental researches, optically trapped objects were found trying to align its major axis along the direction of the laser beam propagation under a rotational torque. When the beam rotates around the bottom extremity of spheroid and incident angle $\beta = 0°$, there is no rotational torque because of symmetry of the particle. When $\beta = 90°$ the radiation force will push the particle along its propagation direction ($-x$ axis). Hence there is a positive torque at $\beta = 90°$ because lower part of the spheroid will experience larger radiation force than the upper part. Compared with the center-around rotation beam incidence, when the direction of the beam

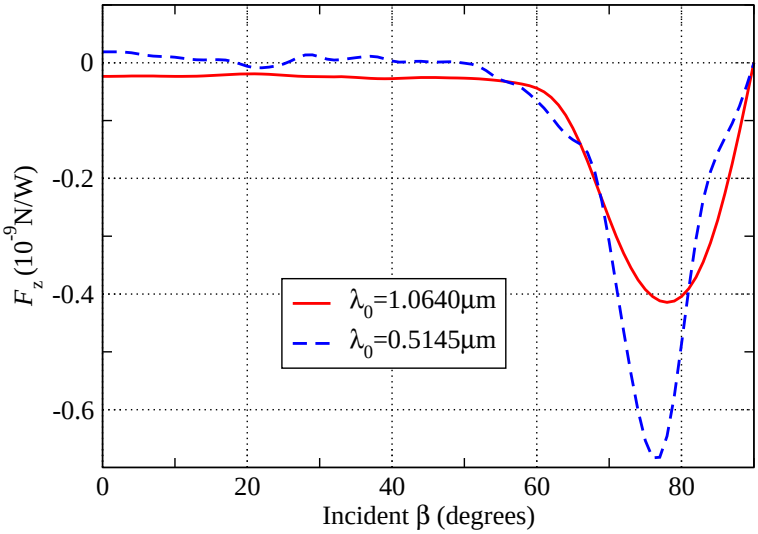

(a) Longitudinal

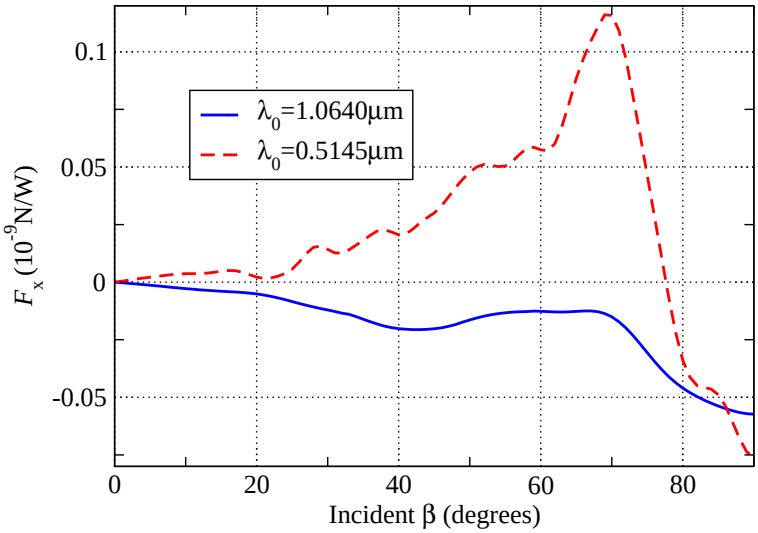

(b) Transverse

Figure 3.9: RPF on a biconcave cell-like particle ($m = 1.4$) in water ($m = 1.33$) versus beam incident angle for two wavelengths. The waist radius of the Gaussian beam is $w_0 = 2$ μm. The diameter of the cell-like particle is $d = 8.419$ μm (xy plane), the maximum and the minimum thickness are $h_M = 1.765$ μm and $h_m = 0.718$ μm.

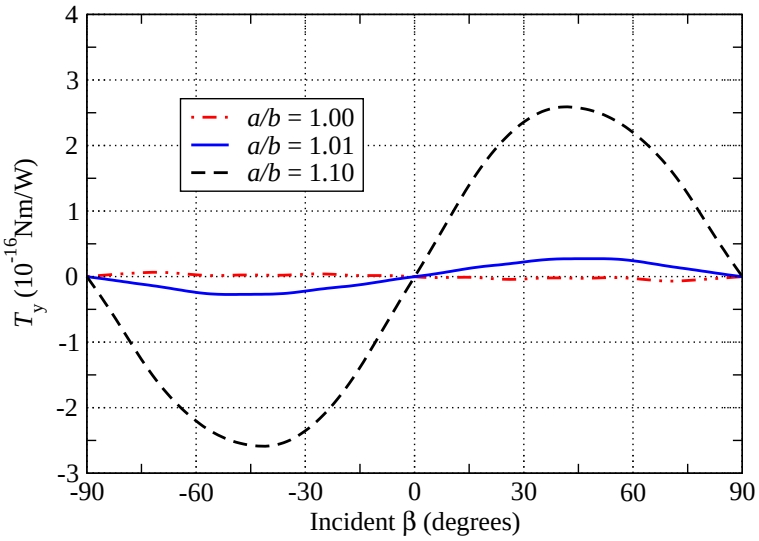

Figure 3.10: Comparison of the radiation torque on two prolate particles ($m = 1.573 + 6.0 \times 10^{-4}i$) of aspect ratios a/b=1.01 and 1.10 computed by our approach. The wavelength and the beam waist radius of the Gaussian beam are respectively $\lambda = 0.785$ μm and $w_0 = 1.0$ μm. The center of the particle coincides with the beam center. The spheroids have the same volume as the sphere of radius $r = 1.0$ μm (Fig. 3 in [75]).

rotation around the extremely bottom of the particle, at the range of about 25° to 55° there exist torques try to make the particle rotate clockwise. The explanation for this is that, when a beam incident on a particle, there is not only a force *pushing* the particle in its incident direction, but also a force *pulling* transparent particles with an index of refraction higher than the surroundings towards the beam axis. The *pushing* force will generate a positive torque and the *pulling* force sometimes can generate a negative torque even larger than that generated by the *pushing* force.

Next, we perform numerical experiments on the symmetric biconcave shaped red blood cell-like particle as shown in Fig. 3.8. The corresponding radiation torque is shown in Fig. 3.8 versus different incident incident β is computed, as shown in Fig. 3.12. It can be observed in this figure, in all range of 0° to 90°, the radiation torques are always negative causing clockwise rotation of the biconcave cell. This is because the biconcave cell can approximately be treated as a oblate spheroid particle. This agrees with the conclusion that optically trapped objects were found trying to align its major axis along the direction of the laser beam propagation under a rotational torque. Also our simulated results in Fig. 3.11 and Fig. 3.12 agree with the conclusion in [75], the positive (negative) torque causing counterclockwise (clockwise) rotation

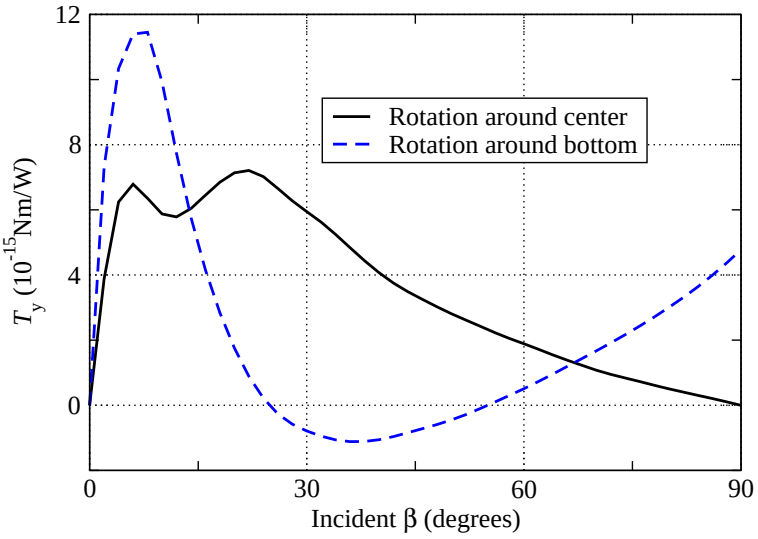

Figure 3.11: Radiation torque on an ellipsoid ($a = 3$ μm, $b = 3$ μm, $c = 12$ μm) polystyrene particle ($m = 1.59$) in water ($m = 1.33$) illuminated by a Gaussian beam ($\lambda = 0.5145$ μm, $w_0 = 1.3$ μm). The incident beam rotates around the center of the particle as shown in Fig. 3.5(a).

of the prolate spheroid particle about the y axis, but opposite rotation direction for the oblate spheroid particle.

At last, to give a final examples of MLFMA capabilities, we simulate the radiation torque on a regular motor, as shown in Fig. 3.13. The motor is immersed in water. A middle hole of 2 μm in diameter is made to accommodate the axle. The individual fan thickness is 1 μm for the motor. The center of the incident Gaussian beam propagating in $-z$ direction keeps a constant distance of 10 μm away from center of the motor in its incident direction [134]. The radiation torques for the micro motor versus beam center move along y axis are shown in Fig. 3.14. The torque is found symmetrical with respect to the axis $y_0 = 0$. Because of the symmetric nature of the structure, there is only the torque component in x axis.

3.3 Conclusions

In this Chapter, the SIE method is used for computing RPF and torque on arbitrary shaped homogenous particles. Triangles patches are used to discrete the outer surface of the particles, which make this method especially flexible and efficient for modeling irregular shaped particles. The MLFMA is employed to reduce the computational

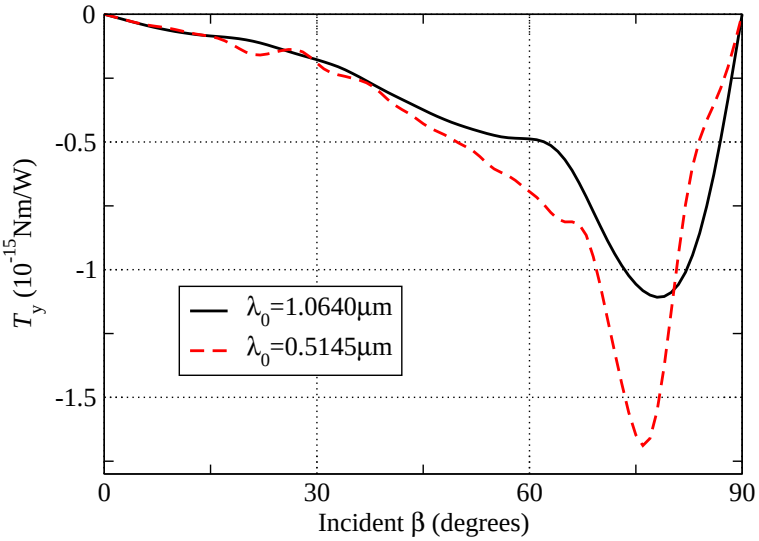

Figure 3.12: Comparison of the radiation torque on the biconcave cell-like particle in water (as shown in Fig. 3.8). The waist radius of the Gaussian beam is $w_0 = 2$ μm. The diameter of the particle is $d = 8.419$ μm (xy plane), the maximum and the minimum thickness are $h_M = 1.765$ μm and $h_m = 0.718$ μm.

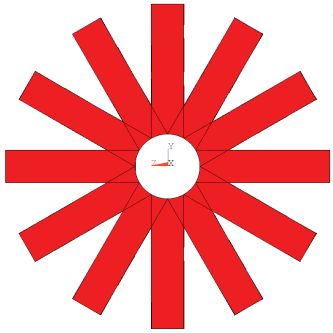

Figure 3.13: Geometry of the regular motor.

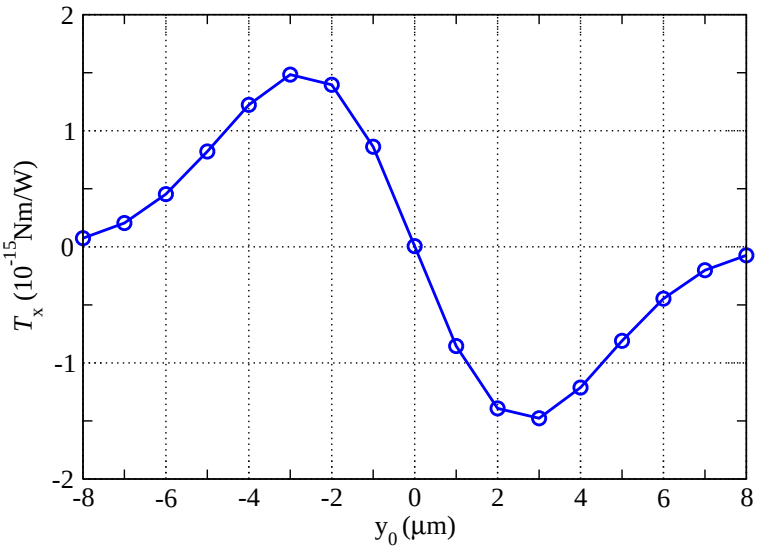

Figure 3.14: Torque versus a varying offset in y evaluated for a motor ($m = 1.58$) in water ($m = 1.33$). The incident beam is set to $\lambda = 1.07$ μm, $w_0 = 3.6$ μm and keep a constant distance $z = 10$ μm to center of the motor in its propagating direction. The motor is 2 μm in heights ($x - axis$) with diameters 10 μm ($yz - plane$).

and storage complexity. The RPF and torque are computed by integrating the dot product of the surface normal and the Maxwell stress tensor over a surface enclosing the particle. Furthermore, the analytical electromagnetic field expression in near region is used. The present method is validated and its capability illustrated in several characteristic examples. RPF and torque on an arbitrary particle by other kinds of shaped beams are under study.

Chapter 4

Computation of stress on arbitrarily shaped particles

A particle illuminated by a beam of light experiences a RPF, and this force can be used to trap and manipulate small particles without any mechanical contact. Various instruments have been developed to make use of this radiation force, such as the Optical tweezers, which use single focused beam to trap particles [61], while in the optical stretcher two shaped beams are employed [62]. Since then, optical trapping become a more and more important tool for researches in the fields of biology, physical chemistry and soft condensed matter physics [133, 66, 146]. When a soft particle is trapped or manipulated, its shape may be deformed due to the nonuniformity of the radiation stress on the surface, a sphere may become non-spherical. Knowing the deformation, one can discern properties of soft particles, such as viscoelastic properties of cells [62]. On the other hand, in many practical applications, the shape of particles is irregular. By applying a specific shaped beam, one may deform the particle as wanted due to the surface stress. Therefore, the numerical prediction of the surface stress on an arbitrarily shaped particle is of crucial importance for real-time applications.

Along with experimental researches, various kinds of computational methods have been developed to perform numerical prediction of radiation force exerted on particles by shaped beams. These methods include: GLMT [70, 71, 12], T-matrix technique[25, 80, 147, 85, 83, 148], DDA [86, 90, 91, 95, 149], FDTD [100, 99, 101] and FEM [102].

In principle, numerical methods for computing overall net force on a particle can also be applied for computing surface stress. But only a few studies on the surface stress of a soft particle have been reported. Ekpenyong *et al.* [150] and Sebastien

et al. [151] have employed the classical geometrical optics to approximate the stress distribution as well as to compute the deformation of a spherical particle with the elastic membrane theory. A rigorous theory (GLMT) and an approximate method (GO) have been applied by Xu *et al.* to the prediction of the optical stress distribution on the surface of a homogeneous sphere [152]. Similar work has been reported recently for an prolate spheroid in dual beam trapping of aspect ratio equal to 1.2 and$x < 50$ [153]. But neither the influence of aspect ratio nor the incident angle were studied. However, these parameters play crucial roles in the distribution of the surface stress. Furthermore, a spherical or spheroidal particle of soft material will be deformed under the radiation force. Therefore the numerical methods for the computation of surface stress on an arbitrary shape particles is to be developed. So far, GO and GLMT are difficult or even impossible to be applied to predict the surface stress on an non-spherical particles. In principle, numerical methods such as DDA, FDTD can be applied for arbitrary shaped particles. However, as far as we know, only one paper dealt with the surface stress on a biconcave red-blood cell with the plane wave incidence by using FDTD [154].

In this chapter, we report our study on the surface stress exerted on an arbitrary shaped soft particle with MLFMA [155]. This method can deal with particles larger than the above mentioned numerical techniques. It is more accurate than the high frequency asymptotic methods such as GO. Compared to the rigorous theory as GLMT, it is flexible and can be easily applied to arbitrary shaped particles and arbitrary shaped beams. For the convenience of presentation, we first focus our attention to the radiation stress on spheroids with different aspect ratios and beam incidences. This is because, in one hand, a spheroid is the simplest non-spherical particle, its physical characteristics can be observed through ray tracing in VCRM; on the other hand, the aspect ratio of a spheroid can be easily controlled while keeping its volume the same as the original sphere. Moreover, the particle size should be larger than the incident wavelength and the beam waist in order to show clearly the effects of the aspect ratio. Here we use a single Gaussian beam as an example for detailed analysis. Surface stress on a soft particle trapped with more than one beam incidence can be easily obtained by using the superposition principle. Then, our computations are extended to an irregular shaped biconcave cell-like particle trapped in water by a Gaussian beam with different beam waist radii and incident directions. An example is also given to show the capabilities of our algorithm. When parallelized with MPI on a memory distributed computer system, the size parameter can be as large as several hundred, i.e. $x = 640$.

4.1 Computation of optical stress by SIE with MLFMA and VCRM

To compute optical stress on the surface of an arbitrary shaped particle, we first need to solve a light scattering problem. By supposing the boundary S of the homogeneous dielectric particle is taken as the electromagnetic fields equivalent surface, with the incident electromagnetic fields denoted as $(\mathbf{E}^i, \mathbf{H}^i)$ and the equivalent electric and magnetic currents as $(\mathbf{J}, \mathbf{M})$, we can obtain the equation form of combined tangential formulation (CTF) [121], as described in Chapter 2. Then by following the procedure of the MoM, and using the RWG vector basis functions [51], a complete matrix equation system can be obtained. After solving this matrix equation with iterative solvers, such as the GMRES, the equivalent sources $(\mathbf{J}, \mathbf{M})$ on the surface S can be known. To speed up the matrix-vector multiplication and reduce the memory requirements, the MLFMA is employed here, which can reduce both the time and the memory complexity from the order of N^3 or N^2, to the order $NlogN$, with N the number of unknowns [123, 49, 52].

When an arbitrarily shaped particle is illuminated by a shaped beam, the surface stress at $\mathbf{r}$ can be calculated by:

$$\mathbf{F} = -\hat{\mathbf{n}} \cdot \left[\overleftrightarrow{T}_2 (\mathbf{r}) - \overleftrightarrow{T}_1 (\mathbf{r}) \right] \tag{4.1}$$

where $\hat{\mathbf{n}}$ is the outward normal of the particle surface and

$$\begin{aligned} \overleftrightarrow{T}_l (\mathbf{r}) &= \frac{1}{2}\mathrm{Re}[\varepsilon_l \mathbf{E}_l(\mathbf{r})\mathbf{E}_l{}^*(\mathbf{r}) + \mu_l \mathbf{H}_l(\mathbf{r})\mathbf{H}_l{}^*(\mathbf{r}) \\ &- \frac{1}{2}(\varepsilon_l |\mathbf{E}_l(\mathbf{r})|^2 + \mu_l |\mathbf{H}_l(\mathbf{r})|^2) \overleftrightarrow{I}] \end{aligned} \tag{4.2}$$

is the time average Maxwell stress tensor outside ($l = 1$) and inside ($l = 2$) the particle, the star * stands for conjugate, and $\mathbf{E}_l(\mathbf{r})$ and $\mathbf{H}_l(\mathbf{r})$ are total electromagnetic fields. We should note that there is a minus sign in Eq. (4.1) because the stress exerted by the external (internal) fields acts on the external (internal) sides of the surface.

Once the equivalent electric and magnetic currents $\mathbf{J}$ and $\mathbf{M}$ are solved by using SIE with MLFMA, the scattered fields $\mathbf{E}_1^s$ and $\mathbf{H}_1^s$ at any point outside the particle can be obtained by:

$$\begin{aligned} \mathbf{E}_1^s &= Z_1 \mathbf{L}_1(\mathbf{J}) - \mathbf{K}_1(\mathbf{M}) \\ \mathbf{H}_1^s &= 1/Z_1 \mathbf{L}_1(\mathbf{M}) - \mathbf{K}_1(\mathbf{J}) \end{aligned} \tag{4.3}$$

The operators $\mathbf{L}_1$ and $\mathbf{K}_1$ are defined as:

$$\mathbf{L}_1\{\mathbf{X}\}(\mathbf{r}) = jk_1 \int_S [\mathbf{X}(\mathbf{r}') + \frac{1}{k_1^2}\nabla(\nabla' \cdot \mathbf{X}(\mathbf{r}'))]G_1(\mathbf{r}, \mathbf{r}')d\mathbf{r}' \tag{4.4}$$

$$\mathbf{K}_1\{\mathbf{X}\}(\mathbf{r}) = \int_S \mathbf{X}(\mathbf{r}')\times\nabla' G_1(\mathbf{r}, \mathbf{r}')d\mathbf{r}' \tag{4.5}$$

where $j = \sqrt{-1}$, $k_1 = \omega(\mu_1/\epsilon_1)^{1/2}$, $\mathbf{X}$ is either the equivalent electric current $\mathbf{J}$ or the equivalent magnetic current $\mathbf{M}$ on S, and

$$G_1(\mathbf{r}, \mathbf{r}') = \frac{\exp(-jk_1|\mathbf{r} - \mathbf{r}'|)}{4\pi|\mathbf{r} - \mathbf{r}'|} \tag{4.6}$$

Then the total electromagnetic fields outside the particle can be known by:

$$\begin{aligned} \mathbf{E}_1(\mathbf{r}) &= \mathbf{E}_1^s(\mathbf{r}) + \mathbf{E}^i(\mathbf{r}) \\ \mathbf{H}_1(\mathbf{r}) &= \mathbf{H}_1^s(\mathbf{r}) + \mathbf{H}^i(\mathbf{r}) \end{aligned} \tag{4.7}$$

According to the boundary conditions on the surface of the particle, the tangential components of EM fields are continuous

$$\begin{aligned} \mathbf{E}_2^t = \mathbf{E}_1^t = \hat{\mathbf{n}} \times (\mathbf{E}_1 \times \hat{\mathbf{n}}) \\ \mathbf{H}_2^t = \mathbf{H}_1^t = \hat{\mathbf{n}} \times (\mathbf{H}_1 \times \hat{\mathbf{n}}) \end{aligned} \tag{4.8}$$

and the relations for the normal components are

$$\begin{aligned} \varepsilon_2\mathbf{E}_2^n = \varepsilon_1\mathbf{E}_1^n = \varepsilon_1(\mathbf{E}_1 \cdot \hat{\mathbf{n}})\hat{\mathbf{n}} \\ \mu_2\mathbf{H}_2^n = \mu_1\mathbf{H}_1^n = \mu_1(\mathbf{H}_1 \cdot \hat{\mathbf{n}})\hat{\mathbf{n}} \end{aligned} \tag{4.9}$$

By using the above boundary conditions, the total electromagnetic fields inside the particle can be obtained and the surface stress can be computed by Eq. (4.1). It can be known from Eqs. (4.1), (4.8) and (4.9) that the surface stress is always normal to the particle surface [154].

To show the precision and the capability of our method for the computation of surface stress, we use a focused Gaussian beam as an example. Other types of beams can be done in a similar way. Here we adopt the Davis-Barton fifth-order approximation [142] of Gaussian beam and the stress on the particle is proportional to the power of the incident beam and here it is normalized according to the power of the Gaussian beam.

4.2 Numerical results and discussions

Based on the algorithm described in the previous section, a code for computing the stress on the surface of a particle has been written in Fortran 95. A part of the code is parallelized with shared memory multiprocessing programming – OpenMP. To further improve its capability, for large prolate spheroids, this code is parallelized with MPI on memory distributed computer system by following [58].

We check firstly the validity of our program by comparing the stress profile calculated with GLMT by Xu *et al.* [152] for a water droplet ($m = 1.330 + 1.342 \times 10^{-7} i$) of radius $a = 20$ μm illuminated by a Gaussian beam of waist radius $w_0 = 16$ μm. The wavelength of the incident beam is $\lambda = 0.785$ μm and the size parameter of the particle is$x = 160$. In this calculation, the whole surface of the droplet is discretized into 1.62×10^6 triangle patches with total 4.86×10^6 unknowns. This calculation takes about 37 GB memory and 70 minutes CPU time with 10 OpenMP threads. The surface stress profile computed by MLFMA is presented in Fig. 4.1. This profile is in good agreement with GLMT results in Fig. 10 in [152]. We have also compared the stress profiles computed by our method with those in Fig. 3 and Fig. 5 in [152] and the agreement is always very good. Also, as another validation, the integral of the stress profile over the surface of a non-absorbing sphere has been carried out and the result agrees perfectly with the total radiation force from the MLFMA solution presented in our previous paper [156].

In what follows, we study the radiation stress on non-spherical particles. First, we choose a spheroid particle to study the influence of the aspect ratio, the beam waist radius and the incidence conditions. We still consider a water droplet, initially spherical of radius 8 μm, deformed to a spheroid of different aspect ratios c/a with c the radius of the spheroid along z axis and a along x and y axis. Then, the surface stress on a more complex biconcave cell-like particle will be studied. At last, surface stress on a large prolate spheroid with size parameter up to 640 is computed to show great capability of the presented method.

The wavelength of the incident beam is fixed to 0.785 μm for water droplet and 0.6328 μm in vacuum for biconcave cell-like particle. We denote by β the angle between the propagation direction of the incident beam and $+z$ axis. To study the influence of beam waist radius, we choose $w_0 = 100$ μm and 2 μm for all the particles except in the last example for a large spheroid where $w_0 = 50$ μm. Since the stress on the surface of a particle is always normal to the particle surface and the origin of the

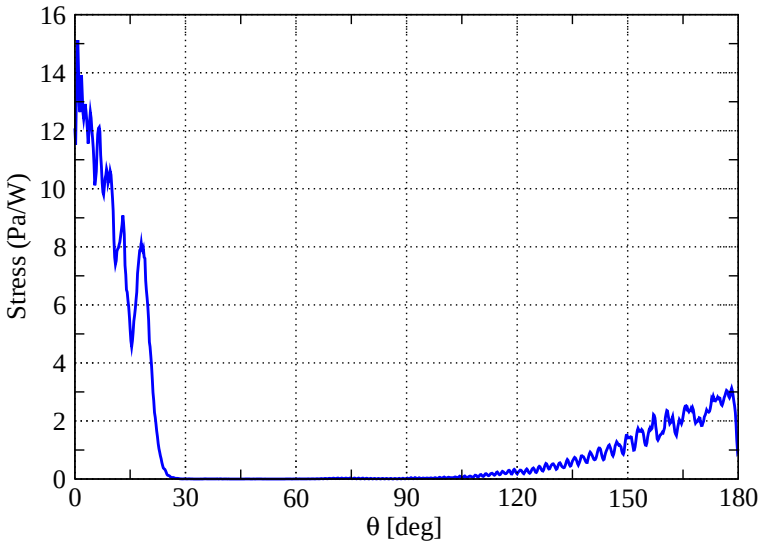

Figure 4.1: Stress profile on the surface of a spherical water droplet of radius 20 μm and refractive index $m = 1.330 + 1.342 \times 10^{-7}i$ illuminated by a Gaussian beam polarized in the x direction of wavelength 0.785 μm and waist radius $w_0 = 16$ μm. The droplet center coincides with that of the beam. Cartesian plot of the stress is in the xz plane.

particle coordinate system is at the center of the particle, only the polar angle θ is necessary to locate points on the surface of spheroids and only one curve is sufficient to present the stress profile. Two polarizations of incident beam will be considered, one in xz plane and the other in yz plane.

4.2.1 Large incident beam

For practical consideration and convenience of presentation, a large Gaussian beam will be used to study the case of plane wave. In such way, the stress can be expressed in pascal per watt (Pa/W), independent of the power of the incident laser beam, and it is easy to compare quantitatively the stress with the case where the particle is illuminated with a focused beam.

When the beam waist of the incident beam is large compared to the particle size a (say $w_0 = 100$ μm for a particle of 20 μm or 30 μm), and both a and w_0 much greater than the wavelength, the ray model can be applied to analyze the physical effects and to help to check the results, at least qualitatively. Therefore, each case will be come with an analysis based on our recently developed ray tracing model VCRM [22]. To ease the understanding of such analysis, we recall some effects on the stress

prediction by ray tracing. When a ray is incident from outside to the particle ($p = 0$), the forces caused by the reflection and the refraction are in the opposite directions, while if a ray is incident on the internal surface of a particle ($p > 0$), the forces caused by the reflection and the refraction are in the same direction [152]. In general case, low order rays $p = 0,\ 1$ provide the major contributions to the surface stress since the amplitude of higher order rays decreases rapidly.

We begin with the simplest case: a spherical water droplet of radius 8 μm. The computed stress profile in xz plane together with the ray tracing graph are shown in Fig. 4.2. Since in such condition, the surface stress profile is symmetric about z axis, only stress profile in the range of $\theta = 0°$ to $180°$ is plotted. It can be seen that the rays of order $p = 1$ focus near the $+z$ axis from $\theta = -20°$ to $\theta = 20°$, the surface stress in that range is therefore much larger than elsewhere.

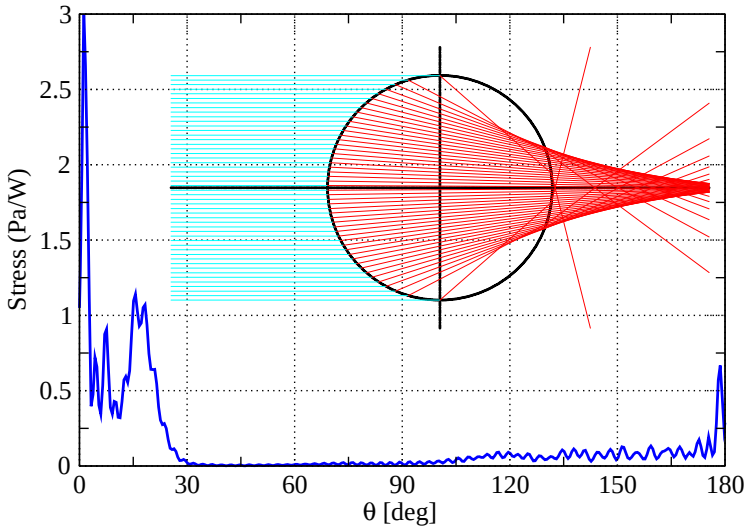

Figure 4.2: Stress profile on the surface of a spherical water droplet ($m = 1.33$) with radius 8 μm illuminated by a large Gaussian beam and ray tracing of order $p = 1$. The wavelength of the incident beam is 0.785 μm and its beam waist $w_0 = 100$ μm.

A prolate spheroid can be regarded as a sphere by stretching so that its volume remains the same. The computed stress profile on surface of a prolate spheroid with aspect ratio $c/a = 3/2$ is shown in Fig. 4.3. The surface stress has a peak at 0° and and decreases rapidly to nearly zero at about 10°. The ray tracing shows that, with this aspect ratio, the first order rays ($p = 1$) focus strongly near $+z$ axis and the number of the rays near $+z$ axis is the largest and decreases rapidly to nearly zero at 10°. Besides, at a point on or near $+z$ axis, the reflection and refraction force has

no or very small tangential component and they are in the same direction, hence the stress on and near $+z$ axis is much larger than the maximum stress of a sphere and more focused in the forward direction.

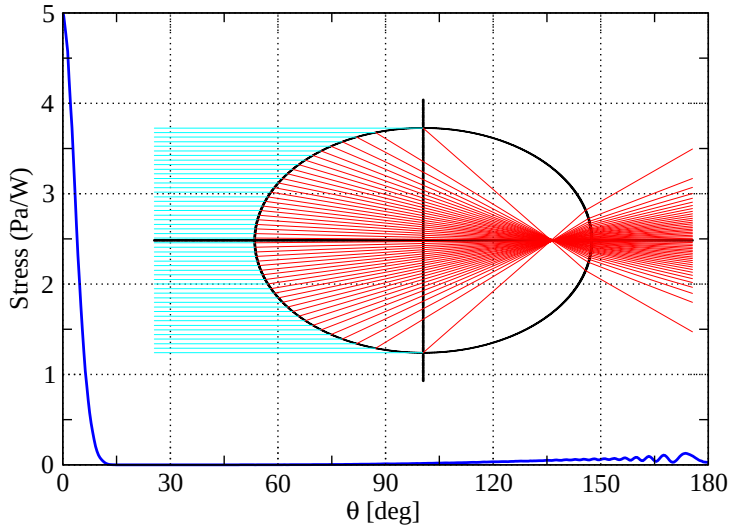

Figure 4.3: Stress profile on the surface of a prolate spheroid with aspect ratio $c/a = 3/2$ and ray tracing of order $p = 1$. The prolate spheroid has the same volume as a sphere of radius 8 μm. Other parameters are the same as those in Fig. 4.2.

We increase the aspect ratio to $c/a = 2$ and find that the stress maximum go apart from the symmetric axis, in about 15° (noted as point **A** in Fig. 4.4). The ray tracing shows that many rays of order $p = 1$ focus in that region. However, the rays arriving at this point experienced an incident/refraction angle larger than in the case of sphere shown in Fig. 4.2, the Fresnel transmission coefficient is then smaller, hence the maximum value of stress is smaller than that on the sphere.

When we further increase the aspect ratio to $c/a = 5/2$, the maximum stress appears on a point near $\theta = 23°$ (point **A** in Fig. 4.5) because most of the first order rays focus in that direction. We find also another maximum near 7°. This is not a contribution of the first order rays, but the second order rays ($p = 2$). We observe that lots of the seconde order rays focus at a point around 7° (point **B**). When the aspect ratio is increased to $c/a = 3$, a similar phenomenon is observed (Fig. 4.6). But the stress due to the second order rays (point **B**) is larger than that of the first order rays (point **A**). This is because the rays at point **B** are nearly normal to the surface while the rays at point **A** are more tilted to the surface such that the tangent components of the electromagnetic fields are less than that at point **B**.

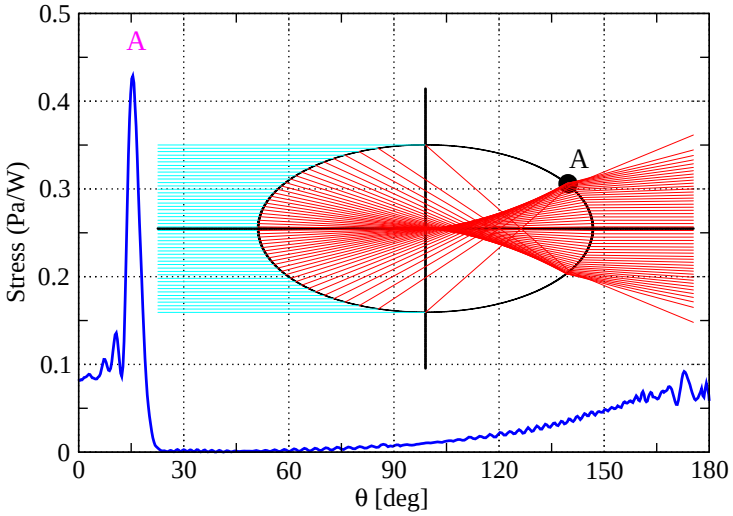

Figure 4.4: Stress profile on the surface of a prolate spheroid with aspect ratio $c/a = 2$ and ray tracing of order $p = 1$. The prolate spheroid has the same volume as a sphere of radius 8 μm. Other parameters are the same as those in Fig. 4.2.

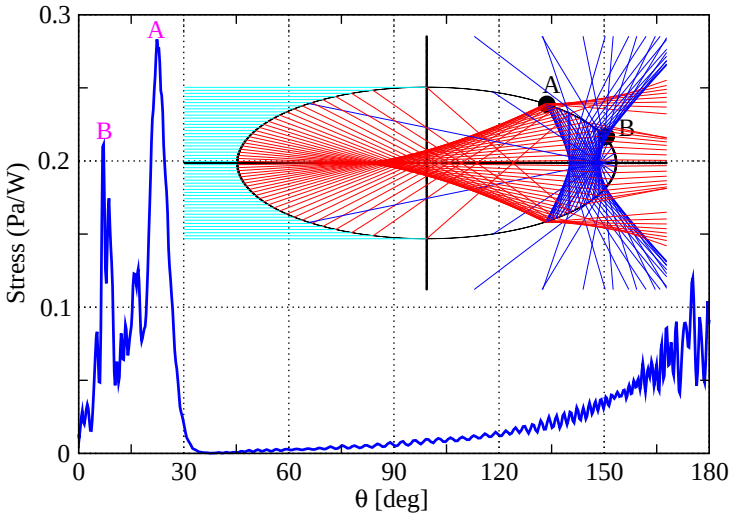

Figure 4.5: Stress profile on the surface of a prolate spheroid with aspect ratio $c/a = 5/2$ and ray tracing of orders $p = 1, 2$. The prolate spheroid has the same volume as a sphere of radius 8 μm. Other parameters are the same as those in Fig. 4.2.

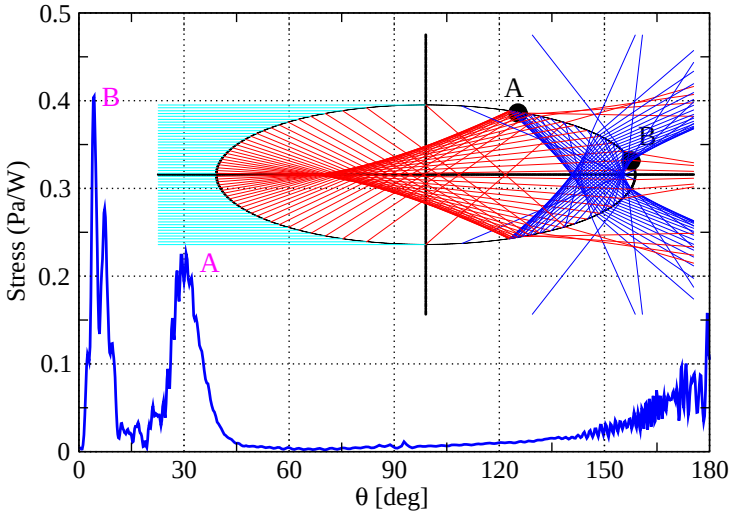

Figure 4.6: Stress profile on the surface of a prolate spheroid with aspect ratio $c/a = 3$ and ray tracing of orders $p = 1, 2$. Other parameters are the same as those in Fig. 4.2.

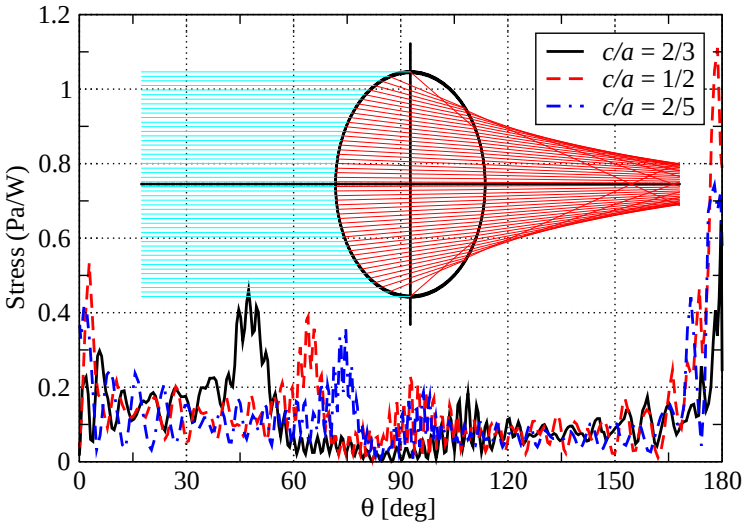

Figure 4.7: Stress profiles on the surface of oblate spheroids with different aspect ratios but the same volume as that of a sphere of radius 8 μm and ray tracing of order $p = 1$ when $c/a = 2/3$. Other parameters are the same as those in Fig. 4.2.

For oblate spheroid particles, the focusing effect is less important, therefore the variation of the stress profile as function of the aspect ration is not so significant. The stress profiles for aspect ratios $c/a = 2/3,\ 1/2,\ 2/5$ are plotted in Fig. 4.7. But we just show the ray tracing for the oblate of aspect ratio $c/a = 2/3$. We find that the stress profiles of the oblate with three aspect ratios are similar to each other. Each stress profile has three maxima, one in forward direction, one in the backward direction and the third one locates at the point where the rays of order $p = 1$ focus. With the increment of the aspect ratio, the third maximum point tends to $\theta = 90°$. Another important difference from the spherical or prolate spheroids is that the surface stress at $\theta = 180°$ can be very important due to the backward reflection.

From the above simple examples of a large incident beam along the symmetric axis of the spheroid, we see that the stress profile on the particle surface depends much the shape of the particle. The contributions of high orders rays can become important in certain cases.

When the incident beam makes angle β with the symmetric axis of the spheroid, the stress profile is no longer symmetric. We show in Fig. 4.8 the stress profiles when a prolate of aspect ratio $c/a = 2$ is illuminated by a large beam at three different angles. $\beta = 0°$ is the case we discussed in Fig. 4.4, the two symmetric maxima are located now in $\theta = 15°$ and $345°$. But when $\beta > 0°$, the optical stress profiles are no longer symmetric about the symmetric axis of the particle. With increment of the incident angle, the maximum stress points move to larger angles and the maximum value may be very important. For the cases $\beta = 15°$ and $30°$, in the small angle side the stress maximum points are well separated and located respectively at $\theta = 30°$ and $60°$. While the stress maximum points in large angle side vary little as function of incident angle. The maximum value of stress in small angle side is also much important than that in the other side. This can be explained by ray tracing shown in Fig. 4.8. The stress at point **A** in the small angle side is due to the first order rays and its value is more important than that at point **B** which is caused by the second order rays.

The stress profile for the same particle illuminated by the same beam as in Fig. 4.8 with observation plane in yz plane is shown in Fig. 4.9. The optical stress profiles are symmetric so only the profile between $0°$ and $180°$ is presented. When $\beta = 0°$ the maximum stress locates near $15°$ and its strength is much important than that in other two incidences.

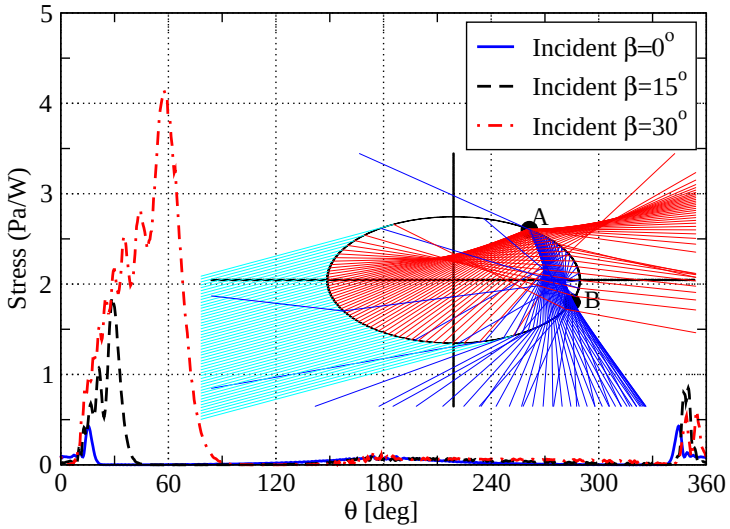

Figure 4.8: Stress profiles on the surface of a prolate spheroid with aspect ratio $c/a = 2$ but different incident angle β and ray tracing of orders $p = 1, 2$ when $\beta = 15°$. Other parameters are the same as those in Fig. 4.2.

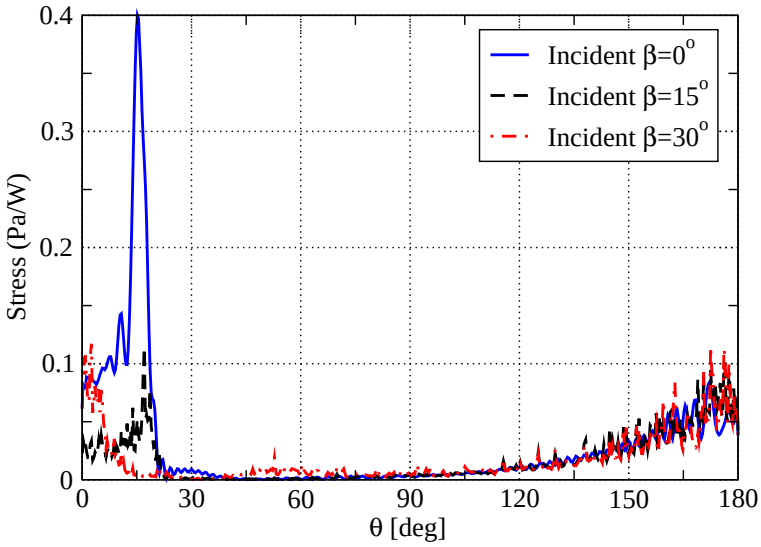

Figure 4.9: Stress profiles on the surface of a prolate spheroid with aspect ratio $c/a = 2$ and different incident angle β. The observation plane is in yz plane ($\phi = 90°$). Other parameters are the same as those in Fig. 4.8.

If the shape of the particle is complex, it is easy to imagine that the stress profile will be more complicated and difficult to calculate and analyze. To show the ability of our method to deal such problems, we choose the blood cells as example. Knowing the surface stress of such kind of particle can help to characterize the elasticity of cells. Consider a biconcave cell-like particle ($m = 1.41$) in water ($m = 1.33$) located at the center of a Gaussian beam of beam waist $w_0 = 100$ μm and wavelength $\lambda = 0.6328$ μm in vacuum. The stress profiles on the biconcave particle with the geometrical parameters ($q = 9$) in [145] and different beam incident direction β are shown in Fig. 4.10. Since this cell-like particle is very thin and it is embedded in water (so the relative refractive index is small), the stress on surface of the particle in xz plane is small and almost uniform in all direction for $\beta = 0°$. When $\beta = 45°$, because of its irregular shape, the maximum stress point does not locate in the forward or backward direction of the incident beam, but at $\theta = 285°$. When $\beta = 90°$, there are several peaks. The maximum stress locates at $\theta = 90°$, which is the forward direction of the incident beam. Also, unlike the spheroid particle, the stresses at the poles of the cell-like particle or in the sides of the incident beam ($\theta = 0°, 180°$) are relatively important.

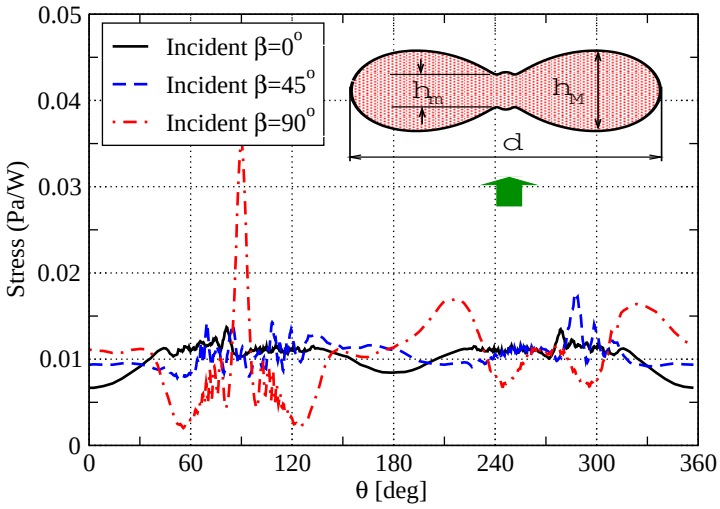

Figure 4.10: Stress profiles on a biconcave cell-like particle ($m = 1.4$) in water ($m = 1.33$) with different incident angle β. The waist radius of the Gaussian beam is $w_0 = 100$ μm with wavelength $\lambda = 0.6328$ μm in vacuum. The diameter of the cell-like particle is $d = 8.419$ μm (xy plane), the maximum and the minimum thickness are $h_M = 1.765$ μm and $h_m = 0.718$ μm.

We show also the stress profile in the plane yz, perpendicular to the plane defined by the symmetric axis of the particle and the propagation direction of the incident

beam. Because of the symmetry, only the profile between 0° and 180° is presented. We observe a peak in about 80° for $\beta = 0°$ and 45° and two maxima around 40° and 140° for $\beta = 45°$ and 90°. We note also the the amplitude of the stress at $\theta = 0°$ and 180° as those in Fig. 4.10 as they should be.

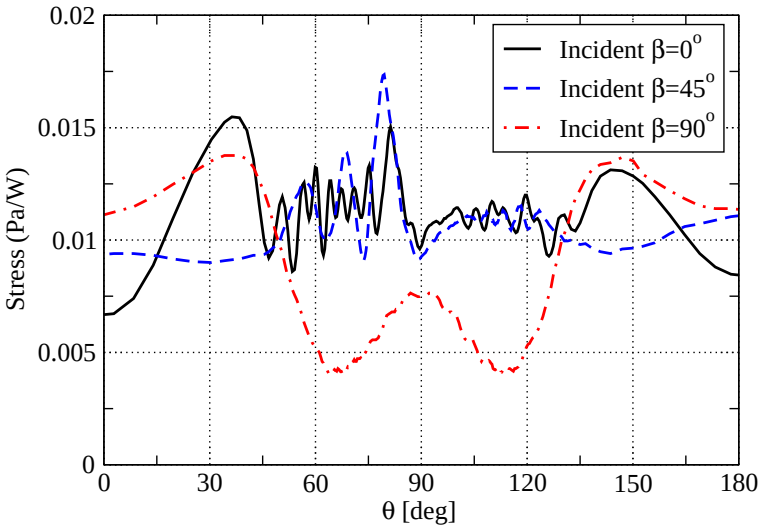

Figure 4.11: Stress profiles on the biconcave cell-like particle in water with different incident angle β. The observation plane is in yz plane ($\phi = 90°$). Other parameters are the same as those in Fig. 4.10.

4.2.2 Focused Gaussian beam incidence

When the Gaussian beam is highly focused, with a beam waist radius $w_0 = 2$ μm for example, the illumination intensity on the particle is strongly nonuniform. The classical ray model is stricto sensu no longer valid to describe the propagation of the beam nor to interpret its interaction with the particle. But it can still be used to give a qualitative analysis and to help check our calculation.

Again we start with a sphere. Fig. 4.12 shows the computed stress profile for a water droplet ($m = 1.33$) of radius $a = 8$ μm located at the center of the beam. The particle radius being much larger than that of the beam waist, the stress is dominated by the contribution of paraxial rays. Therefore, the two maxima are located on z axis one in forward direction and the other in backward directions. Then the stress decreases rapidly to zero with the angle θ. Since the beam waist radius is smaller than that in Fig. 4.2, the stress is stronger.

Then we compute the surface stresses on prolate spheroids and study the influence

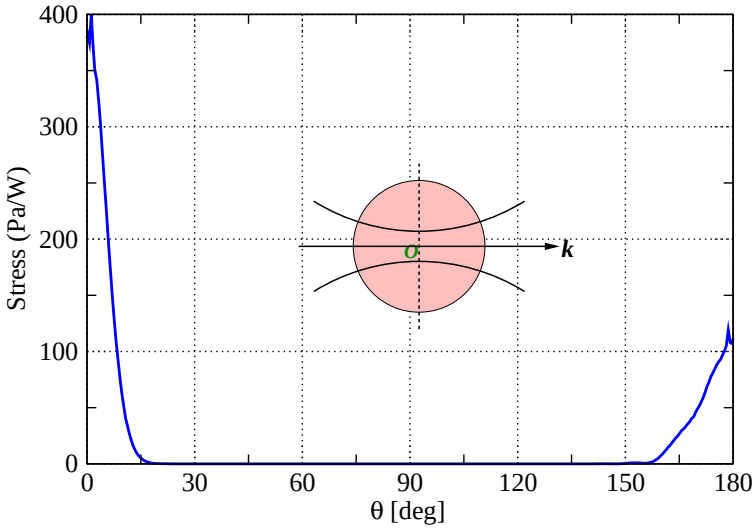

Figure 4.12: Stress profile on the surface of a spherical water droplet of radius 8 μm and refractive index $m = 1.33$ illuminated by a polarized (in the x direction at the waist) Gaussian beam of wavelength 0.785 μm and waist radius $w_0 = 2$ μm. The droplet center coincides with that of the beam. Plot of the stress in the xz plane.

of aspect ratios. The computed stresses for a spheroid of three aspect ratios $c/a = 3/2$, 2 and 5/2 are plotted in Fig. 4.13. Similar to the case of sphere, the surface stress on a prolate spheroid is also dominated by the contribution of the paraxial rays and the two zones of strong stress are located in forward and backward direction. We find also that the stress on the shadowed hemisphere decreases as function of the aspect ratio. This is because the curvature radius of the spheroid face to the incident beam decreases and the beam is more diverged by the particle. The fact that the maximum stress for aspect ratio $c/a = 5/2$ is located at 7° instead of 0° can be explained by the similar effect as point **B** in Fig. 4.5 using the ray tracing. It should note that the rays which contribute to the stress on point **A** in Fig. 4.5 come mainly from the incident rays relative far from the beam axis and their intensities are very weak in case of Fig. 4.13, so the peak at 23° disappears.

In the case of oblate spheroids illuminated by a tightly focused beam, the surface stress profiles for different aspect rations are similar to each other, as shown in Fig. 4.14. This is because the illuminated zone is relatively small and the surface curvature of the particle is also large. When the aspect ratio is sufficient small, the oblate spheroid is similar to a lame of parallel surfaces. There are only two stress peaks, one in the forward direction and the other in the backward direction and their profiles depend on the shape of the incident beam.

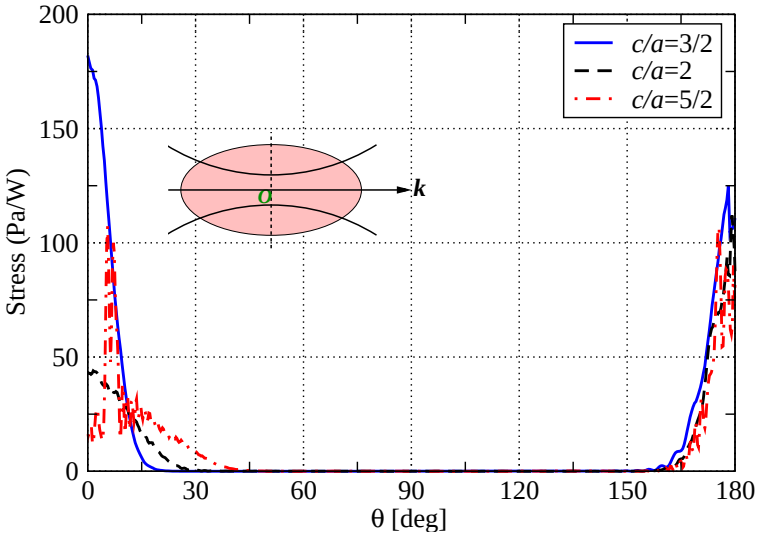

Figure 4.13: Stress profiles on the surface of prolate spheroids with different aspect ratios but the same volume as that of a sphere of radius 8 μm. Other parameters are the same as those in Fig. 4.12.

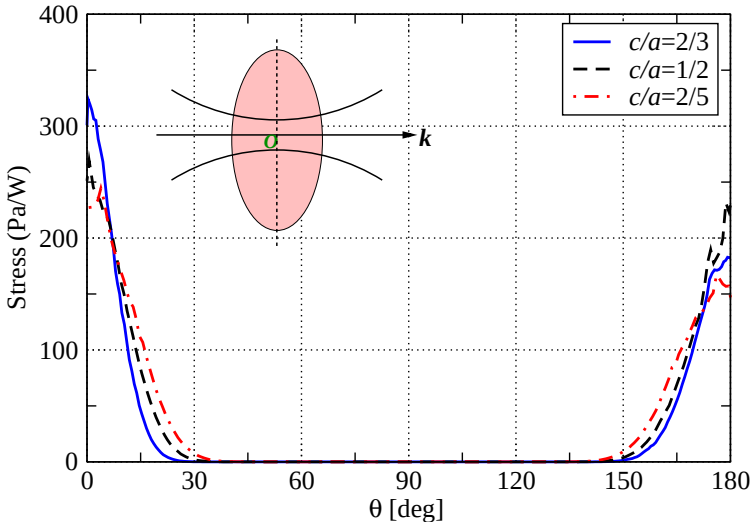

Figure 4.14: Stress profiles on the surface of oblate spheroids with different aspect ratios but the same volume as that of a sphere of radius 8 μm. Other parameters are the same as those in Fig. 4.12.

We show then, in Fig. 4.15, the optical stress on the surface of a long prolate spheroid ($c/a = 2$) illuminated by a tightly focused beam with three incident angles $\beta = 0°, 15°$ and $30°$. And we observed that the maximum value of the stress increases as function of the incident angle. This can be explained by the fact that, when $\beta = 0°$, the incident rays are so strongly focused on the first surface that they form a focal point in the particle and then largely diverged when they arrived on the second surface. If the incident angles $\beta = 15°$ or $30°$, the incident rays are converged to the second surface such that the intensity on the surface is relatively important, so does the stress. We find also that the points of the maximum stress in the forward direction are not exactly in the direction of the incident beam, $\theta = 30°$ and $50°$ respectively for $\beta = 15°$ and $30°$. This is due to the deviation of the rays in the particle.

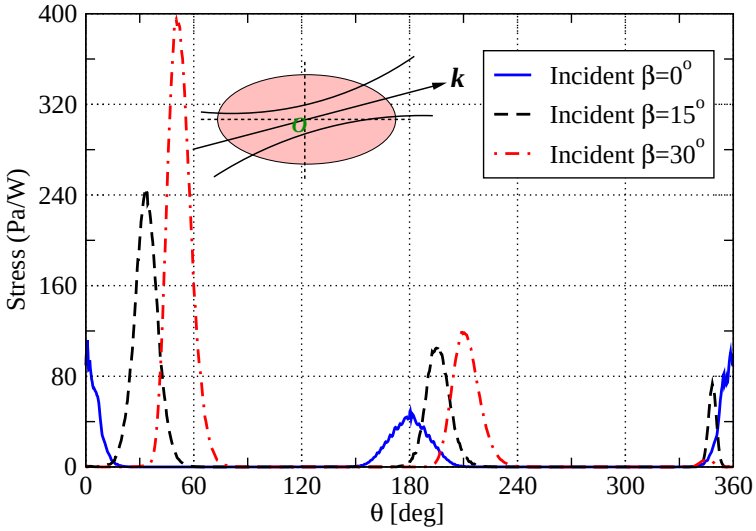

Figure 4.15: Stress profiles on the surface of a prolate spheroid with aspect ratios ($c/a = 2$) but different incident angle β. Other parameters are the same as those in Fig. 4.12.

When a particle is illuminated by a tightly focused beam, the distribution of the stress on the particle surface depends also on the beam position relative to the particle. Consider still a prolate spheroid of aspect ratio $c/a = 2$ with $a = 6.35$ μm and $c = 12.70$ μm so that its volume is the same as a sphere of radius $a = 8$ μm. The Gaussian beam ($w_0 = 2$ μm) propagates along the symmetric axis z of the particle with the center moving along x axis. We note the position of the beam center in the particle coordinate system by (x_0, y_0, z_0) and we will study three cases : $(0, 0, 0)$, $(-3w_0, 0, 0)$, and $(-4w_0, 0, 0)$, namely on axis, off axis inside the partible and off-axis outside of the particle. The computed stress profiles are shown in Fig. 4.16.

Unlike the profile for on axis case, the maximum stress points in the off axis cases are located in the forward direction at about $\theta = 15°$ due to the deviation of the rays in the particle and their peaks are narrow because of the focalization of the rays in the particle. The maximum stress points in the backward direction go to much larger angle positions and the peaks are much larger, this is due mainly to the shift of the incident beam (refer to the lower part of the particle in ray tracing Fig. 4.4). The ray tracing shows that, for the prolate spheroid, the incident rays at lower part of particle will focus at point **A**. Since when beam center locates at $(-4w_0, 0, 0)$, less number of rays with higher intensity incident into the particle and then focus near that point, optical stress on surface of the spheroid is smaller.

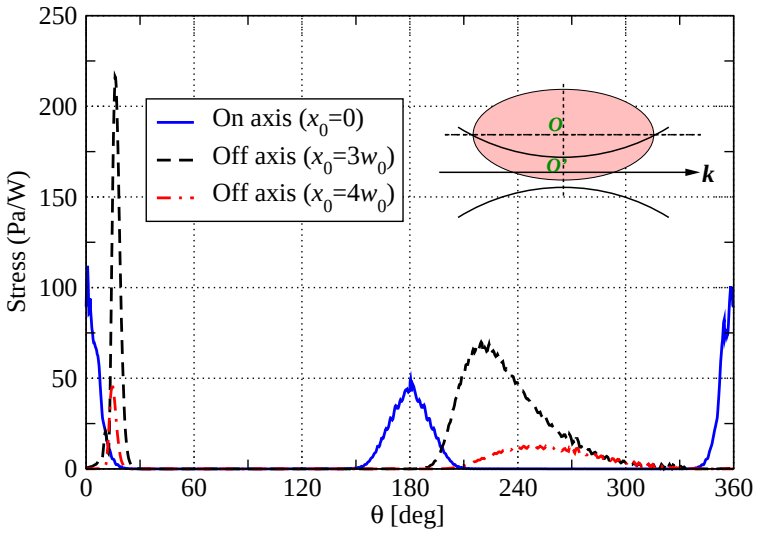

Figure 4.16: Stress profiles on the surface of prolate spheroid with aspect ratios $c/a = 2$. Other parameters are the same as those in Fig. 4.12. The beam has its center (x_0, y_0, z_0) located at $(0, 0, 0)$, $(3w_0, 0, 0)$, and $(4w_0, 0, 0)$, respectively.

Then we apply our method to study the radiation stress on the surface of a cell-like particle when it is illuminated by a focused Gaussian beam. We take the same particle as in Fig. 4.10 and a beam of waist radius $w_0 = 2$ μm illuminating the particle with different angle β. The computed stress profiles in the incident xz plane are shown in Fig. 4.17. Since the beam is highly focused, when $\beta = 0°$, like those for oblate spheroids, the stress maxima are located at the forward and backward directions of the incident beam. The stress near the poles ($\theta = 90°$, $270°$) are almost zero. The stress profile for $\beta = 45°$ is similar to that for $\beta = 0°$, but it is shifted to the large angles. When $\beta = 90°$, the the stress profile is very different, apart from the maxima in the two region around $\theta = 0°$ and $180°$, two maxima appear in the backward and

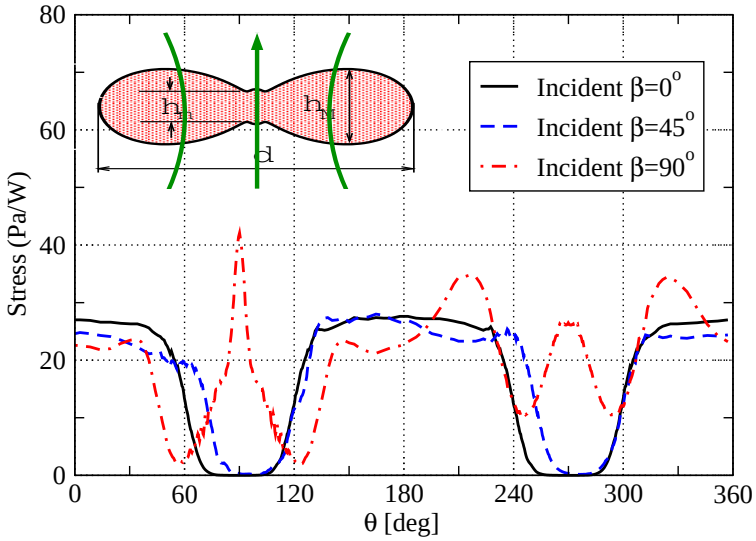

Figure 4.17: Stress profiles on a biconcave cell-like particle ($m = 1.4$) in water ($m = 1.33$) with different incident angle β. The waist radius of the Gaussian beam is $w_0 = 2$ μm with wavelength $\lambda = 0.6328$ μm in vacuum.

forward direction of the incident beam $\theta = 90°,\ 270°$. It is clear that stress profiles for the biconcave particle is more complex than for spherical or spheroidal particle since its structure is irregular.

At last, to show great capability of our present method for the numerical prediction of radiation stress on the surface of a very large prolate spheroidal water droplet ($m = 1.33$) with aspect ratio $c/a = 2$ and the same volume as that of a sphere of radius 50 μm is computed. Its semi-major and semi-minor axis are 79.37 μm and 39.69 μm respectively. The beam waist of the incident Gaussian beam of wavelength 0.785 μm is set to $w_0 = 50$ μm. The incident angle is 15° relative to the symmetrical axis of the particle. For this calculation, the whole surface of the prolate spheroid is discretized into 12 million triangle patches with total 34 million unknowns. The computed stress profile is shown in Fig. 4.18. This calculation takes about 250 GB memory and 22 hour CPU time with 50 MPI processes and 2 threads for each process.

4.3 Conclusions

In this Chapter, optical stress on the surface of homogeneous particles is computed and analyzed by using the MLFMA enhanced SIE method. This numerical method is of high accuracy and great capability for large and arbitrary shaped homogeneous

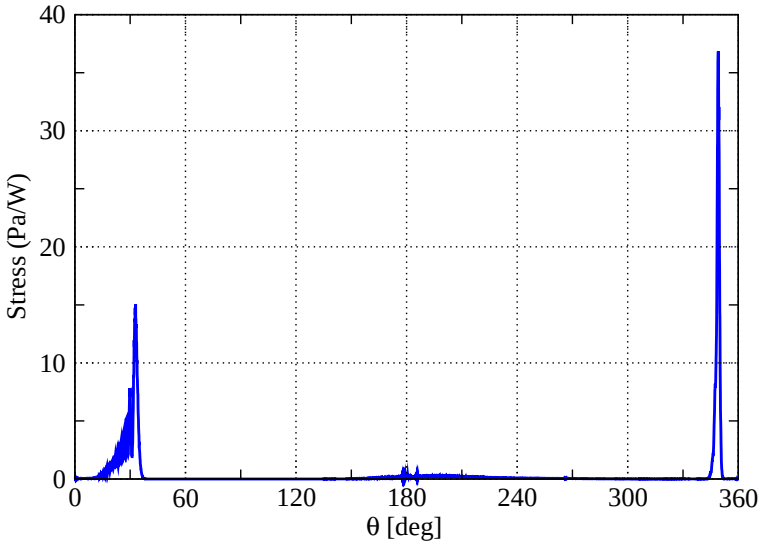

Figure 4.18: Stress profile on the surface of a prolate spheroid ($m = 1.33$) with aspect ratio $c/a = 2$. The prolate spheroid has the same volume as a sphere of radius 50 μm. The wavelength of the incident beam is 0.785 μm and its beam waist $w_0 = 50$ μm.

particles. In the special case of homogeneous sphere illuminated by a Gaussian beam, its results are in good agreement with the generalized Lorentz-Mie theory (GLMT) in [152]. The stress profiles on surface of prolate and oblate spheroids with different aspect ratios are presented. The influences of the aspect ratio as well as the beam waist size and the incident condition are analyzed. Our recently developed ray tracing model is employed to give a physical interpreting of the characteristics of stress and also permit to check the results. We found that the characteristics of stress on prolate spheroids are mainly determined by the rays of low order ($p = 0,\ 1$), but sometime the higher ($p \geq 2$) may play an important role at certain points on the surface depending on both the shape of the particle and the beam as well as their relative position. The stress on surface of a biconcave cell-like particle is also studied, showing that this method can be applied to soft particles of arbitrary shape. Our algorithm can go even far in the size of the particle, for a prolate spheroid of size parameter equal to 640 (volume-equivalent size parameter 400) for instance. Although, we have only presented the surface stress in certain observation planes, the stress at any point of the particle surface is available. The presentation of the stress profiles in 3D is feasible.

Chapter 5

Conclusions and Perspectives

This PhD thesis is devoted to fast computation and analysis of light interactions of large non-spherical particles, with the Vectorial Complex Ray Model (VCRM) and the MultiLevel Fast Multipole Algorithm (MLFMA) enhanced combined tangential formulation (CTF) of the surface integral equation (SIE) method. The incident wave can be a plane wave or arbitrary shaped beam. In this chapter we draw the conclusions of presented work and give perspectives for further studies.

5.1 Conclusions

In various research domains such as the environmental control, the fluid mechanics, the combustion, the micro fluidics and telecommunication, the light scattering theories play an important role. Computation of the scattering properties of particles of very simple shapes, such as sphere and infinite circular cylinder, are well mastered and excessively applied in many fields. But, the shapes of the particles encountered in nature, in industry and in laboratories are often irregular and of complex shape, and their sizes are often larger compared to the wavelength of incident light waves.

Various theoretical and numerical methods have been developed for non-spherical particle, such as spheroid, ellipsoid, or elliptical cylinder to take into account the shape of the particles. However, the sizes of the particles or shapes of the particles are often limited because of the numerical difficulty.

The Vectorial Complex Ray Model (VCRM) recently developed by Ren *et al.* permits to deal with the scattering of large irregularly shaped particles. In VCRM, a

wavefront curvature is introduced as an new intrinsic properties of the rays to describe the divergence/convergnece of the wave. By doing so, the phase shift due to the focal line can also be counted easily. VCRM is proved to achieve good agreement with the rigorous LMT theories. Recently, it is further applied for solving scattering by plane wave or Gaussian beams incident on large ellipsoids and infinite elliptical cylinders. But its results for large non-spherical are to be validated and its precision is to be evaluated.

The full wave numerical method named the combined tangential formulation (CTF) of the surface integral equation method (SIE) was therefore chosen to compute the scattering properties of large non-spherical particles for its high accuracy and high performance. To reduce its computation resource requirement and to strength its capability, the multilevel fast multipole algorithm (MLFMA) is employed to speed up matrix vector multiplication in iterative solution steps of the final matrix equation system. This CTF with MLFMA is efficiently paralleled on a distributed memory super computer platform with hybrid MPI-OpenMP parallelization approach. With this improvement, the calculable size parameter of the particle can be more than 600.

After a brief recall of the fundamental models and concepts in light scattering, the general principles of the VRCM and CTF with MLFMA are presented. By comparing the scattering diagrams of a large sphere with rigorous theory, we have shown that the precision of both VCRM and MLFMA is very good for sphere with radius of several tens of wavelengths. Since we have no rigorous result as a benchmark for the scattering of large elliptical particles, the scattered intensities have also been compared to the results of the code ADDA to validate our MLFMA code. The scattering diagrams as function of the incident angle and the aspect ratios of the ellipsoids have also been studied with MLFMA and VCRM. Numerical results proved that VCRM can predict with precision the light scattering of a sphere, prolate or oblate spheroids and ellipsoids of size as small as some tens of wavelengths. The effects of size parameter and aspect ratios of the ellipsoid particles and the influences of incident angles for a Chebychev dust particle have also been examined. The calculation for a Chebychev particle of size parameter up to 628 demonstrates the great capacity of CTF with MLFMA.

Then CTF with MLFMA is used for the calculation study of the radiation pressure force (RPF) and torque exerted by a shaped light beam on arbitrary shaped homogenous particles. Usually, In the classical numerical methods, the RPF and torque are often computed by vector flux of the Maxwell's stress tensor/pseudotensor

over a surface enclosing the particle. To be convenient, this surface is chosen to be far away from the particle so that asymptotic forms of special functions can be applied. However, for a shaped beam, such as Gaussian beam, it is hard or even impossible to get the mathematical description of the electromagnetic fields which satisfy rigorously the Maxwell's equations in all space. Here we use a spherical surface tightly enclosing the particle to avoid inaccuracy caused by description of the incident electromagnetic fields. Since any point on this spherical surface locates in near field region, the analytical electromagnetic field expression can be used. We choose Gaussian beam as an example and give in detail the frame of using CTF with MLFMA for computing RPF/Toqure on arbitrary shaped particles. Other shaped beams can be done in the same way without any difficulties. Numerical results on spherical and small spheroidal particle are compared with the Generalized Lorenz-Mie theory (GLMT) and good agreements are observed. The RPF and torque on a relatively large spheroid and a complex shaped biconcave red blood cell are also computed. We observed a negative pulling force when the incident wavelength is set to 0.5145μm while a normal pushing force when it is set to 1.0640μm

Prediction of the stress on the surface of an arbitrarily shaped particle of soft material is essential in the study of elastic properties of the particles with optical force. It is also necessary in the manipulation and sorting of small particles with optical tweezers, since a regular shape particles, such as sphere, may be deformed under the non-uniform optical stress on its surface. The stress profile on a spherical or small spheroidal particle trapped by shaped beams has been reported. But little work on the computation of the surface stress of an irregular large non-spherical particle has been reported. We apply the CTF with MLFMA to compute the surface stress on homogeneous arbitrarily shaped particles. The comparison of the computed stress profile with that predicted by the generalized Lorenz-Mie theory (GLMT) for a water droplet of diameter equal to 51 wavelengths in a focused Gaussian beam show that the precision of our method is in very good agreement. Then the stress profiles on spheroids with different aspect ratios are computed. The particles are illuminated by Gaussian beam of different waist radii at different incidences. Physical analysis on mechanism of optical stress is given with help of VCRM. We found the maximum of stress profile on the surface of prolate spheroids is not only determined by the reflected and refracted rays (orders $p = 0,\ 1$) but also the rays undergone one or two internal reflection where they focus. Computational study of stress on surface of a biconcave cell-like particle, which is a typical application in life science, is also undertaken.

5.2 Perspectives

The two initial objectives of this thesis have been achieved: numerical validation of VCRM by comparing the scattering diagrams computed by MLFMA and application of the new developed MLFMA algorithm to the computation of the radiation force, torque and stress exerted by a laser beam on a large non-spherical particle. Some tools developed in this thesis can be used directly for other applications and some are to be improved or extended to larger domains. As the work directly related to this thesis, the following points are to be developed.

Amount of numerical results on the scattering of large non-spherical particles are provided in the thesis: scattering diagrams, scattering matrix, radiation pressure forces, torques and stress. These results are useful in the optical metrology, the particle manipulation and the study of the dynamics of non-spherical in laser beams. The developed code can also be applied to calculated those physical quantities with other parameters. All these numerical results are to be validated by experiment.

By taking into account correctly the wave curvature, VCRM can be applied to predict all the scattering properties of large particles with smooth surface and arbitrary shape. But so far it is only applied to the 2D scattering (scattering in a plane of symmetry) of ellipsoidal particles and elliptical infinite cylinders. The extension of VCRM to 3D scattering of particles such as spheroid and infinite elliptical cylinder should be direct and remain to do. This will permit to enlarge very much the application domain of the model, since this is a necessary step for the calculation of the radiation pressure force, torque and stress exerted by a laser beam on a particle, as well as its scattering, absorption and extinction coefficients. The wave front being a intrinsic property in VCRM, it is also direct to include the shape of incident beam in VCRM. Once the 3D code of VCRM is available, the extension to other shaped particles will be simple. To improve further the accuracy of VCRM the diffraction effect is to be considered near the singularity regions (in the rainbow angles, the critic angles and the forward directions).

The code of MLFMA developed in the thesis is directly applicable to homogeneous particles of any shape and any shaped light beams, so it can be used directly to validate the calculation of the scattering in 3D of VCRM, and to compute the scattering properties (scattering matrix, cross sections, RPF, torque and tress etc.) of other non-spherical particle and/or illuminated by other shaped beams, i.e. the Bessel beam and higher order Hermite-Gaussian beam. This work is very straightforward

and can be easily done, since the framework has been already drawn.

The SIE with MLFMA is proved very powerful, but the code developed and the computations in the manuscript concern only homogeneous isotropic particles. However, in practice, we also need to solve light interaction with inhomogeneous and/or anisotropic particles. The SIE with MLFMA is not suitable for such problems. To study radiation pressure force on such kind of particles, another MLFMA based numerical method named the hybrid finite element-boundary integral-multilevel fast multipole algorithm (FE-BI-MLFMA) can be employed. In FE-BI-MLFMA, the finite element method (FEM) is used to model complex and inhomogeneous properties of the particle. Then the boundary integral equation method (BIE) is used as a truncation of the FEM region. Hence it is general, efficient and accurate, and can be applied to arbitrary shaped, anisotropy and inhomogeneous particles. Like the DDA and FDTD, the calculable size of the particle by this method is small. To strength its capability, we have presented an efficient parallel domain-decomposition based algorithm of hybrid FE-BI-MLFMA method (DDM-FE-BI-MLFMA) [157]. In future, this DDM-FE-BI-MLFMA can be applied for computing RPF and torque on large inhomogeneous particles.

Bibliography

[1] H. C. Van De Hulst. Light scattering by small particles. Courier Dover Publications, 1957.

[2] C. F. Bohren and D. R. Huffman. Absorption and scattering of light by small particles. John Wiley & Sons, 2008.

[3] J. S. Kim and S. S. Lee. Scattering of laser beams and the optical potential well for a homogeneous sphere. J. Opt. Soc. Am., 73(3):303–312, 1983.

[4] J. P. Barton, D. R. Alexander, and S. A. Schaub. Internal and near-surface electromagnetic fields for a spherical particle irradiated by a focused laser beam. J. Appl. Phys., 64(4):1632–1639, 1988.

[5] G. Gouesbet, B. Maheu, and G. Gréhan. Light scattering from a sphere arbitrarily located in a Gaussian beam, using a Bromwich formulation. J. Opt. Soc. Am. A, 5(9):1427–1443, 1988.

[6] G. Gouesbet, G. Gréhan, and B. Maheu. Localized interpretation to compute all the coefficients g_m^m in the generalized Lorenz-Mie theory. J. Opt. Soc. Am. A, 7(6):998–1007, 1990.

[7] K. F. Ren, G. Gouesbet, and G. Gréhan. The integral localized approximation in generalized Lorenz-Mie theory. Appl. Opt., 37(19):4218–4225, 1998.

[8] J. A. Lock. Calculation of the radiation trapping force for laser tweezers by use of generalized Lorenz-Mie theory. I. Localized model description of an on-axis tightly focused laser beam with spherical aberration. Appl. Opt., 43(12):2532–2544, 2004.

[9] J. A. Lock. Calculation of the radiation trapping force for laser tweezers by use of generalized Lorenz-Mie theory. II. On-Axis Trapping Force. Appl. Opt., 43(12):2545–2554, 2004.

[10] F. Onofri, G. Gréhan, and G. Gouesbet. Electromagnetic scattering from a multilayered sphere located in an arbitrary beam. Appl. Opt., 34(30):7113–7124, 1995.

[11] Y. P. Han and Z. S. Wu. Scattering of a spheroidal particle illuminated by a gaussian beam. Appl. Opt., 40(15):2501–2509, 2001.

[12] F. Xu, K. F. Ren, G. Gouesbet, X. Cai, and G. Gréhan. Theoretical prediction of radiation pressure force exerted on a spheroid by an arbitrarily shaped beam. Phys. Rev. E, 75(2):026613, 2007.

[13] K. F. Ren, G. Gréhan, and G. Gouesbet. Scattering of a gaussian beam by an infinite cylinder in the framework of generalized lorenz–mie theory: formulation and numerical results. J. Opt. Soc. Am. A, 14(11):3014–3025, 1997.

[14] J. A. Lock. Scattering of a diagonally incident focused gaussian beam by an infinitely long homogeneous circular cylinder. J. Opt. Soc. Am. A, 14(3):640–652, 1997.

[15] G. Gouesbet, L. Mees, G. Gréhan, and K. F. Ren. Localized approximation for Gaussian beams in elliptical cylinder coordinates. Appl. Opt., 39(6):1008–1025, 2000.

[16] G. Gouesbet and G. Gréhan. Generalized lorenz-mie theory for a sphere with an eccentrically located spherical inclusion. J. Mod. Optic., 47(5):821–837, 2000.

[17] G. Gouesbet and G. Gréhan. Generalized lorenz-mie theory for assemblies of spheres and aggregates. J. Opt. A:Pure Appl. Opt., 1(6):706, 1999.

[18] J. W. Strutt. XV. On the light from the sky, its polarization and colour. The London, Edinburgh, and Dublin Philosophical Magazine and Journal of Science, 41(271):107–120, 1871.

[19] P. Yang and K. N. Liou. Geometric-optics-integral-equation method for light scattering by nonspherical ice crystals. Appl. Opt., 35(33):6568–6584, 1996.

[20] Z. B. Zhang, P. Yang, G. W. Kattawar, and W. J. Wiscombe. Single-scattering properties of platonic solids in geometrical-optics regime. J. Quant. Spectrosc. Radiat. Transf., 106(1):595–603, 2007.

[21] P. Yang and K. N. Liou. An exact geometric-optics approach for computing the optical properties of large absorbing particles. J. Quant. Spectrosc. Radiat. Transf., 110(13):1162–1177, 2009.

[22] K. F. Ren, F. Onofri, C. Rozé, and T. Girasole. Vectorial complex ray model and application to two-dimensional scattering of plane wave by a spheroidal particle. Opt. Lett., 36(3):370–372, 2011.

[23] P. C. Waterman. Matrix formulation of electromagnetic scattering. Proc. IEEE, 53(8):805–812, 1965.

[24] P. C. Waterman. Symmetry, unitarity and geometry in electromagnetic scattering. Phys. Rev. D, 3(4):825, 1971.

[25] M. I. Mishchenko, L. D. Travis, and D. W. Mackowski. T-matrix computations of light scattering by nonspherical particles: A review. J. Quant. Spectrosc. Radiat. Transf., 55(5):535–575, 1996.

[26] M. I. Mishchenko, L. D. Travis, and A. A. Lacis. Scattering, Absorption and Emission of Light by Small Particles. Cambridge U. Press, 2002.

[27] T. Wriedt. Using the T-matrix method for light scattering computations by non-axisymmetric particles: Superellipsoids and realistically shaped particles. Particle & Particle Systems Characterization, 19(4):256–268, 2002.

[28] L. Bi, P. Yang, G. W. Kattawar, and M. I. Mishchenko. Efficient implementation of the invariant imbedding T-matrix method and the separation of variables method applied to large nonspherical inhomogeneous particles. J. Quant. Spectrosc. Radiat. Transf., 116:169–183, 2013.

[29] L. Bi, P. Yang, G. W. Kattawar, and M. I. Mishchenko. A numerical combination of extended boundary condition method and invariant imbedding method applied to light scattering by large spheroids and cylinders. J. Quant. Spectrosc. Radiat. Transf., 123:17–22, 2013.

[30] K. Yee. Numerical solution of initial boundary value problems involving Maxwell's equations in isotropic media. IEEE Trans. Antennas Propagat., 14(3):302–307, 1966.

[31] P. Yang and K. N. Liou. Finite-difference time domain method for light scattering by small ice crystals in three-dimensional space. J. Opt. Soc. Am. A, 13(10):2072–2085, 1996.

[32] W. B. Sun, Q. Fu, and Z. Z. Chen. Finite-difference time-domain solution of light scattering by dielectric particles with a perfectly matched layer absorbing boundary condition. Appl. Opt., 38(15):3141–3151, 1999.

[33] R. S. Brock, X. H. Hu, P. Yang, and J. Lu. Evaluation of a parallel FDTD code and application to modeling of light scattering by deformed red blood cells. Opt. Express, 13(14):5279–5292, 2005.

[34] G. Mur. Absorbing boundary conditions for the finite-difference approximation of the time-domain electromagnetic-field equations. IEEE Trans. Electromagn. Compat., 23(4):377–382, 1981.

[35] J. P. Berenger. A perfectly matched layer for the absorption of electromagnetic waves. J. Comput. Phys., 114(2):185–200, 1994.

[36] P. R. Amestoy, I. S. Duff, J. Koster, and J. Y. L'Excellent. A fully asynchronous multifrontal solver using distributed dynamic scheduling. SIAM J. Matrix Anal. A., 23(1):15–41, 2001.

[37] C. Farhat and F. X. Roux. A method of finite element tearing and interconnecting and its parallel solution algorithm. Int. J. Numer. Method Eng., 32(6):1205–1227, 1991.

[38] J. M. Jin Y. J. Li. A new dual-primal domain decomposition approach for finite element simulation of 3-D large-scale electromagnetic problem. IEEE Trans. Antennas Propagat., 55(10):2803–2810, 2007.

[39] Roger F Harrington and Jan L Harrington. Field computation by moment methods. Oxford University Press, 1996.

[40] E. M. Purcell and C. R. Pennypacker. Scattering and absorption of light by nonspherical dielectric grains. Astrophys. J., 186:705–714, 1973.

[41] A. G. Hoekstra and P. M. A. Sloot. New computational techniques to simulate light-scattering from arbitrary particles. Part. Part. Sys. Charact., 11(3):189–193, 1994.

[42] B. T. Draine and P. J. Flatau. Discrete-dipole approximation for scattering calculations. J. Opt. Soc. Am. A, 11(4):1491–1499, 1994.

[43] A. G. Hoekstra, M. D. Grimminck, and P. M. A. Sloot. Large scale simulations of elastic light scattering by a fast discrete dipole approximation. Int. J. Mod. Phys. C, 9(01):87–102, 1998.

[44] M. A. Yurkin and A. G. Hoekstraa. The discrete dipole approximation: An overview and recent developments. J. Quant. Spectrosc. Radiat. Transf., 106(1-3):558–589, 2007.

[45] J. J. Goodman, B. T. Draine, and P. J. Flatau. Application of fast-fourier-transform techniques to the discrete-dipole approximation. Opt. Lett., 16(15):1198–1200, 1991.

[46] R. F. Harrington. Boundary integral formulations for homogeneous material bodies. J. Electromagn. Waves Applicat., 3(1):1–15, 1989.

[47] L. Gürel, H. Bagci, J. C. Castelli, A. Cheraly, and F. Tardivel. Validation through comparison: Measurement and calculation of the bistatic radar cross section (BRCS) of a stealth target. Radio Sci., 38(3):2803–2810, 2003.

[48] J. M. Taboada, J. Rivero, F. Obelleiro, M. G. Araujo, and L. Landesa. Method-of-moments formulation for the analysis of plasmonic nano-optical antennas. J. Opt. Soc. Am. A, 28(7):1341–1348, 2011.

[49] X. Q. Sheng, J. M. Jin, J. M. Song, W. C. Chew, and C. C. Lu. Solution of combined-field integral equation using multilevel fast multipole algorithm for scattering by homogeneous bodies. IEEE Trans. Antennas Propagat., 46(11):1718–1726, 1998.

[50] P. Yla-Oijala and M. Taskinen. Application of combined field integral equation for electromagnetic scattering by dielectric and composite objects. IEEE Trans. Antennas Propagat., 53(3):1168–1173, 2005.

[51] S. M. Rao, D. R. Wilton, and A. W. Glisson. Electromagnetic scattering by surfaces of arbitrary shape. IEEE Trans. Antennas Propagat., 30(3):409–418, 1982.

[52] J. M. Song and W. C. Chew. Multilevel fast multipole algorithm for solving combined field integral equations of electromagnetic scattering. Micro. Opt. Tech. Let., 10(1):14–19, 1995.

[53] E. Bleszynski, M. Bleszynski, and T. Jaroszewicz. AIM: Adaptive integral method for solving large-scale electromagnetic scattering and radiation problems. Radio Sci., 31(5):1225–1251, 1996.

[54] J. M. Song, C. C. Lu, and W. C. Chew. Multilevel fast multipole algorithm for electromagnetic scattering by large complex objects. IEEE Trans. Antennas Propagat., 45(10):1488–1493, 1997.

[55] S. Velamparambil, W. C. Chew, and J. Song. 10 million unknowns: Is it that big. IEEE Antennas Propagat. Mag., 45(2):43–58, 2003.

[56] L. Gürel and Ö. Ergül. Fast and accurate solutions of extremely large integral-equation formulations discretised with tens of millions of unknowns. Electron. Lett., 43(9):499–500, 2007.

[57] X. M. Pan and X. Q. Sheng. A sophisticated parallel MLFMA for scattering by extremely large targets. IEEE Antennas Propag. Mag., 50(3):129–138, 2008.

[58] X. M. Pan, W. C. Pi, M. L. Yang, Z. Peng, and X. Q. Sheng. Solving problems with over one billion unknowns by the MLFMA. IEEE Trans. Antennas Propagat., 60(5):2571–2574, 2012.

[59] G. Roosen and C. Imbert. Optical levitation by means of two horizontal laser beams: a theoretical and experimental study. Phys. Lett. A, 59(1):6–8, 1976.

[60] A. Ashkin. Acceleration and trapping of particles by radiation pressure. Phys. Rev. Lett., 24(4):156, 1970.

[61] A. Ashkin, J. M. Dziedzic, J. E. Bjorkholm, and S. Chu. Observation of a single-beam gradient force optical trap for dielectric particles. Opt. Lett., 11(5):288–290, 1986.

[62] J. Guck, R. Ananthakrishnan, T. J. Moon, C. C. Cunningham, and J. Kas. Optical deformability of soft biological dielectrics. Phys. Rev. Lett., 84(23):5451, 2000.

[63] J. Guck, R. Ananthakrishnan, H. Mahmood, T. J. Moon, C. C. Cunningham, and J. Kas. The optical stretcher: a novel laser tool to micromanipulate cells. Biophys. J., 81(2):767–784, 2001.

[64] M. Dao, C.T. Lim, and S. Suresh. Mechanics of the human red blood cell deformed by optical tweezers. J. Mech. Phys. Solids, 51(11):2259–2280, 2003.

[65] J. R. Moffitt, Y. R. Chemla, S. B. Smith, and C. Bustamante. Recent advances in optical tweezers. Annu. Rev. Biochem., 77(1):205, 2008.

[66] M. P. MacDonald, G. C. Spalding, and K. Dholakia. Microfluidic sorting in an optical lattice. Nature, 426(6965):421–424, 2003.

[67] W. H. Teh, U. Durig, G. Salis, R. Harbers, U. Drechsler, C. G. Smith, R. E. Mahrt, and H. J. Guntherodt. SU-8 for real three-dimensional subdiffraction-limit two-photon microfabrication. Appl. Phys. Lett., 84(20):4095–4097, 2004.

[68] P. Galajda and P. Ormos. Complex micromachines produced and driven by light. Appl. Phys. Lett., 78(2):249–251, 2001.

[69] M. E. J. Friese and H. Rubinsztein-Dunlop. Optically driven micromachine elements. Appl. Phys. Lett., 78(4):547–549, 2001.

[70] K. F. Ren, G. Grehan, and G. Gouesbet. Radiation pressure forces exerted on a particle arbitrarily located in a Gaussian beam by using the generalized Lorenz-Mie theory, and associated resonance effects. Opt. Commun, 108(4-6):343–354, 1994.

[71] K. F. Ren, G. Grehan, and G. Gouesbet. Prediction of reverse radiation pressure by generalized Lorenz-Mie theory. Appl. Opt., 35(15):2702–2710, 1996.

[72] H. Polaert, G. Gréhan, and G. Gouesbet. Improved standard beams with application to reverse radiation pressure. Appl. Opt., 37(12):2435–2440, 1998.

[73] H. Polaert, G. Gréhan, and G. Gouesbet. Forces and torques exerted on a multilayered spherical particle by a focused Gaussian beam. Opt. Commun., 155(1-3):169–179, 1998.

[74] V. V. Kotlyar and A. G. Nalimov. Analytical expression for radiation forces on a dielectric cylinder illuminated by a cylindrical Gaussian beam. Opt. Express, 14(13):6316–6321, 2006.

[75] F. Xu, J. A. Lock, G. Gouesbet, and C. Tropea. Radiation torque exerted on a spheroid: Analytical solution. Phys. Rev. A, 78(1):013843, 2008.

[76] A. Ashkin. Forces of a single-beam gradient laser trap on a dielectric sphere in the ray optics regime. Biophys. J., 61(2):569–582, 1992.

[77] C. B. Chang, W. X. Huang, K. H. Lee, and H. J. Sung. Optical levitation of a non-spherical particle in a loosely focused gaussian beam. Opt. Express, 20(21):24068–24084, 2012.

[78] B. M. Mihiretie, P. Snabre, J. C. Loudet, and B. Pouligny. Radiation pressure makes ellipsoidal particles tumble. Europhys. Lett., 100(4):48005, 2012.

[79] T. A. Nieminen, H. Rubinsztein-Dunlop, N. R. Heckenberg, and A. I. Bishop. Numerical modelling of optical trapping. Comput. Phys. Commun., 142(1):468–471, 2001.

[80] T. A. Nieminen, H. Rubinsztein-Dunlop, and N. R. Heckenberg. Calculation and optical measurement of laser trapping forces on non-spherical particles. J. Quant. Spectrosc. Radiat. Transf., 70(4):627–637, 2001.

[81] T. A. Nieminen, H. Rubinsztein-Dunlop, and N. R. Heckenberg. Multipole expansion of strongly focussed laser beams. J. Quant. Spectrosc. Radiat. Transf., 79:1005–1017, 2003.

[82] S. H. Simpson and S. Hanna. Numerical calculation of interparticle forces rising in association with holographic assembly. J. Opt. Soc. Am. A, 23(6):1419–1431, 2006.

[83] S. H. Simpson and S. Hanna. Optical trapping of spheroidal particles in Gaussian beams. J. Opt. Soc. Am. A, 24(2):430–443, 2007.

[84] S. H. Simpson and S. Hanna. Rotation of absorbing spheres in LaguerrecGaussian beams. J. Opt. Soc. Am. A, 26(1):173–183, 2009.

[85] F. Borghese, P. Denti, R. Saija, and M. A. Iati. Optical trapping of nonspherical particles in the T-matrix formalism. Opt. Express, 15(19):11984–11998, 2007.

[86] B. T. Draine. The discrete-dipole approximation and its application to interstellar graphite grains. Astrophys. J., 333:848–872, 1988.

[87] B. T. Draine and J. C. Weingartner. Radiative torques on interstellar grains I. superthermal spin-up. Astrophys. J., 470:551, 1996.

[88] B. T. Draine and J. C. Weingartner. Radiative torques on interstellar grains II. grain alignment. Astrophys. J., 480(2):633, 1997.

[89] J. C. Weingartner and B. T. Draine. Radiative torques on interstellar grains III. dynamics with thermal relaxation. Astrophys. J., 589(1):289, 2003.

[90] H. Kimura and I. Mann. Radiation pressure cross section for fluffy aggregates. J. Quant. Spectrosc. Radiat. Transf., 60(3):425–438, 1998.

[91] A. G. Hoekstra, M. Frijlink, L. B. F. M. Waters, and P. M. A. Sloot. Radiation forces in the discrete-dipole approximation. J. Opt. Soc. Am. A, 18(8):1944–1953, 2001.

[92] D. Bonessi, K. Bonin, and T. Walker. Optical forces on particles of arbitrary shape and size. J. Opt. A: Pure Appl. Opt., 9(8):S228, 2007.

[93] P. C. Chaumet and C. Billaudeau. Coupled dipole method to compute optical torque: Application to a micropropeller. J. Appl. Phys., 101(2):023106, 2007.

[94] S. H. Simpson and S. Hanna. Holographic optical trapping of microrods and nanowires. J. Opt. Soc. Am. A, 27(6):1255–1264, 2010.

[95] S. H. Simpson and S. Hanna. Optical trapping of microrods: variation with size and refractive index. J. Opt. Soc. Am. A, 28(5):850–858, 2011.

[96] S. H. Simpson and S. Hanna. Application of the discrete dipole approximation to optical trapping calculations of inhomogeneous and anisotropic particles. Opt. Express, 19(17):16526–16541, 2011.

[97] W. L. Collett, C. A. Ventrice, and S. M. Mahajan. Electromagnetic wave technique to determine radiation torque on micromachines driven by light. Appl. Phys. Lett., 82(16):2730–2732, 2003.

[98] D. W. Zhang, X. Yuan, S. Tjin, and S. Krishnan. Rigorous time domain simulation of momentum transfer between light and microscopic particles in optical trapping. Opt. Express, 12(10):2220–2230, 2004.

[99] M. Mansuripur A. Zakharian and J. Moloney. Radiation pressure on a dielectric wedge. Opt. Express, 13(6):2064–2074, 2005.

[100] R. C. Gauthier. Computation of the optical trapping force using an FDTD based technique. Opt. Express, 13(10):3707–3718, 2005.

[101] Z. H. Liu, C. K. Guo, J. Yang, and L. B. Yuan. Tapered fiber optical tweezers for microscopic particle trapping: fabrication and application. Opt. Express, 14(25):12510–12516, 2006.

[102] D. A. White. Numerical modeling of optical gradient traps using the vector finite element method. J. Comput. Phys., 159(1):13–37, 2000.

[103] A. A. R. Neves, A. Camposeo, S. Pagliara, R. Saija, F. Borghese, P. Denti, M. A. Iat, R. Cingolani, O. M. Marag, and D. Pisignano. Rotational dynamics of optically trapped nanofibers. Opt. Express, 18(2):822–830, 2010.

[104] A. van der Horst, An. I. Campbell, L. K. van Vugt, D. A. Vanmaekelbergh, M. Dogterom, and A. van Blaaderen. Manipulating metal-oxide nanowires using counter-propagating optical line tweezers. Opt. Express, 15(18):11629–11639, 2007.

[105] J. N. Wilking and T. G. Mason. Multiple trapped states and angular kramers hopping of complex dielectric shapes in a simple optical trap. Europhys. Lett., 81(5):58005, 2008.

[106] Z. D. Cheng, T. G. Mason, and P. M. Chaikin. Periodic oscillation of a colloidal disk near a wall in an optical trap. Phys. Rev. E, 68(5):051404, 2003.

[107] E. A. Hovenac and J. A. Lock. Assessing the contributions of surface waves and complex rays to far-field Mie scattering by use of the Debye series. J. Opt. Soc. Am. A, 9(5):781–795, 1992.

[108] X. Han, K. F. Ren, L. Mees, G. Gouesbet, and G. Gréhan. Surface waves/geometrical rays interferences: numerical and experimental behaviour at rainbow angles. Opt. Commun., 195(1):49–54, 2001.

[109] P. Yang, H. L. Wei, H. L. Huang, B. A. Baum, Y. X. Hu, G. W. Kattawar, M. I. Mishchenko, and Q. Fu. Scattering and absorption property database for nonspherical ice particles in the near-through far-infrared spectral region. Appl. Opt., 44(26):5512–5523, 2005.

[110] F. Onofri, M. Krzysiek, J. Mroczka, K. F. Ren, S. Radev, and J. P. Bonnet. Optical characterization of bubbly flows with a near-critical-angle scattering technique. Experiments in fluids, 47(4-5):721–732, 2009.

[111] L. Bi, P. Yang, G. W. Kattawar, Y. X. Hu, and B. A. Baum. Scattering and absorption of light by ice particles: solution by a new physical-geometric optics hybrid method. J. Quant. Spectrosc. Radiat. Transf., 112(9):1492–1508, 2011.

[112] F. Xu, K. F. Ren, and X. S. Cai. Extension of geometrical-optics approximation to on-axis Gaussian beam scattering. I. By a spherical particle. Appl. Opt., 45(20):4990–4999, 2006.

[113] F. Xu. Shaped beam scattering by a spheroid and online wet steam measurement by using spectral light extinction method. PhD thesis, PhD thesis. Rouen: University of Rouen, 2007.

[114] J. A. Lock. Ray scattering by an arbitrarily oriented spheroid. i. diffraction and specular reflection. Appl. Opt., 35(3):500–514, 1996.

[115] J. A. Lock. Ray scattering by an arbitrarily oriented spheroid. ii. transmission and cross-polarization effects. Appl. Opt., 35(3):515–531, 1996.

[116] Y. J. Yuan. Diffusion de la lumière par un objet irrégulier pour lapplication à limagerie des sprays. PhD thesis, PhD thesis of Rouen University, France, 29 March2012, 2012.

[117] K. F. Ren, C. Rozé, and T. Girasole. Scattering and transversal divergence of an ellipsoidal particle by using vectorial complex raymodel. J. Quant. Spectrosc. Radiat. Transfer, 113:2419–2423, 2012.

[118] K. L. Jiang, X. Han, and K. F. Ren. Scattering of a Gaussian beam by an elliptical cylinder using the vectorial complex ray model. J. Opt. Soc. Am. A, 30(8):1548–1556, 2013.

[119] K. F. Ren, X. Han, and K. Jiang. Scattering of an arbitrary shaped object by using vectorial complex ray model. In 2012 10th International Symposium on Antennas. Propagation & EM Theory (ISAPE), 2012.

[120] J. R. Mautz and R. F. Harrington. Electromagnetic scattering from a homogeneous material body of revolution. Arch. Elektr. Uebertrag., 33:71–80, 1979.

[121] Ö. Ergül and L. Gürel. Comparison of integral-equation formulations for the fast and accurate solution of scattering problems involving dielectric objects with the multilevel fast multipole algorithm. IEEE Trans. Antennas Propagat., 57(1):176–187, 2009.

[122] H. Gan and W. C. Chew. A discrete BCG-FFT algorithm for solving 3-D inhomogeneous scatterer problems. J. Electromagn. Waves Applicat., 9(10):1339–1357, 1995.

[123] R. Coifman, V. Rokhlin, and S. Wandzura. The fast multipole method for the wave equation: A pedestrian prescription. IEEE Antennas Propagat. Mag., 35(3):7–12, 1993.

[124] T. Malas and L. Gürel. Schur complement preconditioners for surface integral-equation formulations of dielectric problems solved with the multilevel fast multipole algorithm. SIAM J. Sci. Comput., 33(5):2440–2467, 2011.

[125] J. Fostier and F. Olyslager. An asynchronous parallel MLFMA for scattering at multiple dielectric objects. IEEE Trans. Antennas Propagat., 56(8):2346–2355, 2008.

[126] Ö. Ergül. Parallel implementation of mlfma for homogeneous objects with various material properties. Prog. Electromagn. Res., 121:505–520, 2011.

[127] M. A. Yurkin and A. G. Hoekstra. The discrete-dipole-approximation code adda: capabilities and known limitations. J. Quant. Spectrosc. Radiat. Transf., 112:2234–2247, 2011.

[128] K. L. Jiang, X. Han, and K. F. Ren. Scattering from an elliptical cylinder by using the vectorial complex ray model. Appl. Opt., 51(34):8159–8168, 2012.

[129] J. W. Hovenier M. I. Mishchenko and L. D. Travis. Light Scattering by Nonspherical Particles: Theory, Measurements, and Applications. Academic Press, 2000.

[130] H. R. Pruppacher and R. L. Pitter. A semi-empirical determination of the shape of cloud and rain drops. J. Atmos. Sci., 28(1):86–94, 1971.

[131] A. Ashkin and J. M. Dziedzic. Optical trapping and manipulation of viruses and bacteria. Science, 235(4795):1517–1520, 1987.

[132] M. E. J. Friese, T. A. Nieminen, N. R. Heckenberg, and H. Rubinsztein-Dunlop. Optical alignment and spinning of laser-trapped microscopic particles. Natrue, 394(6691):348–350, 1998.

[133] K. Svoboda and S. M. Block. Biological applications of optical forces. Annu. Rev. Bioph. Biom., 23(1):247–285, 1994.

[134] N. K. Metzger, M. Mazilu, L. Kelemen, P. Ormos, and K. Dholakia. Observation and simulation of an optically driven micromotor. J. Opt., 13(4):044018, 2011.

[135] R. M. P. Doornbos, M. Schaeffer, A. G. Hoekstra, P. M. A. Sloot, B. G. de Grooth, and J. Greve. Elastic light-scattering measurements of single biological cells in an optical trap. Appl. Opt., 35(4):729–734, 1996.

[136] Y. Harada and T. Asakura. Radiation forces on a dielectric sphere in the Rayleigh scattering regime. Opt. Commun., 124(5-6):529–541, 1996.

[137] B. Mihiretie, J. C. Loudet, and B. Pouligny. Optical levitation and long-working-distance trapping: From spherical up to high aspect ratio ellipsoidal particles. J. Quant. Spectrosc. Radiat. Transf., 126:61–68, 2013.

[138] J. P. Barton, D. R. Alexander, and S. A. Schaub. Theoretical determination of net radiation force and torque for a spherical particle illuminated by a focused laser beam. J. Appl. Phys., 66(10):4594–4602, 1989.

[139] S. Chang and S. S. Lee. Radiation force and torque excerted on a stratified sphere in the circularly polarized Tem01-mode beam. J. Opt. Soc. Am. B, 5(1):61–66, 1988.

[140] M. I. Mishchenko. Radiation force caused by scattering, absorption, and emission of light by nonspherical particles. J. Quant. Spectrosc. Radiat. Transf., 70(4-6):811–816, 2001.

[141] L. W. Davis. Theory of electromagnetic beams. Phys. Rev. A, 19(3):1177, 1979.

[142] J. P. Barton and D.R. Alexander. Fifth-order corrected electromagnetic field components for fundamental Gaussian beam. J. Appl. Phys., 66(7):2800–2802, 1989.

[143] A. R. Edmonds. Angular Momentum in Quantum Mechanics. Princeton University Press, 1957.

[144] G. Gouesbet, J. J. Wang, and Y. P. Han. Transformations of spherical beam shape coefficients in generalized Lorenz-Mie theories through rotations of coordinate systemsIII. special Euler angles. Opt. Commun., 283(17):3235–3243, 2010.

[145] J. Q. Lu, P. Yang, and X. H. Hu. Simulations of light scattering from a biconcave red blood cell using the finite-difference time-domain method. J. Biomed. Opt., 10(2):024022–02402210, 2005.

[146] J. C. Crocker, J. A. Matteo, A. D. Dinsmore, and A. G. Yodh. Entropic attraction and repulsion in binary colloids probed with a line optical tweezer. Phys. Rev. Lett., 82(21):4352, 1999.

[147] F. M. Kahnert. Numerical methods in electromagnetic scattering theory. J. Quant. Spectrosc. Radiat. Transf., 79:775–824, 2003.

[148] G. Gouesbet. T-matrix formulation and generalized Lorenz-Mie theories in spherical coordinates. Opt. Commun., 283(4):517–521, 2010.

[149] S. H. Simpson and S. Hanna. Computational study of the optical trapping of ellipsoidal particles. Phys. Rev. A, 84(5):053808, 2011.

[150] A. E. Ekpenyong, C. L. Posey, J. L. Chaput, A. K. Burkart, M. M. Marquardt, T. J. Smith, and Michael G. Nichols. Determination of cell elasticity through hybrid ray optics and continuum mechanics modeling of cell deformation in the optical stretcher. Appl. Opt., 48(32):6344–6354, 2009.

[151] R. G. Sebastien, M. T. Wei, J. J. Bai, A. Chiou, P. P. Bareil, P. L. Duval, and Y. L. Sheng. Dynamic deformation of red blood cell in Dual-trap Optical Tweezers. Opt. Express, 18(10):10462–10472, 2010.

[152] F. Xu, J. A. Lock, G. Gouesbet, and C. Tropea. Optical stress on the surface of a particle: homogeneous sphere. Phys. Rev. A, 79(5):053808, 2009.

[153] L. Boyde, A. Ekpenyong, G. Whyte, and J. Guck. Comparison of stresses on homogeneous spheroids in the optical stretcher computed with geometrical optics and generalized Lorenz-Mie theory. Appl. Opt., 51(33):7934–7944, 2012.

[154] J. T. Yu, J. Y. Chen, Z. F. Lin, L. Xu, P. N. Wang, and M. Gu. Surface stress on the erythrocyte under laser irradiation with finite-difference time-domain calculation. J. Biomedical Opt., 10(6):064013–064013, 2005.

[155] M. L. Yang, K. F. Ren, Y. Q. Wu, and X. Q. Sheng. Computation of stress on the surface of a soft homogeneous arbitrarily shaped particle. Phys. Rev. E, 89(4):043310, 2014.

[156] M. L. Yang, K. F. Ren, M. J. Gou, and X. Q. Sheng. Computation of radiation pressure force on arbitrary shaped homogenous particles by multilevel fast multipole algorithm. Opt. Lett., 38(11):1784–1786, 2013.

[157] M. L. Yang, H. W. Gao, and X. Q. Sheng. Parallel domain-decomposition-based algorithm of hybrid fe-bi-mlfma method for 3-d scattering by large inhomogeneous objects. IEEE Trans. Antennas Propagat., 61(9):4675–4684, 2013.

Résumé

Cette thèse est dédiée à la validation du modèle de Tracé de Rayons Vectoriels Complexes (VCRM - Vectorial Complex Ray Model en anglais) par la comparaison des diagrammes de diffusion avec les résultats de SIE- MLFMA (Surface Integral Equation with Multilevel Fast Multipole Algorithm en anglais) et les applications de MLFMA développé à la prédiction de la force de pression de radiation, le couple et la tension exercés sur des grosses particules non-sphériques par un faisceau laser.

En introduisant la courbure du front d'onde comme une nouvelle propriété des rayons lumineux, VCRM apporte une amélioration considérable sur la précision et l'applicabilité du modèle de rayons pour la diffusion de la lumière par les particules non-sphériques. Cependant ses résultats pour les particules non-sphériques restent à valider. Alors, MLFMA est une méthode numérique très efficace pour traiter l'interaction de la lumière avec des particules de forme quelconque. Afin d'étendre sa capacité pour les grosses particules, dans cette thèse, MLFMA est améliorée et parallélisée. Le code mis au point permet d'obtenir des résultats exacts pour les particules de paramètre de taille supérieur à 600. Le bon accord entre les diagrammes de diffusion des grosses particules ellipsoïdales calculés par MLFMA et VCRM illustre la grande capacité de ces deux méthodes.

Ensuite, le code MLFMA développé est appliqué au calcul de la force de pression de radiation (FPR) et le couple sur des particules homogènes de forme quelconque. Pour éviter l'imprécision de la description mathématique en champ lointain de faisceau laser, l'expression analytique de champs électromagnétiques dans la région proche de la particule est utilisée. La FPR et le couple sont donc calculés par le flux du vecteur du tenseur de Maxwell sur une surface sphérique incluant la particule. Cette méthode est très puissante et flexible permettant de prédir la FPR et le couple exercés par un faisceau de forme quelconque sur une grosse particule, comme des particules sphéroïdales, des particules de forme de globule rouge ou moteur.

La FPR et le couple sont des effets mécaniques globaux d'un faisceau de lumière exercés sur une particule. La tension sur la surface d'une particule peut être importante dans l'étude des propriétés élastiques de certaines particules. Le code MLFMA développé est donc étendu au calcul de la tension de surface et VCRM a été appliqué à l'analyse le mécanisme de la tension sur des particules sphéroïdales.

Mots clés: Diffusion de la lumière, particules non-sphériques, Pression de radiation, couple, tension, VCRM, MLFMA

Abstract

This PhD thesis is devoted to the validation of the Vectorial Complex Ray Model (VCRM) by comparison of the scattering diagrams with the results computed by the Surface Integral Equation (SIE) with Multilevel Fast Multipole Algorithm (MLFMA) and the application of the developed MLFMA to the prediction of the scattering matrix, the radiation pressure force, torque and stress exerted on large non-spherical particles by laser beams.

By introducing the wave front curvature as a new property of rays, VCRM improves considerably the precision and the applicability of the ray model for the light scattering by non-spherical particles. But its results for non-spherical particles remain to be validated. On the other hand, MLFMA is an efficient full wave numerical method for computing light scattering by large particles of arbitrary shape. To enhance further its ability for large particles, in this thesis, MLFMA is improved and parallelized with Message Passing Interface (MPI) on a memory distributed computer system. The code developed permits to obtain accurate results for particles of size parameter bigger than 600. The good agreement between the scattering diagrams of large ellipsoidal particles computed by MLFMA and VCRM demonstrates the great capability of both methods.

Then the developed MLFMA code is applied to the computation of the radiation pressure force (RPF), torque on arbitrary shaped homogenous particles. To avoid the imprecision of the mathematical description in far field of shaped beams, the analytical expression of electromagnetic fields in near region is used instead. RPF and torque are therefore computed by the vector flux of the Maxwell's stress tensor over a spherical surface tightly enclosing the particle. This method is very powerful and flexible permitting to deal with the interaction between any shaped beams and large non-spherical particles, such as spheroidal particles, cell like particles and motor shaped particles.

RPF and torque are overall mechanical effect of a light beam on the particles. The stress on the surface of a particle can be important in the study of elastic properties of certain particles (of soft material for example). The developed MLFMA code is hence extended to the computation of the surface stress. At this stage, VCRM has been applied to give a physical analysis on mechanism of optical stress on spheroidal particles. It is found that the maximum of stress on the surface of non-spherical particles may be caused by high order rays.

KeyWord: light scattering, Vectorial Complex Ray Model, Multilevel Fast Multipole Algorithm, non-spherical particle, Radiation pressure force, torque, stress